ABSTRACT

Title of thesis: STRESS CHARACTERIZATION
OF STRETCHABLE CRYSTALLINE
SEMICONDUCTORS

Sabrina M. Curtis, Master of Science, 2018

Thesis directed by: Professor Marina S. Leite
Department of Materials Science

Thesis co-advised by: Dr. Nathan Lazarus and Dr. Randy Tompkins
Special Members of the Graduate Committee

Stretchable crystalline semiconductors are the key to enable wearable high power and energy devices. The work presented in this thesis evaluates the non-uniform surface stress distribution of stretchable Si and GaN serpentine geometries and has yielded the following contributions: (i.) 2D and 3D numerical analyses of the effect of mechanical anisotropy in (100) Si on crystalline stretchable behavior, revealing the <100>direction can be up to 36% more stretchable than the <110>direction, and (0001) GaN has no anisotropic dependence. (ii.) A micro-fabrication procedure which allows for the fabrication and release of stretchable Si into serpentine mechanical test structures which demonstrated an experimental strain-to-rupture of 84%. (iii.) In-situ characterization of the non-uniform surface stress distribution in stretchable Si, while applying external strain, using micro-Raman spectroscopy. (iv.) A micro-scale imaging technique to spatially resolve the local surface stress distribution in stretchable AlGaN/ GaN high electron mobility transistor devices.

STRESS CHARACTERIZATION OF STRETCHABLE CRYSTALLINE SEMICONDUCTORS

by

Sabrina M. Curtis

Thesis submitted to the Faculty of the Graduate School of the
University of Maryland, College Park, in partial fulfillment
of the requirements for the degree of
Master of Science
2018

Advisory Committee:
Professor Marina S. Leite, Chair
Dr. Randy Tompkins, Co-Advisor
Dr. Nathan Lazarus, Co-Advisor
Professor Gary Rubloff, Committee Member

Acknowledgments

I would like to dedicate my Master's thesis to everyone who has supported me along this M.S/B.S journey. To start, I would like express my gratitude for my advisers Dr. Nathan Lazarus and Dr. Randy Tompkins. Their outstanding mentorship has taught me numerous useful research skills and how to truly critically think like a scientist. They gave me the personal freedom and confidence to successfully chase ideas of my own, furthering my love for science. In addition to the guidance I received in the lab, they have both provided me with important life advice. I am a better scientist, writer, critical thinker, researcher, and presenter because of them, and for that I am forever grateful. I'd also like to thank my other committee members Prof. Marina Leite and Prof. Gary Rubloff for always believing in me and motivating me to do better. I owe my decision to obtain a Ph.D. after my masters to the unbelievable support I have received over the years from this committee.

To my Army Research Lab (ARL) members/collaborators/friends: Dr. Barbara Nichols and Dr. Sina Najamaei for their expertise with Raman spectroscopy, and patience with my many questions. Dr. Milena Graziano, Yomery Espinal, and Dr. Manuel Rivas for their positivity, being the best writing buddies, and helping me keep my sanity during the long work nights and weekends. I definitely couldn't have gotten through this without you three. Gabe Smith for his knowledge in mechanics, mentorship during the Collegiate Inventor Competition (FlexSi!), excitement to pursue additional projects with me, and for being an awesome study buddy. Thank you to everyone else at ARL that have helped shaped my project in some shape or form: Dr. Ken Jones, Iain Kierzewski, Cory Knick, Dr. Darin Sharar, Dr. Adam Wilson, Dr. Brendan Hanrahan, Dr. Sarah Bedair, Elad Siman-Tov, Mike Derange, Franklin Nouketcha, Dr. Lauren Boteler, Dr. Aivars Lelis, and Claude Pullen.

Prof. Brajendra Mishra. Thank you to everyone for your patience, guidance, and mentorship over the years. You all have shaped me into the research scientist that I am today, and directly impacted my decision to obtain a Ph.D.

The love, encouragement, and support I have received from my family is truly invaluable. First to James: You have been my rock every step of the way during this master's, and I know I can count on you for absolutely anything. To my siblings: Kaleigh, Chesi, Cade, Marques, Valerie and Jada and cousins: Emily, Maya, Mark, Casey, Janine, Shawn, Dean, Vincent, Kalynn, Zander, Damien, Gavin, and Corrine this thesis is really for all of you. I hope you all chase your dreams, and I know you will all be very successful in life. To Uncle John: thank you for always being a phone call away whenever I needed someone to vent or brag about my accomplishments to! To Aunt Nichole: for being my second mom, 14er buddy, and for your hundreds of edits on my papers/documents over the years. I am a better person and definitely a better writer because of you. To my other parents: Jeff, Tony, and Tiffani, thank you all for stepping up and parenting me in all different ways. I am the responsible, fun, witty, and disciplined person that I am today because of my well-rounded upbringing between my 4 (or 6?) parents. To my Curtis, Bailey, Daigle, Cowen, and Williams grandparents thank you all for always staying interested in my research and pushing me to accomplish my goals. My gratitude also extends to all of my other cousins, aunts, uncles, and step family members that would take two more pages to list!

Finally, to my best friend, the one constant in my life, my mom Jennifer. Thank you for always believing in me even when I didn't. You are the reason I came to Maryland in the first place and you led me to engineering. You have worked so hard and sacrificed so much to give Kaleigh and I everything we wanted and needed. You are truly an inspiration, I love you mama.

Sabrina M. Curtis
April 2018
College Park, MD

List of Figures

ix

Chapter 1: Introduction and Research Objectives

1.1 The Need for Stretchable Crystalline Materials

The motivation for this research lies in the need for stretchable high power and high energy systems that can elastically bend, flex, and stretch by a minimum of 30% strain for integration into the soldiers' uniform or onto their skin. Crystalline semiconductors (such as Si and GaN) are brittle materials used in a number of power and energy applications, and are intrinsically not stretchable or flexible; however they can reach unprecedented end-to-end displacements (10s - 100s % global strain) if patterned into unconventional micro-structured serpentine geometries (1). Our Wide Band Gap Semiconductors research group in the Energy and Power Division at United States Army Research Laboratory (ARL) is pursuing the development of the first stretchable aluminum gallium nitride / gallium nitride high electron mobility transistor (AlGaN/ GaN HEMT) (2; 3) for highly efficient power management (> 100 watts) of wearable systems which could serve in applications such as the DARPA Warrior Web soft exoskeleton (4; 5). The research described in this thesis is a numerical and experimental evaluation of the non-uniform surface stress distribution of crystalline semiconductors (Si and GaN) patterned into stretchable serpentine geometries. Modeling and experimental techniques are presented to examine the influence of stretchable serpentine geometry and crystalline anisotropy on the non-uniform stress distribution under applied external strain.

Si has a low-band gap of 1.12 eV and is used in a variety of low power-output sensor and actuator devices due to its low manufacturing cost, matured fabrication processes, and its abundance which also makes it the most common substrate material for MEMS devices (6). Si is reaching its limits of power density

due to limitations in the material properties such as a low critical electric field and thus a high specific on-resistance, and high rectifying losses (7). Rectifying and resistive losses are one of the largest sources of power loss in wireless power systems and result in the generation and dissipation of heat which could cause discomfort to a user if integrated onto human skin (8) or a soft substrate that could be worn. As an alternative to Si devices, wide band gap materials such as 6H-SiC (2.86 eV), GaN (3.4 eV), and C (diamond) (5.6 eV) have high critical electric fields, low specific on resistances, and low resistive losses which can allow for higher power, higher frequency, faster-switching, and overall more efficient wearable device technologies (7; 9). High electron mobility transistor (HEMTs) are a type of field effect transistor used to provide high power at microwave frequencies in applications such as low noise small signal amplifiers, power amplifiers, and oscillators (9; 10). An AlGaN/ GaN heterostructure is an ideal candidate for HEMT devices since the band gap is 3x higher than Si it can achieve higher voltages, electron mobility, break down fields and power efficiencies, while maintaining lower rectifying losses (7). In addition the specific on-resistance of GaN is 1000X lower than Si, meaning it can mitigate the heat loss significantly better, which is desired for wearable systems (2). These advantages are the reasons why our research group is exploring stretchable crystalline materials to fabricate the first stretchable AlGaN/ GaN HEMT device, for stretchable wireless high power management.

When designing devices intended for wearable applications, it is important to understand and predict the failure strain value and stress concentration locations of the device. This work proposes a simple theoretical and in-situ experimental stress mapping and monitoring technique of Si and GaN serpentines under applied strain. 2D and 3D finite element analysis (FEA) numerical simulations are used to model the non-uniform local stress distribution of multiple stretchable serpentine structures under applied external strain. This allows for the prediction of the maximum surface stress on the structure and its likely failure location. The model also provides insight for promising stretchable geometries, which are then fabricated from Si and GaN. The modeled local stress distribution along the serpentine geometry after

an applied external strain is then experimentally verified using the non-destructive characterization technique micro-Raman spectroscopy. Finally, further experimental verification is presented through low-cycle stress monitoring experiments and optical imaging. Adapting widely used theoretical modeling and experimental techniques of localized stress concentrations within crystalline semiconductors can provide insight into predictive failure analysis of stretchable crystalline integrated circuits.

1.2   Master's Thesis Research Contributions

I accomplish the following research objectives by modeling, fabricating and experimentally characterizing the non-uniform stress distribution of stretchable crystalline materials. From these contributions, I foresee the methods developed in this thesis to be widely implemented during future stretchable crystalline device design, fabrication process monitoring, and performance testing.

(i.) Stretchable anisotropic modeling of crystalline semiconductors. Using COMSOL Multiphysics 5.2, I perform a refined 2D model and the first 3D finite element model (FEM) investigating the influence of serpentine geometry and mechanical anisotropy on the stress/ strain behavior of (100) Si and (0001) GaN. To our knowledge, this is the first 3D anisotropic FEM model of any stretchable crystalline semiconductor. In agreement with prior results (2), our results show serpentine geometries can reduce peak stress by 20-98%, and geometries with curved edges (Curved Corner and Horseshoe) mitigate stress under strain better than those with sharp corners. Upon performing in-plane rotations to study crystalline anisotropic stretchable dependence it was demonstrated (0001) GaN behaves isotropically within the c-plane used for GaN power device fabrication which is ideal for stretchable electronics. (100) Si behaves anisotropically, revealing the <100> direction can be up to 12-30% more stretchable than the <110> direction.

(ii.) Stretchable fabrication and release process of crystalline materials. I develop and optimize a reliable micro-fabrication process which allows for the fabrication and release of free standing stretchable crystalline Si serpentine

mechanical testing structures. This procedure uses standard micro-machining and photolithography techniques, that can easily be repeated in a standard clean room, allowing fabrication of serpentines with varying thicknesses, widths, and amplitudes ranging from a few nanometers to hundreds of microns. This process could be adapted to allow for the release of other stretchable thin-film crystalline materials epitaxially grown onto a silicon substrate, such as III-V materials (GaN, AlGaN, InGaN). Furthermore, this fabrication and release process is compatible with dielectric and metal deposition processes which are crucial steps during stretchable device fabrication.

(iii.) **In-situ stress characterization and fatigue evaluation of stretchable Si with micro-Raman Spectroscopy.** For the first time, I experiemntally characterize the non-uniform local surface stress distribution on a stretchable <100> Curved Corner Si serpentine while applying global external strains of 0 - 72%. To achieve this, I custom-built a 3D printed sample holder that allows for static micro-Raman stress measurements to within 50 MPa, while applying external strain on the serpentine structure. Due to a small width-to-radius ratio (w/r = 0.2), the tested <100> Curved Corner serpentine buckles out of plane to relieve stress under applied external strain, non-uniformly concentrating the maximum stress in the buckled regions called the Bend. This is the location of fracture predicted by the 3D anisotropic model. Additionally, tensile testing on the <110> Curved Corner Si serpentine revealed a global strain-to-rupture of 84%, which is in excellent agreement with the 2D model. However, the local strain within the individual period could displace by larger amounts than the global strains, which was predicted in the 3D model. I also show micro-Raman spectroscopy can be used to study the reversible elastic behavior of stretchable crystalline serpentines by performing low-number cycle fatigue characterization for 15 cycles from 0 - 40% strain, showing no appreciable change in the stress.

(iv.) **Stress monitoring of stretchable AlGaN / GaN HEMT device fabrication using micro-Raman spectroscopy.** A variant of micro-Raman spectroscopy is used to spectrally and spatially resolve the local surface stress distribu-

tion within GaN devices, into 2D stress maps. With my collaborators at ARL and the College of Nanoscale Science at SUNY Polytechnic Institute, I study the stress changes induced in stretchable AlGaN/ GaN HEMT devices, fabricated through two different approaches (bottom-up vs top-down). I show that selective area growth (bottom-up approach) of AlGaN/ GaN HEMT devices onto a sapphire substrate induces a strong compressive stress (-1.7 GPa). I also show that etching AlGaN/ GaN into a stretchable HEMT device on a silicon substrate through the top-down approach induces tensile stress (+0.5 GPa). Finally, I demonstrate removing the Si substrate and encapsulating the stretchable device within a soft silicone elastomer induces additional tensile stress (+0.8 GPa).

1.3   Thesis Organization

This thesis is organized into seven main chapters. Chapter 1 stated the research problem and the contributions of the thesis. Chapter 2 sets the motivation to use Si and GaN in stretchable electronic applications, covers necessary background information of materials and reviews the mechanical concepts that enable traditionally brittle and rigid materials to stretch. Additionally, the influence of crystalline anisotropy in Si and GaN is reviewed. Chapter 3 discusses the 2D and 3D finite element models developed to evaluate the mechanical behavior of Si and GaN stretchable structures under applied strain. This includes evaluation of the anisotropic behavior of (100) Si in serpentine structures, prediction of failure location, and determination of the maximum tensile strain on two serpentine geometries, as a function of the width-to-radius ratio. Chapter 4 describes the details of the novel micro-fabrication and release process developed that allowed for the development of single crystal Si and GaN into stretchable mechanical test structures. Chapter 5 presents the experimental procedure, results, and analysis of micro-Raman spectroscopy data for measuring the non-uniform stress distribution of Si mechanical test structures to validate the model. Additionally, I present using using micro-Raman as a low-cycle fatigue characterization technique. Chapter 6 presents methodology

to use micro-Raman spectroscopy as a stress monitoring technique during the fabrication of stretchable AlGaN/ GaN HEMTs. Finally, Chapter 7 provides conclusions, recommendations for future work, and the research contributions of this work to the greater academic community.

Chapter 2:   Silicon and Gallium Nitride for Stretchable Electronics

Stretchable electronics is the integration of highly deformable electrical conducting components onto soft stretchable substrates. Fabrication and transfer processes are well established for stretchable conductor systems that embed metal traces into elastomers for metal interconnection of circuit components, often through a wavy serpentine method (1; 11; 12). However, research on semiconductor stretchable devices is less reported (13; 14; 15). Inorganic materials such as crystalline semiconductors, metals, dielectric oxides and nitrides are required to develop high-performance stretchable circuits for wearable electronic applications (16). To enable a stretchable device, all circuit components must be architecturally reconfigured into compliant geometries, or replaced with intrinsically high strain materials (17). Chapter 2 is intended to review the current status of research efforts toward stretchable materials, components, and devices. This chapter also motivates why the crystalline semiconductors silicon (Si) and gallium nitride (GaN) are particularly interesting materials to study for applications in stretchable power management and future stretchable energy devices. Finally, an overview of the basic materials properties, and the effect of crystalline anisotropy of Si and GaN on their mechanical behavior is presented.

2.1 Stretchable Materials, Methods and Devices

2.1.1 Requirements for Wearable Electronics

Wearable smart electronics are becoming increasingly popular among consumers and military personnel because they offer a more convenient solution to portable electronics. Wearable electronics can be achieved by micro-fabricating and implementing stretchable electrical devices directly onto human skin (18), or a substrate that can be worn (19; 20; 21). Any device intended to be used for wearable applications must elastically survive cycled deformation such as bending, flexing, twisting and stretching by a minimum of 20% strain (16) to 30% strain, to match the elastic performance of human skin (18). Some locations of the body are reported to require even higher strain levels up to a 100%, such as behind the kneecap (8). To meet these demands, high performance wearable electronic systems require all active circuit components to be elastically deformable, and thus stretchable.

Early efforts to build stretchable conducting circuits exploited the use of semiconducting organic materials due to their intrinsic hyperelastic (high strain) mechanical properties (22; 23; 24). Many organic flexible and stretchable devices have been demonstrated included organic stretchable solar cells (25), organic light-emitting diode (OLED) displays (26), flexible artificial electronic skin (27), and organic photodiodes (OPD) for non-invasive medical sensors (28). However, with the growing complexity of wearable technologies requiring high power and high energy output, the low carrier mobilities and resulting low efficiencies of organic materials are not suited for these applications (29). As a result, vast efforts have been made to develop methods and compliant geometries to enable stretchability within inorganic materials, which are traditionally low-strain materials (13; 14; 15; 30).

2.1.2 Stretchable Inorganic Materials, Methods, and Devices

Metal conductors, like most inorganic materials, are intrinsically stiff and unable to stretch significantly ($<< 1\%$); however, they can bend if their cross section

is sufficiently thin (11). One of the first techniques to develop a stretchable circuit system with thin-film metal is referred to as the pre-strained substrate method (31; 32). In this method, a stretchable substrate such as silicone or polyurethane is held under tension, and evaporation or sputtering is used to deposit the metal directly onto the substrate. When the tension is released from the substrate, the system is allowed to relax which buckles the metal forming compliant out-of-plane wavy structures. These highly deformable metallic nanoribbons are heavily used as stretchable inter-connectors, because they can regain mechanical and electrical continuity upon cycling strain (31).

A second method to create stretchable metal uses standard photolithography and micro-machining techniques to pattern materials into 2D structures comprised of kinks and waves, referred to as serpentines. These structures can elastically cycle large end-to-end displacements, reversibly, behaving similar to a spring. The amplitude and wavelength of the wavy serpentine geometry undergo a geometrical reconfiguration to relieve stress in response to the physical deformations (11; 12; 33). For example, Gray et al. explored the buckling mechanics and stretchable behavior of gold (Au) patterned into 2D spring-like serpentine structures. They showed that by reducing the thickness and width of the serpentine traces, the structure becomes mechanically more reconfigurable and could reach higher tensile strains. They demonstrated the gold metal wires could stretch and compressive reversibly by 54% several times, while maintaining stable electrical conductivity (11).

The mechanical performance of the serpentine can be further improved upon by embedding the serpentine components within a soft elastomer support, such as polydimethylsiloxane (PDMS) (34). The soft substrate offers both more deformable regions and mechanical protection, which helps prevent damage to the circuit and can improve device performance, life-time, and fatigue characteristics (35; 36; 37). The effective stiffness, and thus strain-to-rupture of the serpentine/ elastomer system is tunable, dependent on the geometrical parameters: arc length, amplitude, height, width and Youngs modulus of the materials. Using an elastomer as the stretchable substrate is advantageous because the modulus of elasticity is at least

three orders of magnitude lower than the wavy material conductive material embed within. This means when the material is stress/strained, the majority of the peak stresses are concentrated in the elastomer rather the conductor components, (11; 38; 39). Thin copper wires were demonstrated to reach strains beyond $< 50\%$, when well-bonded to an elastomeric substrate, however, it was reported that metals undergo irreversible plastic deformation, which would cause a degradation in the mechanical and electrical performance of the stretchable device (40).

2.2 The Need for Stretchable Crystalline Materials for Power and Energy Devices

Currently, the most efficient power and energy devices utilize crystalline inorganic semiconductor materials, which have a tensile strain of $< 1\%$, far below the 30% tensile strain requirement for wearable systems. While there are significant research advances in the development of flexible high power and high energy devices from inorganic materials (41), these technologies are insufficient for stretchable electronic applications, due to structural limitations. As a result, great efforts have been made to enable stretchable lithium ion batteries (42), stretchable super capacitors (43; 44), stretchable crystalline solar cells (30; 45), stretchable inductors (46; 47) and other stretchable wireless power transfer technologies (48; 49). Development of stretchable single crystalline semiconductor devices made of silicon (Si) and gallium nitride (GaN) are of particular interest because they could be the solution to high power energy generation and energy storage wearable devices.

One of the first techniques used to enable stretchable systems which contain rigid or brittle circuit components is referred to as an "island plus bridge" layout, where the functional inorganic material is a rigid micro-scale "island" connected by stretchable metal interconnect "bridges" (50). The bridges must have a low effective stiffness to tolerate large deformations. Through selective gas and chemical etch processes, these island structures can be released (de-bonded) from their traditional rigid substrate, and transferred to a stretchable substrate, (42; 45). Under

10

deformation, if the peak stresses present in the island are smaller than yield stress (7 GPa for silicon) of the material, the system can survive cycling tension and compression, and is considered to be a highly elastic reversible system. The serpentine geometries are suitable to serve as the structure for both the device "island", and the stretchable metal interconnect "bridge" (18).

Single crystal silicon is a narrow band gap material (1.1 eV), widely used as various components in various microelectromechanical systems (MEMS), due to well-studied materials properties, and matured fabrication procedures which leads to low manufacture cost. Well known deposition, etching, and photolithography techniques have led to highly efficient flexible Si solar cell devices, super junction MOSFETs, and other high performance integrated silicon circuits. While Si is a an excellent semiconductor material, Si-based transistor devices are reaching their limits of power density, breakdown voltage, operation frequency, and temperature (7). In search of devices with higher power and energy densities, wide-band gap (WGB) semiconductors (< 2 eV) may be able to overcome these challenges demonstrating power electronic devices that are faster, more efficient, and can withstand higher voltages and higher temperatures than Si. As a result, Si has transitioned into serving as a cost-effective substrate to support epitaxial growth of high performing wide band gap materials.

Gallium Nitride (GaN) is a an ideal candidate for highly efficient power conversion electronics due to its wide direct electronic band gap (3.4 eV at room temperature), which results in a high electronic breakdown field, large electron saturation field, and unusually large electron mobility, allowing it to be used in high temperature, high voltage, and high frequency applications (51). One of the advantages of using GaN for power electronics is the magnitude of the band gap can be altered, ranging as high as AlN (6.2 eV) and as low as InN (0.64 eV), because GaN forms solid solutions (AlGaN, InGaN, AlInGaN) with its III-Nitride counterparts. The advantage of these properties for high electron mobility transistor devices will be further discussed in Section 6.1.

2.3 Anisotropic Effects of Silicon and Gallium Nitride

Single crystal (or monocrystalline) materials, are composed of repeating periodically arrayed atoms that form crystal lattices. Simple cubic materials behave isotropically, meaning their mechanical, optical, and electronic properties have no directional dependence due to rotational symmetry. Silicon and gallium nitride have anisotropic crystal structures which means their properties are dependent on crystallographic orientation. The concept of mechanical anisotropy in Si and GaN are reviewed below.

2.3.1 Mechanics of (100) and (111) Silicon

The crystal structure of single crystal Si is a face-centered-diamond cubic, which consist of two interpenetrating face centered cubic (FCC) crystal structures, offset by an amount of x = y = z = $\frac{a_0}{4}$, where a_0 is the lattice constant of Si. The elastic properties, stiffness and compliance matrix, of silicon can be described using three independent elements due to the cubic symmetry in silicon. Due to mechanical anisotropy, if one were to fabricate identical MEMS devices on the isotropic (111) Si plane and anisotropic (100) Si plane the properties of the device are expected to behave quite differently depending on local atomic arrangement. Here, I evaluate (100) Si since this is the most common plane for MEMS device fabrication. (111) Si is also shown since it's a common substrate for III-V materials, due to the in-plane isotropic properties which promotes lattice matching along the closed packed planes of the basal (0001) plane of the hexagonal wurtzite crystal structure. The crystal structure of Si highlighting the (100) and (111) planes are shown in Figure 2.1.
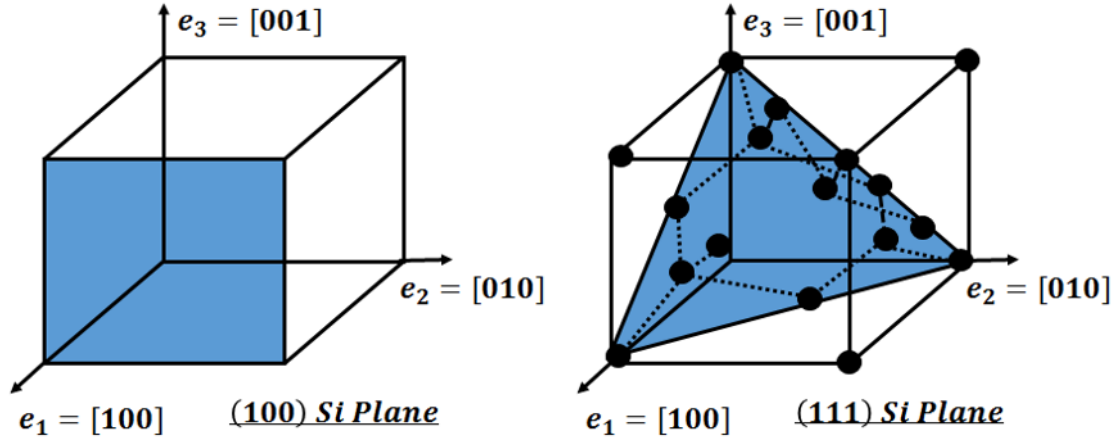
Figure 2.1: **Diamond cubic crystal structure of single crystal silicon.** A.) (100) anisotropic plane and B.) (111) isotropic plane.

2.3.2 (0001) Gallium Nitride

Gallium Nitride is composed of a group III element (Ga), and a group V element (N). It owes its interesting material properties due to the bonding nature of the Ga and N ions. GaN, AlN, and AlGaN all have a wurtzite crystal structure, which is a thermodynamically stable crystal structure composed of two interpenetrating hexagonal closed packed lattices (52). All group III metals bonded to nitrogen experience a large difference in electronegativity, creating strong ionic bonds between the molecules. Since ionic bonds are the strongest bonds to break, the energy that it takes to excite an electron from the valence band to the conduction band is extremely large, therefore, the material has a wide band gap. The material properties of GaN enable advanced performance of high-electron mobility transistors (HEMT), monolithic microwave integrated circuits (MMICs) for RF applications, solar cells, and light emitting diodes (LEDs). The wurtzite crystal structure of GaN is shown in Figure 2.2.

13
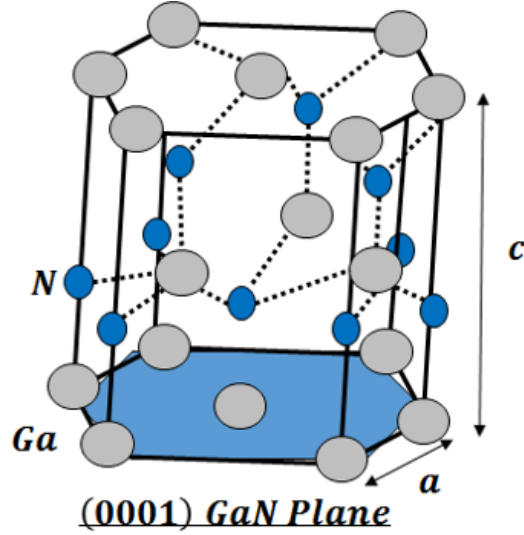
Figure 2.2: **Wurtizite hexagonal closed packed crystal structure of single crystal GaN.**
Herem a is the lattice constant which is interatomic spacing between two Ga ions. The blue
highlighted plane is the (0001) growth plane analyzed in this work.

2.3.3   Effect of Anisotropy on the Stiffness Tensor of Si and GaN

The Young's modulus E is a material property that describes the relationship
between stress and strain for an out-of-plane deflection of a square plate, and is
anisotropically dependent on crystal axis orientation. For Si, the Young's modulus
ranges from 130 - 188 GPa which could present up to a 45% variation in stress
within traditional MEMS devices, or stretchable crystalline serpentines. The effect
of mechanical anisotropy along various crystallographic orientations of a material
is described by the material's elastic coefficients related through the fourth ranked
stiffness and compliance tensors. Due to crystal symmetry, the generalized stiffness
and compliance coefficients can be reduced to a simplified 6 x 6 matrix, as shown
in Equation 2.1.

$$C_{ijkl} = \begin{bmatrix} C_{11} & C_{12} & C_{13} \\ C_{21} & C_{22} & C_{23} \\ C_{31} & C_{32} & C_{33} \\ & & & C_{44} \\ & & & & C_{55} \\ & & & & & C_{66} \end{bmatrix} \quad S_{ijkl} = \begin{bmatrix} S_{11} & S_{12} & S_{13} \\ S_{21} & S_{22} & S_{23} \\ S_{31} & S_{32} & S_{33} \\ & & & S_{44} \\ & & & & S_{55} \\ & & & & & S_{66} \end{bmatrix}$$

$$(2.1)$$

where $C_{11} = C_{iiii}$, $C_{12} = C_{iiji}$, $C_{44} = C_{ijij}$, $S_{11} = C_{iiii}$, $S_{12} = S_{iiji}$, $S_{44} = 4S_{ijij}$

The stiffness coefficients can then be used to calculate the compliance coefficients, at a particular orientation using Equation 2.2. For isotropic materials the stiffness tensor C_{ijkl} is simply expressed as the single coefficient E of the Young's modulus (53).

$$S_{11} = \frac{C_{11} + C_{12}}{(C_{11} - C_{12})(C_{11} + 2C_{12})}, S_{12} = \frac{-C_{12}}{(C_{11} - C_{12})(C_{11} + 2C_{12})}, S_{44} = \frac{1}{C_{44}} \quad (2.2)$$

The stiffness and compliance tensors are also related to stress and strain in a crystal through Equation 2.3.

$$\textbf{Hooke's Laws: } \sigma_{ij} = C_{ijkl}\epsilon_{kl}, \epsilon_{ij} = S_{ijkl}\sigma_{kl} \quad (2.3)$$

where σ_{ijkl} and ϵ_{ijkl} are the stress and strain components respectively.

Through well-established calculations, the generalized Hookes Law can be used to resolve the stress components along a crystal axis Equation 2.3. Through multiplication of the direction cosine matrix by a known tensor reference frame, one can perform a tensor transformation to determine the elastic coefficients for any crystallographic orientation. These calculations are well established and are reported in detail elsewhere for Si (53; 54; 55) and for GaN (56; 57). After performing these rotations, the Youngs Modulus can then be calculated for the [100], [110], and [111] crystallographic directions of Si as shown in Equation 2.4 and are found to be E_{110} = 169 GPa, E_{100} = 130 GPa, E_{111} = 188 GPa.

$$\frac{1}{E_{100}} = S_{11} = \frac{1}{130}GPa^{-1}$$

$$\frac{1}{E_{110}} = S_{11} - \frac{1}{2}[(S_{11} - S_{12}) - \frac{1}{2}S_{44}] = \frac{1}{169}GPa^{-1}$$ (2.4)

$$\frac{1}{E_{111}} = S_{11} - \frac{2}{3}[(S_{11} - S_{12}) - \frac{1}{2}S_{44}] = \frac{1}{188}GPa^{-1}$$

In the case of a (100) Si plane, the wafer flat is aligned in the [110] direction, and has a Young's modulus of $E_{110} = 169$ GPa. The bracket notation of [110] indicates this direction is a member of the <110> family of directions which lie parallel or perpendicular ("X" or "Y" axis) to the wafer flat. The lowest Young's modulus ($E_{100} = 130$ GPa) occurs along the [100] direction, in the <100> family occurs at a 45° rotation from the "X" or "Y" axis. The highest Young's modulus ($E_{111} = 188$ GPa) is along the <111>family of directions on the (111) Si plane (53).

The studies performed in this thesis investigate the effect of mechanical anisotropy on the stretchable behavior of crystalline serpentines on (100) Si and (0001) GaN. To do this, we performed in-plane rotations in 10° increments on (100) Si from the [100] direction, and 10° increments on the (0001) GaN from the [0001] direction, and then evaluated the stress behavior of identical serpentine geometries. The elastic stiffness tensors [100] Si, [110] Si, and [0001] GaN used in this thesis are shown in Equation 2.5, 2.6, and 2.7.

$$C_{[100]Si} = \begin{bmatrix} 165.7 & 63.9 & 63.9 & & & \\ 63.9 & 165.7 & 63.9 & & & \\ 63.9 & 63.9 & 165.7 & & & \\ & & & 79.6 & & \\ & & & & 79.6 & \\ & & & & & 79.6 \end{bmatrix} x10^9 Pa, \quad (2.5)$$

$$C_{[110]Si} = \begin{bmatrix} 165.7 & 63.9 & 63.9 & & & \\ 63.9 & 165.7 & 63.9 & & & \\ 63.9 & 63.9 & 165.7 & & & \\ & & & 79.6 & & \\ & & & & 79.6 & \\ & & & & & 79.6 \end{bmatrix} x10^9 Pa \qquad (2.6)$$

$$C_{[0001]GaN} = \begin{bmatrix} 390 & 145 & 106 & & & \\ 145 & 390 & 106 & & & \\ 106 & 106 & 398 & & & \\ & & & 105 & & \\ & & & & 105 & \\ & & & & & 122.5 \end{bmatrix} x10^9 Pa \qquad (2.7)$$

The stiffness tensor for 0° - 90° in-plane rotations on (100) Si and (0001) GaN was calculated to be used in future modeling steps. The first elastic coefficient (C_{11}) is representative of the anisotropic behavior of the material as a function of crystal rotation along the xyz axes, and is shown for both Si and GaN in Figure 2.3.
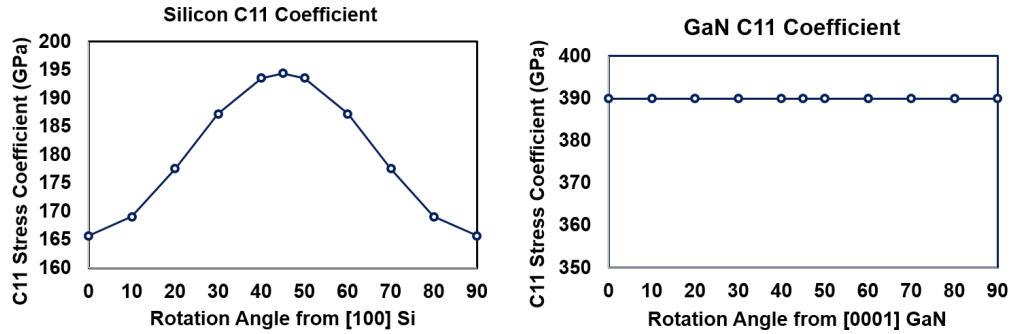
Figure 2.3: C_{11} **stiffness coefficient of in-plane rotations on (100) Si and (0001) GaN** Variations in the C_{11} coefficient in Si indicate strong anisotropic behavior in the (100) plane. The lack of variations in the C_{11} coefficient indicates isotropic behavior

Silicon is shown to have the highest C_{11} value along the <110> direction while

the lowest C_{11} value occurs at the 45° rotation along the <100> direction. This leads me to hypothesize that the <100> direction in Si would have improved stretchable behavior over the <110>. Additionally there is no variation in the C_{11} value on the (0001) GaN plane, as a function of rotation angle which indicates this plane of GaN would display isotropic stretchable behavior along all crystallographic directions.

Mechanical anisotropy plays a significant role in predicting the failure of crystalline devices. To the best of our knowledge, this issue has not been addressed in stretchable crystalline devices. Generally the anisotropic mechanical dependence in devices with rectangular shapes is shown to be small, however, it is expected that this dependence will become significant when we evaluate serpentine geometries with curved edges and angled members (53). This influence will be investigated using finite element modeling methods and by experimentally fabricating and characterizing crystalline serpentine devices.

Chapter 3:   Numerical Modeling of Stress and Strain in Stretchable Crystalline Materials

Finite element analysis is used in Chapter 3 to examine the mechanical behavior of stretchable single crystal semiconductors. 2D and 3D models are performed using the comprehensive numerical solver COMSOL Multiphysics 5.2 to evaluate the effect of serpentine geometry and mechanical anisotropy on crystalline stretchable behavior of (100) Si and (0001) GaN. To do this I first refine a 2D model to evaluate the non-uniform von Mises peak stress distribution after applying a 30% strain parallel to the trace on a number of common serpentine geometries (curved corner rectangle, rectangle, horseshoe, triangle, and trapezoid) (2; 47). It was found that serpentine geometries with a more gradual change in direction (i.e Curved Corner and Horseshoe) distribute the local strain fields over the trace more uniformly, and are ideal candidates for stretchable geometries of crystalline devices. Next, in-plane rotations are applied on (100) Si and (0001) GaN to investigate the influence of crystallographic orientation on the von Mises peak stress distribution showing (0001) GaN behaves isotropically, displaying 6-fold rotation symmetry, while (100) Si has a strong anisotropic dependence due to 4-fold rotation symmetry. To further study the anisotropic dependence in Si, I then determine the maximum global tensile strain of the Curved Corner and Rectangular geometries as a function of the width-to-radius (w/r) ratio. Si serpentines with a low w/r ratio (< 0.1) were demonstrated to reach end-to-end displacements as high as 276% (2.76X its original length), while w/r ratios of up to 0.6 could reach global end-to-end displacements of $> 20\%$. Additionally, serpentines patterned in the <100> direction on the (100) Si plane were found to be up to 17 - 32% more stretchable than those patterned

19

in the <110> direction. Finally, a 3D FEA moel is used to further investigate the effect of mechanical anisotropy in the Si Curved Corner structure with w/r = 0.2, predicting a maximum global tensile strain of 84% in the <100> direction and 76% in the <110> direction. Stress measurements using micro-Raman spectroscopy with be used to experimental verify these results in Chapter 5.

3.1 Numerical Evaluations of Stretchable Systems

Finite Element Analysis (FEA) is a popular tool researchers use to analyze material mechanical behavior and extract important parameters such as the von Mises peak stress distribution, tensile strain, principal stress/ strain coefficients, and device failure location in many microelectromechanical systems (MEMS). FEA has played a pivotal role in the rapid expansion of the stretchable electronics field, by providing great insight on the ideal architectures for stretchable device fabrication and evaluation of the mechanical and electrical performance under strain. Early efforts used FEA techniques to examine the mechanical behavior of free standing serpentine metallic traces (Au, Cu, Pt), and metalic traces bonded to elastomer supports for use as stretchable interconnects in "island-bridge" device layouts. These studies show that serpentine structures can strongly relieve stress under strain, increasing intrinsic metallic strain-to-rupture from (< 5%) to 25 - 1600%, depending on geometrical parameters such as the ratio between the trace width (w) and arc radius (r), and the serpentines length (l) (11; 33; 37; 38; 39; 58; 59). These studies demonstrated curved structures experience smaller stress concentrations than structures with sharp corners (58). (11; 33; 37; 38; 39; 59)

Often times fabricated stretchable devices are encapsulated within an elastomeric substrate to provide protection and additional stretchable support. FEA has previously been used to examine the effect of film thickness and grain size on the mechanical performance of metallic 2D serpentines supported by polymer substrates. Through simulation and optical imaging it has been shown that as film thickness decreases, crack density increases which subsequently causes an increase in the yield

strength (and effective stiffness) in the material, due to an increase in grain sizes (37). Another study looked at the influence of serpentine thickness on the elastic stretchability of the serpentine trace, showing thicker films are less stretchable due to a change in the primary deformation mode from buckling to in-plane. Through FEA, fatigue testing, and scanning electron microscopy (SEM) imaging, Kim et. al demonstrated that a serpentines stretchability is directly proportional to substrate thickness, with thinner substrates mechanically behaving the best (21; 38; 39).

Additionally, FEA has been used to investigate the electrical performance of serpentine metallic traces for stretchable interconnects, and stretchable devices. For example, Lazarus et al. investigated the influence of wavelength and amplitude of periodic geometries on the electrical performance of serpentine structures for use in stretchable inductor coils (48). Their findings, in agreement with Balakrisnan et al., show that copper metal interconnects without sharp corners (Sine Wave, Horseshoe, and Curved Corner) gave not only the best mechanical performance, but also the best electrical performance; however, curved structures are pointed out to be more difficult to micro-fabricate (58). Curved structures mitigate stress concentrations over a large area and perform the best electrically due to current switching directions more gradually. Overall, these findings support the idea that patterning metal into these periodic stretchable geometries will allow the system to survive significant amounts of strain without electrical or mechanical failure.

With the growing popularity of stretchable crystalline materials, a few research groups have looked at modeling the mechanical properties of semiconductor materials such as Si and GaN (2; 16; 38). Widlund et al. performed a very complete and systematic FEA and experimental study on the stretchable behavior of free standing 2D silicon serpentine ribbons, assumed to be confined to in-plane deformation only. They generated a model which explains serpentine mechanical behavior in terms of dimensionless parameters such as such as *Stretchability* (ε_{app}^{cr}) which is the global critical applied strain before the serpentine ribbon ruptures, given by

$$\varepsilon_{app}^{cr} = \frac{\varepsilon_{cr}}{\frac{\varepsilon_{max}}{\varepsilon_{app}}} \tag{3.1}$$

where ε_{cr} is the intrinsic strain-to-rupture, ε_{max} is the maximum tensile strain of the material, and ε_{app} is the applied strain. $\frac{\varepsilon_{max}}{\varepsilon_{app}}$ is the given as the ratio between maximum strain and the applied strain. The stretchability parameter controls the structure's stiffness which is related to the maximum end-to-end displacement that can be achieved by a free standing serpentine ribbon. Using the isotropic materials properties of silicon (E = 130 GPa, $\nu = 0.27$), they found that Si serpentine ribbons with a small w/r, large length-to radius ratio (l/R), and large arc angle α became compliant and could reach strains several orders of magnitude higher than straight Si wires. There results indicate that even brittle Si with $\varepsilon_{cr} = 1\%$, could reach ε_{app}^{cr} up to 1000% with extremely large l/R ratios (16); however they did not report experimental verification of these results. Additionally, in this model they used the isotropic material properties of Si which does not accurately reflect the mechanics of Si along different crystal axis.

Tompkins et. al. performed the first anisotropic 2D FEA study of single crystal Si and GaN in serpentine geometries as structural candidates for fabrication of the first stretchable high electron mobility transistor devices (HEMTs) (2). With COMSOL Multiphysics 3.3, they performed a linear elastic model to look at the effect of serpentine geometry on the maximum von Mises peak stress of Si and GaN serpentines, after applying a 30% global strain parallel to the trace. They determine that serpentine geometries could offer a 30 - 98% reduction in peak stress for GaN, 28 - 92% reduction for Si, and that the optimal serpentine geometries were ones with a more gradual change in direction (i.e Sinusoid) behaved could displace by larger amounts than geometries with sharp corners (i.e rectangle). They also performed the first anisotropic dependence study on the serpentines mechanical behavior, by applying in-plane rotations about (0001) GaN and (100) Si. They found the GaN behaves isotropically within the (0001) growth plane and (100) Silicon behaves anisotropically, with the minimum stress occurring at a 45 degree angle from the [110] direction.

3.2 (2D) Stationary Linear Elastic Model

Due to computational restraints the meshing conditions and curve smoothness reported in the Tompkins et al. study were relatively poor, and it was pointed out that further discretization of the individual curves could help further advance this study. To create a valid model for comparison, a more powerful computer running the newest available software (COMSOL Multiphysics 5.2) was used to refine and obtain more accurate values in this work. 2D and 3D linear elastic models under the stationary mechanics module in COMSOL Multiphysics 5.2 were used to evaluate the influence of serpentine geometry and mechanical anisotropy of (0001) GaN and (100) Si on crystalline stretchable behavior. The physics, boundary conditions, and material properties are selected to mirror the conditions in the previous reported simulations (2; 47). The results presented in this work are expected to be more accurate due to a better discretization of curved geometries, which lead to finer meshing conditions, more accurate modeling results, and later finer anisotropic etching profiles.

3.2.1 Numerical Model Input Parameters to Evaluate the von Mises Peak Stress

The 2D simulation geometries, boundary conditions, anisotropic variables, and meshing conditions are discussed below.

3.2.1.1 Serpentine Geometries and Materials
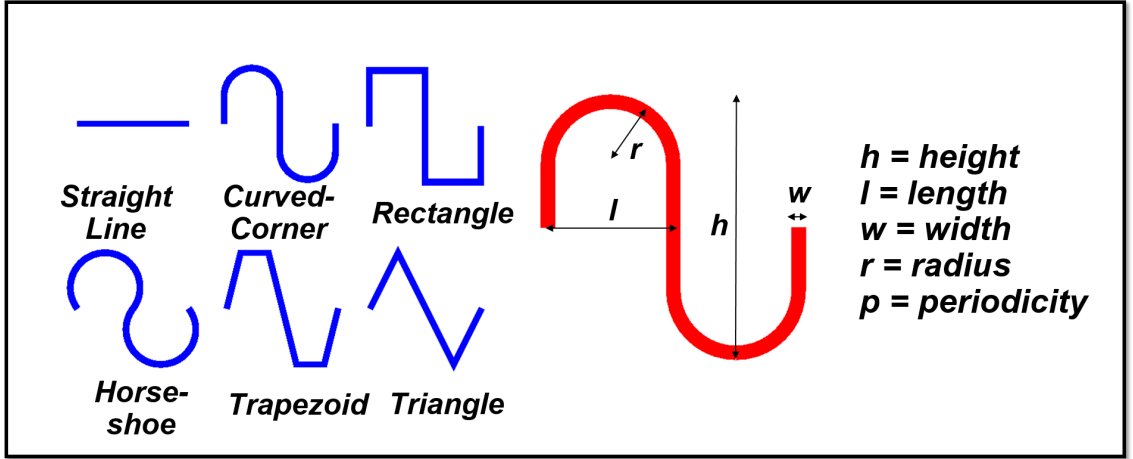
Figure 3.1: **Serpentine geometries analyzed in this Thesis: Straight, Curved Corner, Rectangle, Horseshoe, Trapezoid, and Triangle.** The geometrical parameters modeled in this work are the amplitude height (h = 1 mm), wavelength or length (l = 1 mm), width (w = 25 μm, 50 μm, 100 μm, 150 μm), arc radius (r = 250 μm), and number of periods (p = 5, 10).

The mechanical performance of five serpentine geometries (Horseshoe, Rectangular, Curved Corner, Triangle, and Trapezoid) are analyzed in comparison to a traditional straight geometry, as shown in Figure 3.1. The dimensions and model input parameters are intended to replicate the conditions used in the Tompkins et al. study (2). First a 10 period Si or GaN trace with geometrical dimensions of amplitude height (h = 1 mm), wave length (l = 1 mm), arc radius (r = 250 μm), trace width (w = 25, 50, 100, 150 μm), and trace thickness (t = 7 μm), is constructed into the respective serpentine geometries, is embedded within a rectangular (3 mm x 10 mm x 15 μm) elastomer substrate. Sylgard 184 (Dow Corning) was chosen as the stretchable substrate for this study because it's a PDMS based polymer often used as a substrate material which offers mechanical protection and is assumed to have superior isotropic stretchable behavior, reaching intrinsic tensile strains of up to 40% (34). The material properties used in the following mechanical simulations are shown in Figure 3.2

Material Properties:	(100) Si <100> direction	(100) Si <110> direction	(0001) GaN all directions	Sylgard 184
Elastic Coefficients: (GPa)	C11 = 165.7 [1] C12 = 63.9 [1] C44 = 79.6 [1]	C11 = 194.5 [1] C12 = 35.7 [1] C44 = 79.6 [1]	C11 = 390 ± 15 [3] C12 = 145 ± 20 [3] C13 = 106 ± 20 [3] C33 = 398 ± 20 [3] C44 = 105 ± 10 [3] C66 = 123 ± 10 [3]	NA
Young's Modulus:	130 GPa [1,2]	169 GPa [1,2]	297 GPa [4]	1.32 – 2.97 MPa [5]
Density (kg/m^3)	2330 [1]	2330 [1]	6095 [3],	695 [5]
Poisson's ratio	0.278 [1]	0.064 [1,2]	0.14 to 0.37, average 0.23 [4]	0.45 [5]
Isotropic or Anisotropic	Anisotropic	Anisotropic	Isotropic	Isotropic

[1] Hopcroft, Matthew A., William D. Nix, and Thomas W. Kenny. "What is the Young's Modulus of Silicon?." *Journal of microelectromechanical systems* 19.2 (2010): 229-238.
[2] W. A. Brantley, "Calculated elastic constants for stress problems associated with semiconductor devices," Journal of Applied Physics, vol. 44, pp. 534-535, 1973.
[3] Polian, A., M. Grimsditch, and I. Grzegory. "Elastic constants of gallium nitride." *Journal of Applied Physics* 79.6 (1996): 3343-3344.
[4] Krost, A., et al. "GaN-based epitaxy on silicon: stress measurements." *physica status solidi (a)* 200.1 (2003): 26-35.
[5] Johnston, I. D., et al. "Mechanical characterization of bulk Sylgard 184 for microfluidics and microengineering." *Journal of Micromechanics and Microengineering* 24.3 (2014): 035017.

Figure 3.2: **Material properties used to model anisotropy in the linear elastic model** The geometrical parameters modeled in this study are the amplitude height (h = 1 mm), wavelength or length (l = 1 mm), width (w = 25 μm, 50 μm, 100 μm, 150 μm) arc radius (r = 250 μm) and number of periods (p = 5, 10).

3.2.1.2 Boundary Conditions

Next the boundary conditions are defined as follows. A fixed constraint is enacted on one boundary edge of the system, preventing movement in the XYZ directions. The opposite boundary is prescribed a uniaxial displacement of 3 mm in the X direction (parallel to the 10 mm long side of the serpentine trace), while holding the YZ directions fixed. This displacement imposes a constant global strain of 30% while allowing the long ends of the serpentine / elastomer to be free boundaries, not restricted in movement on any axis. As shown in Figure 3.3, after applying uniaxial deformation the serpentine undergoes geometric reconfiguration to relieve stress, and the elastomer deforms as expected due to Poisson's ratio.
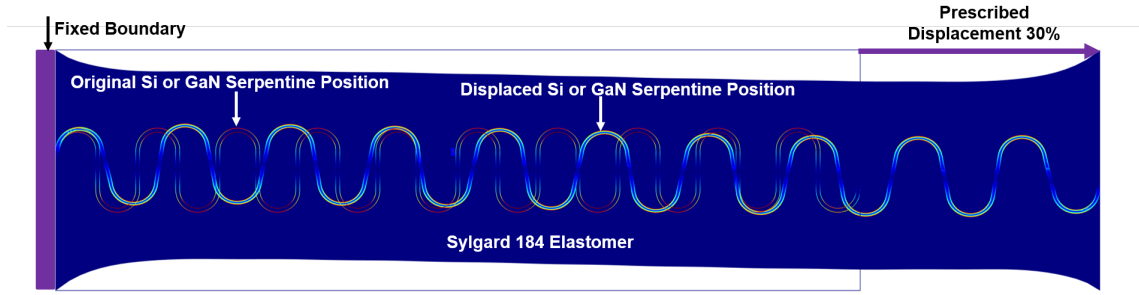
Figure 3.3: **2D COMSOL simulation of a 10 period Si or GaN serpentine trace embedded within a Sylgard 184 elastomer substrate after an applied 30% global strain parallel to the trace** The curved corner serpentine displayed in this image has a width = 50 μm which corresponds to a w/r = 0.2

3.2.1.3 Anisotropic Dependence on the Von Mises Peak Stress

The von Mises peak stresses can then be evaluated after applying a known strain, given the stiffness tensor of the material, which is related to the geometry and Youngs modulus, as described in section 2.4.2. Stress is related to strain through Hookes Law for a continuous media, Eq 3.1.

$$\sigma_{ij} = C_{ijkl}\varepsilon_{kl} \tag{3.2}$$

where σ_{ij} is the stress, ε_{kl} is the applied strain, and C_{ijkl} is the stiffness tensor, derived for each rotation using the equations in 2.4.2. The stiffness tensor is used to describe the anisotropic mechanical properties of a material at certain crystallographic orientations, Eq 3.2. The stiffness is effectively the Youngs Modulus of the material at a specific crystallographic orientation, and it is directly proportional the stress at a given strain.

The yield stress, also referred to as the intrinsic tensile stress, is the maximum internal force a material can undergo prior to fracture. The yield stress (σ) for Si is 7 GPa and using the Young's modulus ($E_{110} = 169$ GPa) and Hooke's law ($\sigma = E\varepsilon$), we can calculate the tensile strain (ε) of Si (i.e 7 GPa / 130 GPa = 0.04 = ε). This value is expected to be slightly higher for GaN, due to a stiffer Young's modulus, however, there is currently not a universally accepted value for GaN. After applying

a strain of 30% parallel to the trace, we want to ensure we are operating in the linear elastic regime, which occurs when the stress within the system is far below the yield stress of the material. If the von Mises peak stresses reported in the system are lower than the yield stress of the material, the system is considered reversibly elastic, and is suited for use in stretchable electronics. To compare the mechanical performance of each geometry in Figure 3.1, we analyzed the maximum Von Mises peak stress distribution. This is a convenient average of the three principal stresses of the material governed by Equation 3.3, which is a function of the stiffness tensor at a certain crystallographic orientation.

$$\sigma_v = \frac{\sqrt[2]{(\sigma_1 - \sigma_2)^2 + (\sigma_2 - \sigma_3)^2 + (\sigma_3 - \sigma_1)^2}}{2} \tag{3.3}$$

3.2.1.4 Meshing Conditions

After applying a 30% strain parallel to the trace on the Curved Corner structure, the von Mises peak stress was evaluated as a function of number of mesh points. Like most FEM softwares, COMSOL Multiphysics offers a range of meshing conditions (extremely coarse to extremely fine) which changes the number of mesh points. Figure 3.4 shows the 2D mesh convergence plot results on the maximum von Mises peak stress on the Curved Corner serpentine structure embedded within Sylgard 184 after applying a 30% strain. As the number of mesh vertices increased from 1,300 to 14,000 points the von Mises peak stress decreased by 3 percent.

2D Mesh Convergence Plot of [110] Curved Corner Si Serpentine
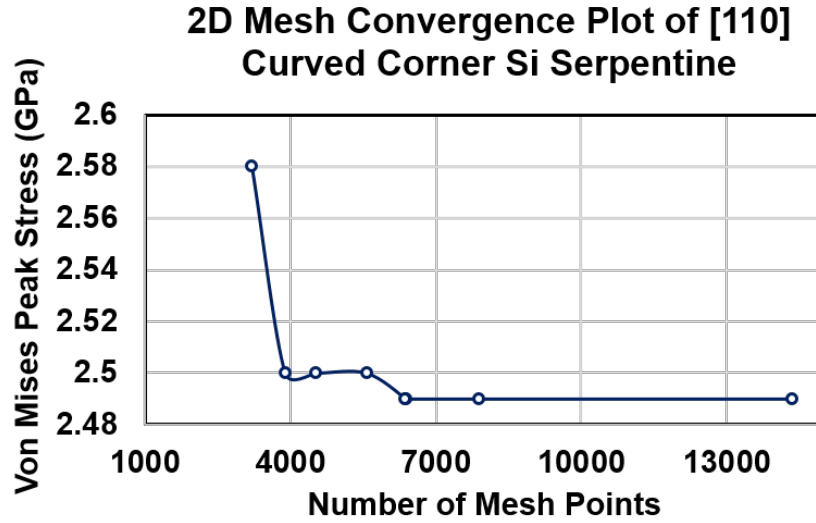
Figure 3.4: **2D COMSOL Mesh Convergence Plot** The von Mises peak stress value is reported as a function of number of mesh points after applying a 30% strain parallel to the trace.

After performing this mesh convergence test, the finest mesh element size was elected which ranged between 12,376 and 28,322 mesh points, depending on the simulated serpentine geometry. This is a 9-21 % increase in number of mesh points per geometry than used in the study reported by Tompkins (11,320 - 22,401 points), which is most likely due to improved discretization of the curves from importing geometries directly from CAD as opposed to building them in the COMSOL software.

Once all boundary conditions are properly defined, the geometry is discretized into extremely fine triangular mesh points, with a zoomed in view of a single period shown in Figure 3.5. This figure also shows the Curved Corner structure concentrates stress in the regions with the largest change in curvature which occurs at the amplitudes maximum and minimum. This is the location where peak stress is predicted to be the highest, and it is likely the failure location of the structure.
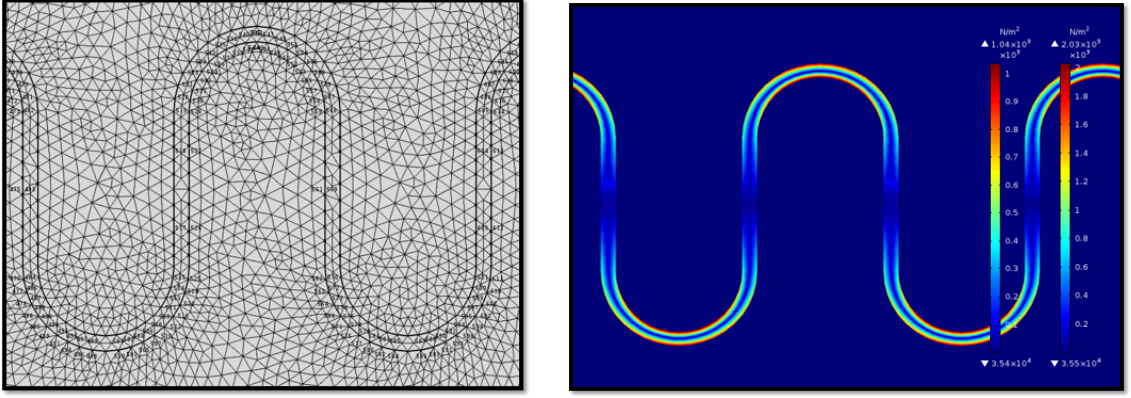
Figure 3.5: **Meshing conditions and COMSOL Multiphysics stress output of Curved Corner serpentine.** (left) Image showing the triangle mesh used for FEM simulation. The serpentine geometry under analysis is a Curved Corner with a 1000 μm peak-to-peak amplitude, 1000 μm wavelength, a 50 μm width and 7 μm thickness. (right) Typical von Mises peak stress distribution output of a 1000 μm amplitude Curved Corner serpentine structure, after a 30% strain applied parallel to the trace.

3.2.2 Effect of Serpentine Geometry on Stretchable Behavior of (100) Silicon and (0001) Gallium Nitride

The output of the von Mises peak stress distribution on a 1000 μm amplitude curved corner is shown in Figure 3.5. The stress distribution of the other tested serpentine geometries (Rectangle, Horseshoe, Trapezoid, and Triangle) are shown in Figure 3.6. In agreement with prior simulations (2; 48; 58) the maximum peak stresses were found to concentrate in the regions with the largest change in curvature. Thus, the highest peak stress occurs at the maximum and minimum of the amplitudes in the Curved Corner geometry, and along the beams parallel to the applied strain for the Rectangular geometry.
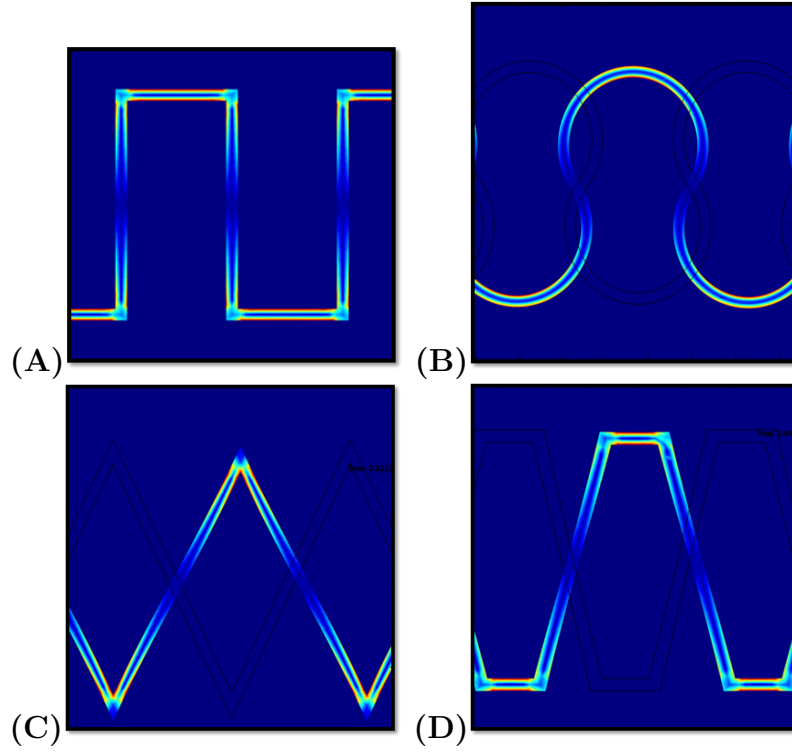
Figure 3.6: **Von Mises peak stress distribution on four tested serpentine geometries**
A.) Rectangle B.) Horseshoe C.) Trapezoid D.) Triangle after a 30% strain applied parallel to the trace.

Due to minor variations in meshing and boundary conditions, the program tends to concentrate the peak stresses on the periods closest to the boundary edges which could cause the program to output higher peak stresses values than the true peak stress. To account for this potential source of error in our data, we developed a MATLAB script that systematically removes data related to edge effects, outputting the true value and location of the maximum peak stress on the structures. In these simulations, it was found that after applying a 30 percent strain, the Si curved corner structure (Figure 3.5) had a peak stress of 2.1 GPa, and GaN Curved Corner structures had peak stresses of 4.76 GPa. The stresses are much lower in the Si structure than GaN because Si is a less rigid material, described by its lower stiffness tensor and lower elastic modulus. Similarly, the von Mises peak stresses on the rectangular structure (Figure 3.5) for Si and GaN were 1.44 GPa and 3.64 GPa respectively. Figure 3.7 show the maximum von Mises peak stress

of each geometry after applying a 30% strain parallel to the trace, both with and without silicone (Sylgard 184). The maximum stress values for the same serpentine geometries calculated by Tompkins et al (2) are also included in this figure for reference.
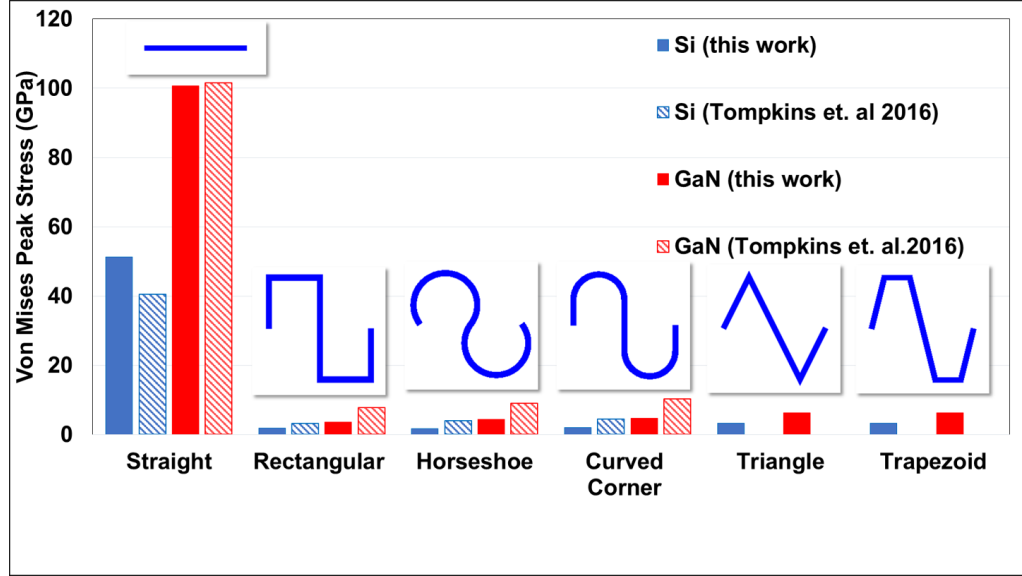
Figure 3.7: **Effect of serpentine geometry on the reduction of peak stress after applying a 30% strain parallel to the trace for single crystal Si and GaN.** Calculated in this work is shown in solid colors, while Tompkins(2) is shown hashed. Note Tompkins did not calculate the Triangle and Trapezoid geometry.

Overall, these results suggest the optimal stretchable geometries are structures with rounded edges such as the Horseshoe and Curved Corner rectangle. Additionally, lowest amount of stress was in the Rectangular structure while the triangular structure concentrated the most amount of stress at all orientations. As expected, stress in GaN serpentine structures is 1.2 - 2X larger than Si, due to the stiffer elastic modulus. While the Horseshoe geometry mechanically behaves the best, the following studies will analyze only the Curved Corner and Rectangular serpentine geometries to explore the effect of anisotropy on geometries with round and sharp edges.

3.2.3 In-Plane Rotation Dependence of (0001) GaN and (100) Si

While the wurtzite and diamond cubic crystal structure of GaN and Si results in overall anisotropic materials, the basal plane (0001) GaN, and (111) Si are known to behave isotopically, while the (100) Si plane behave anisotropically. To verify mechanical isotropic/ anisotropic behavior, in-plane rotations were applied in $10°$ increments from the [0001] direction the (0001) plane of GaN, and similarly rotations in $10°$ increments from the [100] direction on (100) Si, as described in section 2.3.3.

3.2.3.1 Isotropic (0001) Gallium Nitride

After applying these rotations, it was found that the stiffness tensor of GaN is rotationally invariant(i.e $C'_{11} = C_{11}$). After applying a 30% strain and monitor the peak stresses for each in-plane rotations angle in (0001) GaN we see the trend line is flat indicating there is no variation in the stress value. This implies that the mechanical properties behave isotropically in the (0001) growth plane of GaN, due to 6-fold crystal rotation symmetry, which is highly desired in stretchable systems.
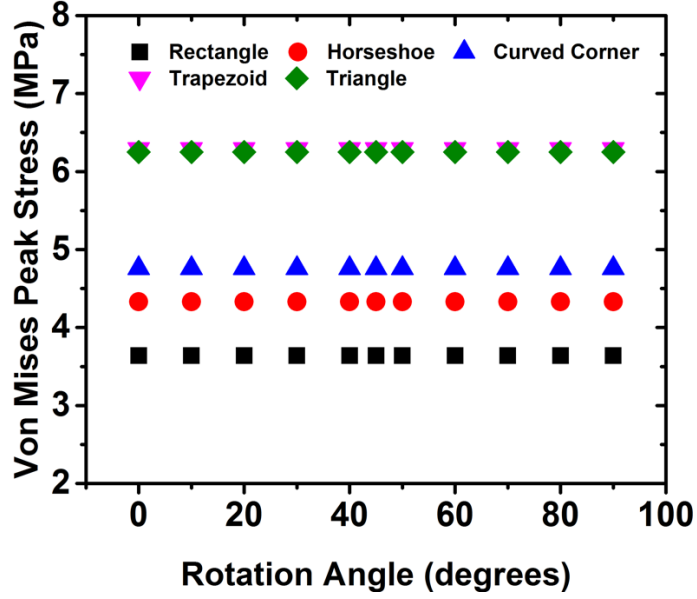
Figure 3.8: **Maximum von mises peak stress value for all serpentine ge-
ometries as a function of in-plane rotations on (0001) GaN serpentines
after applying a 30% strain.** No variations in the maximum stress indicates GaN
serpentines behave isotropically in the (0001) plane.

3.2.3.2 Anisotropic (100) Si

To evaluate the influence of anisotropy within (100) Si, in-plane rotations
were also applied in 10° increments about the [110] direction. It was found that the
stiffness tensor had a strong anisotropic dependence, exhibiting 4-fold rotational
symmetry(i.e $C'_{11} = C_{11}$ only for 90° rotations). As shown in Figure 3.9, for all Si
serpentine geometries, rotations 0° and 90° from [110] direction result in the highest
peak stress which indicates this crystallographic orientation would have the lowest
$Stretchability$ (ε^{cr}_{app}).
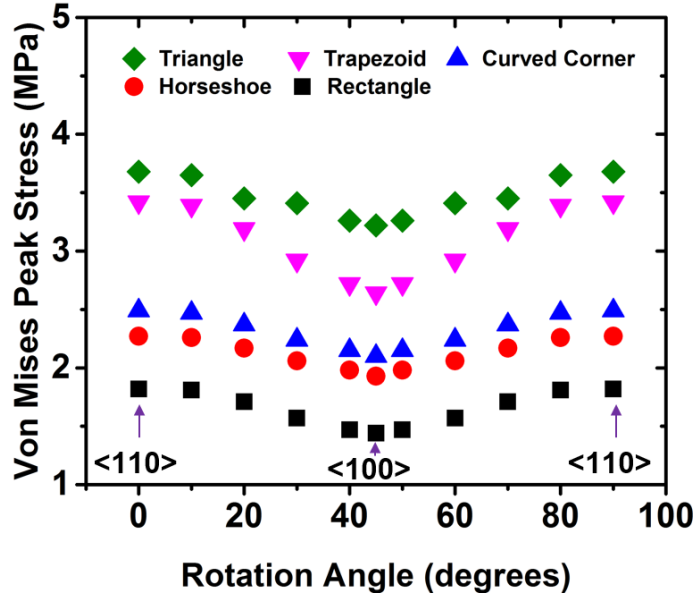
Figure 3.9: **Maximum von Mises peak stress as a function of in-plane rotations on (100) Si serpentines after applying a 30 % strain.** The large variations in the maximum stress indicates the serpentines behave anisotropically in the (100) plane with the <110> direction corresponding to the least amount of stress.

The plot shows that the maximum stress occurs at the [110] direction, which is the cleavable direction parallel(0°) and perpendicular (90°) to the wafer flat. As we move in 10° degree rotations away from the [110] direction at 0°), the peak stresses gradually decrease until we reach the minimum at the 45° angle at the [100] direction. As we continue to the increase the rotation angle from 45° 90° the peak stresses begin to increase symmetric about the [100] direction back to the maximum stress at [110].

These results indicate that if one were to fabricate identical stretchable serpentines geometries on a (100) Si wafer along different crystallographic orientations (i.e <110> and <100>), the mechanical performance would dramatically differ. This is because the elastic modulus of silicon is dependent on its crystallographic orientation, therefore the stiffness tensor also has a crystallographic orientation de-

pendence.

3.2.4 Stretchability of (100) Silicon in the <100> and <110> directions

The most important design parameter in a stretchable system is the maximum percent elongation (ε_{app}^{cr}) it can withstand before the formation of cracks which can subsequently lead to fatigue, fracture and device failure. For wearable electronic applications, these materials must be elastically stretchable, which means they need to maintain full electrical and mechanical performance after cycling tens of percent strain, without fatigue or fracture in the system. Any deformation imposed on the stretchable system must be able to stretch and compress reversibly, by a minimum of 30% strain for most wearable electronics applications, but could require reversible deformation of us to 100s% strain in some locations such as behind the knee. We are interested in determining the maximum end-to-end displacement (global elongation) of Si serpentines in the <100> and <110> directions as a function of the structures width-to-radius (w/r) ratio, as shown in Figure 3.10.
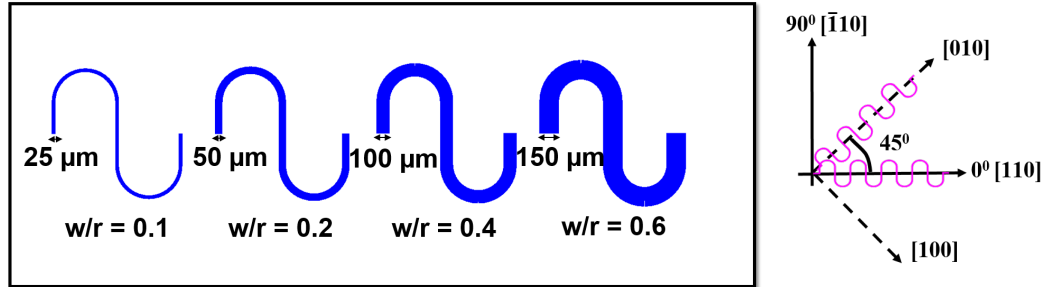
Figure 3.10: **Width-to-radius (w/r) ratios analyzed** Increasing the width of serpentine traces from 25 μm to, 50 μm, 100 μm, and 150 μm, increases the w/r from 0.1 to, 0.2, 0.4, and 0.6

To evaluate the dependence of crystallographic orientation on the stretchability (maximum tensile strain) of the serpentines, I investigated two geometries, Curved Corner and Rectangle, varying the geometrical parameter of the width-to-radius ratio (w/r). When the width of the device is much thinner than its length (w < < l) under deformation, the atomic planes slip in the transverse direction to

accommodate induced stress which promotes a geometrical reconfiguration. I varied the width of the serpentine trace from 25 μm, 50 μm, 100 μm, and 150 μm, which changed the (w/r) from 0.1, 0.2, 0.4, and 0.6. Figure 3.11 shows the effect of anisotropy on the maximum tensile strain of a silicon Curved corner trace patterned in both the <100> and <110> directions at various w/r ratios.
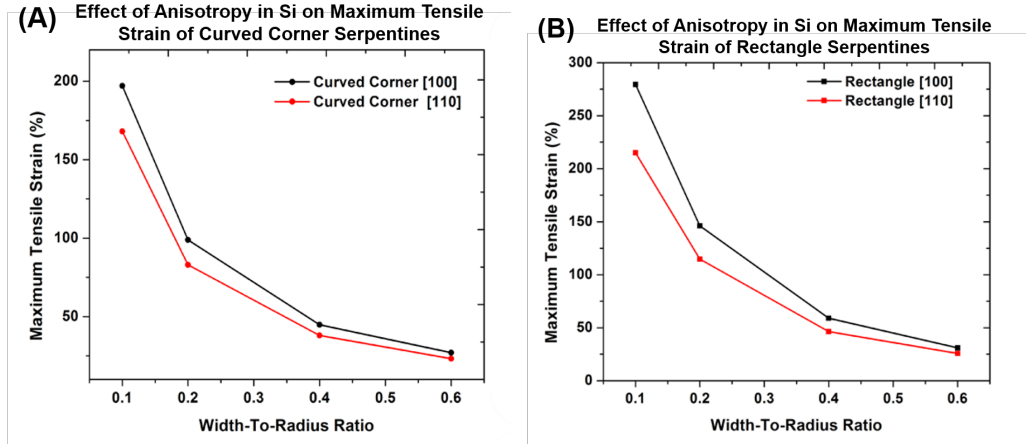
Figure 3.11: **Effect of anisotropy and width-to-radius ratio in Si on stretchable behavior for the Curved Corner and Rectangular serpentines.** Lower (w/r) ratios are 10 - 26% more stretchable than large (w/r) ratios. Both plots demonstrate the maximum tensile strain of the serpentine geometries are dependent on the crystalline anisotropy and plane it is patterned on and on its width. A.) Demonstrates the Curved Corner tensile strain can vary due to mechanical anisotropy by 12-25% while B.) demonstrates the Rectangle varies by 25-30%.

Under applied tensile strain, it's been reported that free standing serpentines with a small width-to-radius (w/r) ratio have more degrees of freedom which allows ribbons to flex, buckle out of plane and twist to accommodate deformation under applied strain, while serpentines with a large w/r tend to be restricted to in-plane deformation (37). The results shown in Figure 3.11 indicate serpentine geometries with smaller widths (w/r = 0.1) can reach global end-to-end displacements 2.75X their original length. However, larger widths (w/r = 0.6) increase the stiffness of the serpentine geometries which only allow for elongations 0.3X their original length. Additionally, these results indicate the [100] direction is the most stretchable for Si, where serpentines patterned in the [100] direction can be up to 12-30% more stretchable than serpentines patterned in the [110] direction. This is primarily due

to the [100] being the closed packed direction for the (100) plane, giving additional molecules to slip to accommodate stress in the system, so it can achieve higher strain percentages. Herein, we will be working with Si and GaN serpentines of a 50 μm width which corresponds to a w/r ratio of 0.2.

3.3 (3D) Stationary Linear Elastic Model

There were some assumptions made in the 2D model, which may not reflect true experimental conditions such as the serpentine is confined only to in-plane (2D) deformation, and that all periods of the serpentine will stretch uniformly. In order to more accurately model the experimental conditions, a 3D linear elastic COMSOL Multiphysics 5.2 model is employed to analyze any out-of plane (Z-axis) buckling deformation mechanisms on a free standing 5 period curved corner serpentine with h = 1 mm, l = 1 mm, w/r = 0.2, t = 7 μm. I repeat the same mesh convergence test in the 3D model, testing mesh vertices's ranging between 1200 - 120000 points. This is a large improvement in the number of points from the 2D model. Shown in Figure 3.13, there is a non-linear variation in the value of stress with increasing number of mesh points, which is on average 33% higher than the values reported by the 2D model. I will point out however, the 3D model is not fully converged.
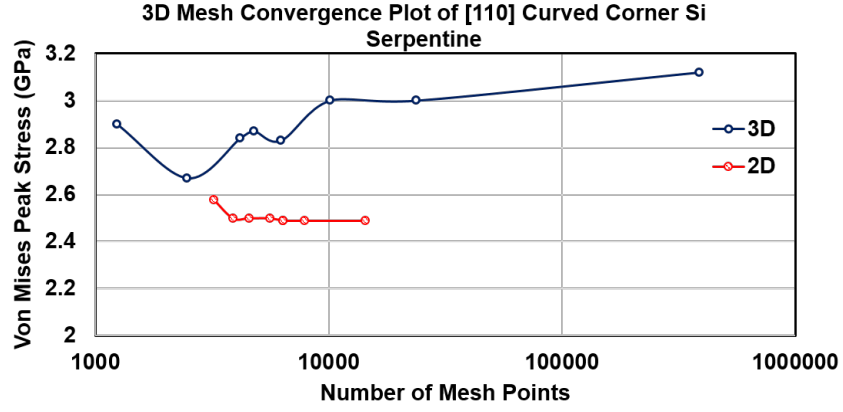
Figure 3.12: **3D mesh convergence test.** The von Mises peak stress value is reported as a function of number of mesh points after applying a 30% strain parallel to the trace. The 2D mesh convergence data is also plotted for reference.

Next, I evaluate the effect of mechanical anisotropy on the maximum global tensile strain of the Curved Corner serpentine in the <100> and <110> directions. The maximum global strain is the maximum end-to-end displacement Si reaches before the internal stress exceeds 7 GPa, similar to the methods performed on the 2D model. The COMSOL result of the non-uniform straining profile on the Si Curved Corner serpentine in the <100> is shown in Figure 3.13.
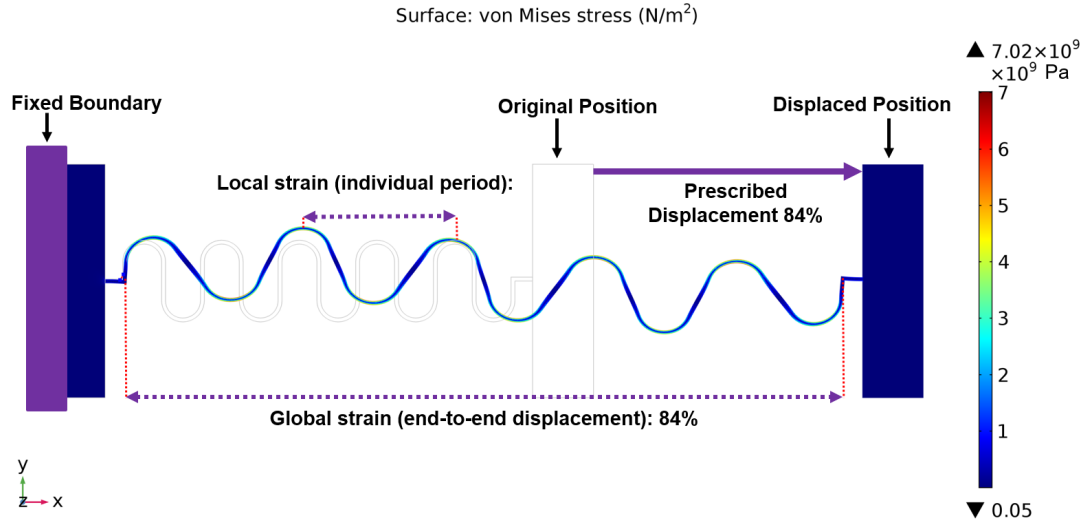
Figure 3.13: **3D COMSOL model of a free standing 5 period <100> Si Curved Corner serpentine trace stretching to a maximum global strain of 84%.** The left boundary edge of the rectangular post is held fixed while the other end is displace by 4.2 mm which corresponds to an end to end displacement of 84%.

Repeating this for the <110> we find a slightly lower tensile strain at 70%. Figure 3.14 shows the fracture location of the serpentine with respect to crystalline anisotropy, with <110> Curved Corner serpentines breaking at the Amplitude for both the 2D and 3D model, while the <100> Curved Corner serpentine fractures at the Bend in the 3D model. The end-to-end displacement tensile strain percentage and fracture location variations between the 2D and 3D model are summarized in Figure 3.15.
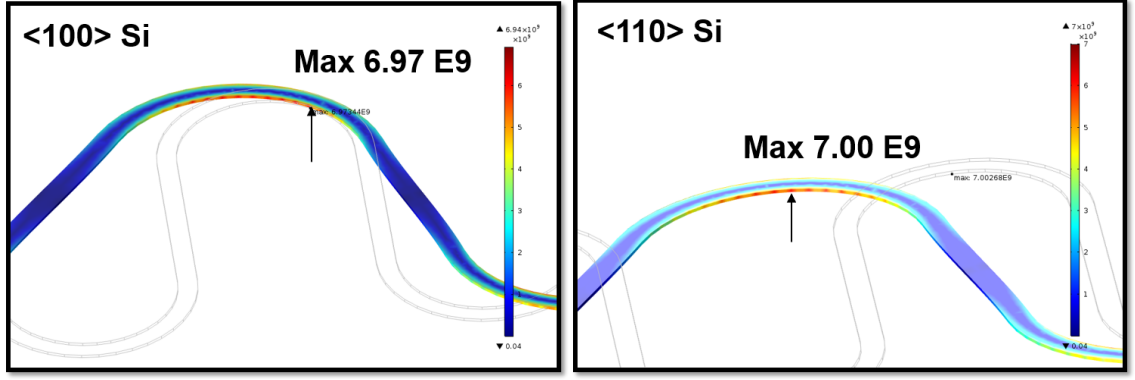
Figure 3.14: **3D FEA modeling results demonstrating the fracture location of <110> and <100> Si Curved Corner serpentines.** The <110> direction is shown to break at the amplitude location in the 3D model, while the <100> fractures at the arc bend. The 2D model originally predicted fracture at the amplitude for both orientations.

	2D Model	3D Model
<110> Si	84% (amp)	70% (amp)
<100> Si	101% (amp)	84% (bend)

Figure 3.15: **2D and 3D FEA modeling results comparison of the maximum end-to-end displacement (tensile strain) of <110> and <100> Si serpentines.** 2D and 3D tensile strain ($\epsilon\% = \frac{\Delta L}{L}$) and fracture location results are compared, showing the 3D model on average out-puts tensile strain 17% higher than the 2D model.

3.4 Modeling Crystalline Stretchable Behavior Summary and Conclusions

Major design insights on the mechanical behavior GaN and Si serpentines were provided through the 2D and 3D COMSOL 5.2 simulations performed. All serpentine geometries tested for both GaN and Si resulted in a peak stress reduction of 20 - 98%, from convention straight geometries, showing these structures are well suitable for use in wearable electronics. Curved geometries (Horseshoe and Curved Corner) experience more gradual change in peak stresses due to the gradual change in curvature along the structure, thus displaying overall lower stresses than geome-

tries with sharp corners. Anisotropy in Si plays a signifiant role on the stretchable mechanics, displaying four-fold symmetry in the (100) plane, with the [110] crystallographic direction (0°), containing the highest peak stresses, while [100] at the 45° rotations result in the lowest peak stresses. I demonstrate this anisotropic dependence could result in tensile strain variations of 12 - 30% for the Curved Corner and Rectangular geometries (w/r = 0.1 - 0.6). Additionally, I showed GaN displays isotropic behavior in the (0001) plane, which indicates uniform stretchable behavior regardless of crystal orientation. This isotropic property is highly desired when fabricating stretchable devices which rely on contact photolithography where slight misalignments are common.

There was a discrepancy on the maximum tensile strain of 17% between the 2D and 3D models. Since the mesh converged linearly for the 2D model, but did not fully converge on the 3D model, it is assumed that the 2D model more accurately represents the local surface stress concentration. The additional degree of freedom provided by the 3D model most likely will portray the out-of-plane deformation expected on the trace while under applied deformation. Another potential source of error that could be the reason for this discrepancy is the models assume the starting material (Si or GaN) is a relaxed single crystal patterned into a perfect serpentine geometry. In general, the crystalline materials will have inherent stress from the substrate, for instance, Si will be released from a silicon-on-insulator (SOI) wafer, which generally induces inherent compressive stress. Similarly, GaN will be released from a sapphire wafer (induced compressive stress) or a silicon wafer (induced tensile stress). While FEA is a powerful tool for stretchable design, one shortcoming of relying solely on FEA data is these modeling results do not factor in initial residual stresses present from material growth or device manufacturing. Thermal and mechanical stresses present in the material from micro-processing can lead to the nucleation and propagation of dislocations, and formation of cracks and voids. Presence of these stresses directly from fabrication can ultimately lead to premature failure of the devices, which is generally not predicted by the model. Therefore; experimental verification of these results is crucial to understanding crystalline stretchable

41

behavior.

Chapter 4:   Microfabrication of Stretchable Crystalline Serpentine Structures

Chapter 4 presents the novel experimental procedure details of the fabrication process I developed which allows for the fabrication and release of stretchable Si serpentine mechanical test structures. The freestanding Si serpentine test structures were fabricated through a combination of standard micro-machining processes, such as photolithography, backside alignment, and a two step inductively coupled plasma (ICP) deep reactive ion etch (DRIE) process, in the Class 10 and 100 Nanofabrication Center at the U.S Army Research Laboratory. Si serpentine mechanical test structures are fabricated in both the <100> and <110> crystallographic directions, from a (100) silicon-on-insulator wafer, which will allow us to evaluate the influence of crystalline anisotropy on stretchable behavior. While this fabrication process is compatible with many geometrical parameter, height (h), length (l), width (w), radius (r), thickness(t), Curved Corner and Rectangular serpentine structures are fabricated to reflect the conditions imposed by the FEA model (h = 1 mm, l = 1 mm, r = 250 μm, w = 50 μm, and t = 7 μm) presented in Chapter 3. Additionally, a fabrication and release process is proposed which would allow the development of serpentine mechanical test structures from (0001) GaN. The processes described here can be adapted to allow the fabrication and release of most III-V material into a serpentine structure, if epitaxially grown onto a Si substrate. We also demonstrate one sided metalization (2 μm NiTi) onto the Si serpentine post release, which could be then undercut and removed to leave freestanding NiTi. We speculate that researchers could adapted this process to release other thin-film materials that have yet to be explored by the stretchable electronics community. The non-uniform

stress distribution along multiple locations of the fabricated and released Si Curved Corner serpentine structures will be evaluated while applying external strain via micro-Raman spectroscopy in Chapter 5.

4.1 State of the Art Fabrication Approaches to Enable Flexible and Stretchable Si and GaN

Vast strides on the production of flexible and stretchable single crystal semiconductor devices has been made over the last 20+ years, allow functional inorganic crystalline materials to be integrated into high-performance stretchable electronics (41), (30). Through these methods, silicon has been incorporated into many flexible/ stretchable applications including lateral pn junction diodes (18), a hemispherical electronic eye camera (12), structural health monitoring (60), sensors for prosthetic skin (61), and photovoltaics (41). Flexible gallium nitride has been integrated into applications such as flexible RF AlGaN / GaN high electron mobility transistors (HEMT) on plastic substrates (62; 63; 64; 65), and flexible optoelectronic devices (66). Additionally stretchable GaN LEDs were demonstrated using an island-bridge layout (67). To the best of our knowledge, to date our group is the first to develop stretchable GaN devices into serpentine configurations to enable stretchability within the crystal (3).

4.1.1 Methods to Enable Flexible / Stretchable Si

Due to the high temperature requirement for inorganic semiconductors processing, crystalline materials cannot be simply grown directly onto a pre-strained stretchable substrate. Instead, one method developed by the John Rogers group in 2006 was to process thin Si and GaAs nanoribbons on the wafer and then use a transfer stamp to bind them to a pre-strained substrate. Similar to the previously reported methodologies used for metals, when tension is released from the elastomer substrate, the crystalline ribbons periodically buckle out-of-plane, which could reach tensile strains of up to 100%, and compressive strains of 25% (68). Another example

they developed to enable stretchable Si used standard photolithography techniques to pattern thin silicon ribbons (20 to 320 nm) on a silicon-on-insulator (SOI) wafer, and use etching techniques to release the ribbon from the underlying SiO_2 layer. Next, a pre-strained elastomeric support is bonded to the silicon ribbon, which can now easily peel off of the SOI wafer. Once the strain is released on the elastomer, the Si ribbons spontaneously buckle into highly ordered, periodic wavy structures which can repeatedly cycle -11% compression to 11% tension (30). While these methods successfully allowed for the fabrication of stretchable crystalline materials they are restricted to very thin Si device layers (< 500 nm), and the out-of plane wavy buckling presents challenges for any further device processing. At very low widths and thicknesses, thin Si serpentine ribbons tend to undergo out-of-plane buckling deformation which limits the available characterization techniques, and potential device applications. Moreover, these methods requires device encapsulation into an elastomer support for mechanical protection, as opposed to allowing a free-standing released structure, which creates challenges during device performance testing.

The MEMS community has developed many fabrication procedures utilizing isotropic and anisotropic etching processes which allow for suspended Si structures (69). For example, auxetic geometries display a negative Poisson's ratio under tension, which makes them highly deformable under applied strain. Auxetic Si was developed using an SOI wafer where the Si device layer was directionally etched into the defined auextic structure using fluorine-based gas in deep reactive ion etching (DRIE). Next, the buried oxide and underlying Si layers were isotropically etched to undercut the structure, allowing for a released auexetic Si piece. To develop a free standing Si serpentine, I will be adapt anisotropic dry plasma etching techniques.

4.1.2   Methods to Enable Flexible / Stretchable GaN

AlGaN/ GaN high electron mobility transistors (HEMT) are a promising solution to wearable wireless power management, however, the semiconductors inability to stretch or bend significantly presents challenges. Since the most brittle component of HEMT devices are the inorganic semiconductor, this becomes the limiting mate-

rial in an integrated stretchable system. Our group is interested in using serpentine structures to fabricate stretchable AlGaN/GaN HEMT free standing structure as opposed to encapsulated in an elastomer (3). In this chapter, I propose a fabrication process that would allow for the release of free standing AlGaN / GaN serpentines.

GaN patterned on Si substrates is an advantageous for designing flexible and stretchable GaN devices because of the etch selectivity, Si will etch in fluorine based chemistries while GaN etched in chlorine based gases. Lv et al demonstrated a process that allowed for suspension of a large area GaN micro-structures using a two-step dry release process. First a Cl_2- based ICP-DRIE etch is performed define the AlGaN / GaN mesa structure. Next an anisotropic ICP etch is performed to create vertical profile side walls within deep Si trenches based on SF_6 / O_2 / C_4F_8. The trench was then exposed to an isotropic plasma etch which released and suspended the large area GaN structure from the Si wafer (70). Similar methodologies to release GaN from Si are also reported in (71; 72).

Lee and coworkers were the first to investigate ways to increase the flexibility of GaN. They successfully fabricated and released a flexible AlGaN/ GaN HEMT from its Si substrate. Taking advantage of the fact that AlGaN / GaN HEMT devices are thin films, they can withstand flexing forces, if removed from their bulk substrate. To achieve this, they developed a procedure which uses standard top-down processes to fabricate the device, release it from a Si substrate, and then transferred it to a flexible substrate (polyethylene terephthalate) (65). Defrance et al. were the first to investigate the radio frequency (RF) performance of AlGaN/GaN HEMTs on flexible substrates (63). They developed a method to successfully fabricate and release a HEMT device from a Si substrate without roughening the surface. After lithographically processing the HEMT device onto a Si wafer, the front side of the HEMT is temporarily bonded to a handling wafer, and the silicon substrate was removed by mechanical lapping followed by a selective Xeon difluoride etch (XeF_2). They measured the direct current characteristics of the device before and after the transfer and found the current density decreases with the transfer which they attribute to the poor thermal conductivity of the stretchable substrate. Another

interesting finding of this group was the 2DEG concentration actually increases with bending due to the induced piezoelectric polarization in AlGaN and GaN (63). These results lead us to believe stretchable serpentine structures will increase the 2DEG concentration under tensile stresses.

4.2 Fabrication Process of <100> and <110> Serpentines from (100) Silicon

While there are modeling efforts investigating the mechanical performance of free standing Si into 2D planar serpentine structures, fabrication and experimental verification is limited (2; 16). This work produces 2D in-plane serpentines structures, as opposed to buckled out-of-plane 3D serpentines; therefore, an elastomer substrate is not required to support the serpentine trace during characterization. Single crystal silicon (Si) mechanical test structures were fabricated using (100) silicon-on-insulator (SOI) wafers. As shown in Figure 4.1, devices patterned on a (100) wafer along the standard x and y axis (0° and 90°) are along the <110> family of directions while the <100> family of directions is rotated 45° from the <110>. Serpentine test structures area orientated in both <100> and <110> directions were fabricated by strategically designing a contact photolithography mask plate, using AutoCAD 2013 software, which physically oriented geometries in both the 0° and 45° orientations. The dimensions of each period of the serpentine are: 1000 μm amplitude, 1000 μm wavelength, 50 μm width, and 7 μm thickness.
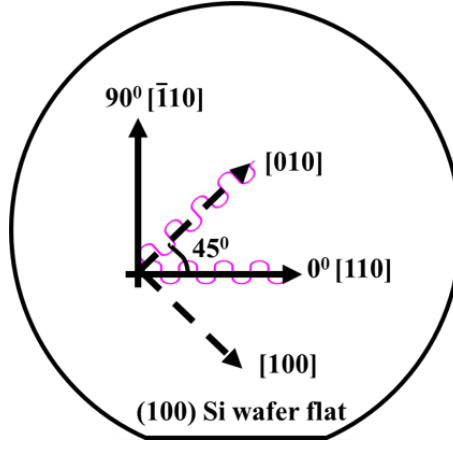
Figure 4.1: **Diagram labeling the angle and family of directions on a (100) Si wafer** Serpentine will be patterned in both the <100> and <110> through physical geometrical tilt in the photolithography mask.

The serpentine structures of interest require a final thickness of 7 μm. While wafers < 10 μm thick are commercially available, they are extremely difficult to handle and transfer during processing, and the materials tend to be costly. Therefore, an SOI wafer was advantageous to use because it separates a thin device layer of Si (7 μm) from a thick handle layer of Si (350 μm) by a sacrificial 3 μm thick oxide. Additionally, SOI wafers are advantageous because they allow one to select the device thickness ranging from a few nanometers up to 200 μm. Each step in a micro-fabrication sequence require careful development and optimization to make the step reliable, repeatable, and cost efficient.

The intention is to eventually characterize the stress/ strain behavior of the mechanical test structures; therefore it is important to take precautionary measures to ensure no external stresses are induced onto the crystal during processing and handling. To realize this, I designed a structure consisting of a thick mechanical rectangular frame which acts as the support to suspend a 7 μm thick serpentine. The long supports parallel to the trace are break away regions that only serve the purpose to provide rigidity during processing. The frame region is a hollow rectangular structure that is intentionally created to provide a mechanically rigid support area to suspend the final serpentine device. The advantage of this support is it helps

48

prevent inducing stresses within the serpentine during general handling and processing. Figure 4.2 shows the process flow I developed fabricate and release <100> and <110> Si serpentine mechanical test structures. This chart presents a summary of the required machinery, materials, and experimental details of each major processing step, while below the chart includes a full description of the fabrication step.
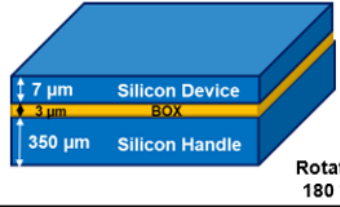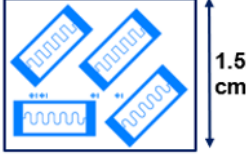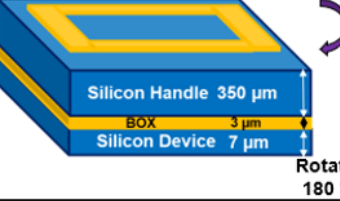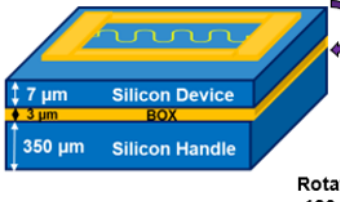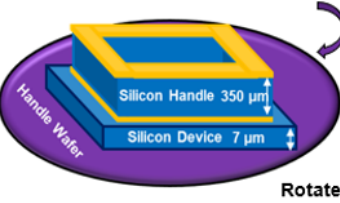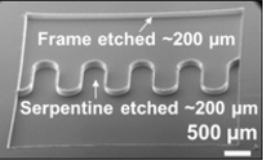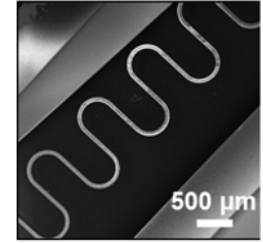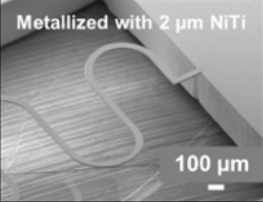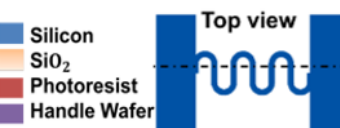
Device Cross Section:	Processing Step:	Processing Step Image:
Rotate 180°	1. Starting Stack: 1.5 cm x 1.5 cm Silicon on Insulator (SOI) chip Si / SiO$_2$ / Si / SiO$_2$ (7 µm / 3 µm / 350 µm / 2 µm)	Top down view of pattern
Rotate 180°	2. Photolithography to pattern frame on the 2 µm SiO$_2$ on the 350 µm Si handle side. BOE 6:1 to etch oxide hard mask.	Patterned Oxide Hard Mask
Rotate 180°	3. PECVD 0.1 µm of SiO$_2$ onto 7 µm Si device side. Photolithography to pattern serpentine and frame structure, BOE 6:1 to etch oxide hard mask.	
Rotate 180°	4. Bond *top side* down to handle wafer via photoresist. Deep Reactive Ion Etch (DRIE) through the 350 µm Si handle and 3 µm BOX layer.	Frame etched ~200 µm, Serpentine etched ~200 µm
	5. Bond *bottom side* down to handle wafer via photoresist. DRIE through top 7 µm Si device layer to release serpentine structure.	
	6. Structure completely stripped of all residual oxide via vapor HF. Post clean, 2 µm of NiTi deposited onto top side of trace.	Metallized with 2 µm NiTi
	7. Clean sample ready for Raman characterization. Frame intentionally broken to allow straining.	

Figure 4.2: **Procedure developed to fabricate and release Si serpentines from an SOI wafer.**

50

1. The starting material is 1.5 cm x 1.5 cm chip from a diced (100) silicon-on-insulator (SOI) wafer (University Wafers). The cross section of the (100) SOI wafer from the manufacturer consists of the following four layers: *top side* silicon device / buried silicon dioxide / silicon handle / oxide *bottom side*. The dimensions of the four layers are *top side* 7 μm Si / 2 μm buried silicon dioxide (SiO_2) / 350 μm Si substrate / 2 μm SiO_2. The SOI wafer is advantageous because our fabrication processes uses use deep-reactive ion etching (DRIE) techniques in later steps, and the middle buried oxide layer (SiO_2) serves as an etch stop to the SF_6-O_2/ CHF_4-O_2 plasma chemistry from the DRIE process, with a selectivity of 40:1 for Si:SiO_2 (73). This SOI wafer structure was strategically chosen for fabrication of a serpentine and a rectangular frame because the built in etch stop layers allow us to fabricate the rectangular structure through the entire thickness of (360 μm) of the SOI stack while leaving a released serpentine suspended in between the rectangular frame (7 μm thick). An top-down view of the photolithography pattern transfered to the entire chip is shown in the processing step image.

2. Since SiO_2 has a good etch selectivity to SF_6/ C_4F_8 chemistry, it was chosen to serve as the etch resistant hard-mask material. First, photolithography was performed to pattern photoresist to etch a SiO_2 hard mask on the *bottom side* (2 μm oxide / 350 μm handle) of the piece. The bottom side pattern consists of the rectangular frame to and alignment marks that will be used for backside alignment later in step 3, without the serpentine suspended. The photolithography and oxide etching procedures are as follows.

Photolithography: First hexamethyldisilizane (HDMS ALDRICH reagent grade > 99%) is spin coated onto the *bottom side* SiO_2 at 3000 rpm for 60 s, and then soft-baked on a hot-plate at 100 $°C$ for 60 s. The advantage of using HDMS is it acts as an adhesion layer by providing a hydrophobic coating the SiO_2 which promotes wetting on the surface from the photoresist. Next, image reversal photoresist AZ5214E (positive process) is spin coated at 3000 rpm for 60 s, soft-baked on a hot-plate at 100 $°C$ for 60 s. Finally, the photoresist covered chip is exposed to UV light under the serpentine mask plate at 9 mW/cm^2 for 8.6 s (Karl Suss MA/BA6),

and is then developed in AZ400K for 20 s.

Oxide Etching: An oxide hard mask of the frame is created by submerging the patterned piece in a solution of 6:1 Buffered Oxide Etch with Surfactant (J.T. Barker UN2922) for 18 minutes. The thickness of SiO_2 results in purple hue in color and is inherently hydrophobic to water, meaning water will not stick to the chip. Etching is complete once the rinse water begins to stick on the piece, becoming hydrophilic, and it will undergo a color change from purple to a blue hue, indicating that the silicon is exposed. At this point the oxide hard-mask etching step is complete and the photoresist is stripped away through a series of acetone, methanol, and isopropanol baths for 1 minute each. This process cleans the wafer, leaving the *top side* (7 μm Si) ready for photolithography patterning.

3. Next, the chip is flipped back over exposing the *top layer* of Si and plasma enhanced chemical vapor deposition (PECVD, Plasma Therm 790+) is used to deposit a layer of 0.1 μm SiO_2. The photolithography procedure is repeated from step 2, and the features on the top of the piece is aligned to the bottom features, using the backside alignment feature on the mask aligner (Karl Suss MA6). The topside features also contain the mechanical frame, alignment marks, and serpentine structure in the respective geometry patterned in between the rectangular frame. After the photoresist is patterned and developed, the top oxide hard mask is patterned by repeating the oxide etching process in step 3, by submerging the part in 6:1 Buffered Oxide Solution, this time for 30 s due to the thinner oxide layer etching faster. The photoresist strip and cleaning procedure is then repeated from step 2.

4. Next, the chip is bonded *top side* facing down into a 4 in Si handle wafer, using a thick layer of photoresist (10 μm AZ9245) for adhesion between the chip and the handle wafer. Inductively Coupled Plasma Deep Reactive Ion Etching with SF_6 and C_4F_8 gas chemistries (ICP DRIE, PM1 Plasma Therm Versalock 700), was used to anisotropically etch through the 350 μm Si handle to define the hollowed rectangular frame on the backside of the SOI chip. The parameters of the DRIE etching include RF power of 850 W with C_4F_8 / SF_6 / Argon (70/0.5/40 sccm) gas on for 4 seconds to passivate and C_4F_8 / SF_6 / Argon (0.5/100/40 sccm) gas on for

6 seconds to etch, cycled for 1.5 hours. The helium cooler pressure was kept at 4000 mTorr the entire time.

The first silicon etch is complete once the buried oxide layer was exposed, indicated by a color change from dark blue to purple. The oxide layer was removed using anisotropic dielectric plasma etching (PM3 Plasma Therm Versalock 700) with gas chemistries. Once the top silicon layer is exposed, indicated again by a color change to dark blue, the wafer is submerged into acetone for 10 hours to de-bond the piece part from the handle wafer. The structure at this point is very fragile with extra care taken to clean it with acetone, methanol, and isopropanol then allowed to dry on a hot plate at 100 $°C$. Air drying with N_2 is not advised, due to the high pressure of the air. The image of the process at this step shows the deep etch of both the frame and serpentine, however, the process only etches the rectangular frame at this step.

5. Next the *bottom side* of the chip is bonded to the handle wafer using photoresist (10 μm AZ9245). Again, using the ICP DRIE (Plasma Therm Versalock 700), the 7 μm of Si on the *top side* anisotropicly etched for 15 minutes to define the desired serpentine geometry. Once the etch is complete the stretchable serpentine traces is now suspended between the rectangular frames. At this point, the individual structures are carefully removed from the handle wafer by slightly heating and loosening the photoresist on a hot plate at 95° $°C$. The charged white region shown in the scanning electron microscopy (SEM) image is due to the presence of oxide.

Additionally, shown in Figure 4.3, multiple serpentine etch profiles were tested using the methods reported here. Many of the Bosch process anisotropic (ICP DRIE) plasma steps were first tested on a standard 4 in (100) Si wafer, as opposed to on the expensive SOI wafers. These etching profile results show this technique can fabricate serpentine traces as thick as 300 μm
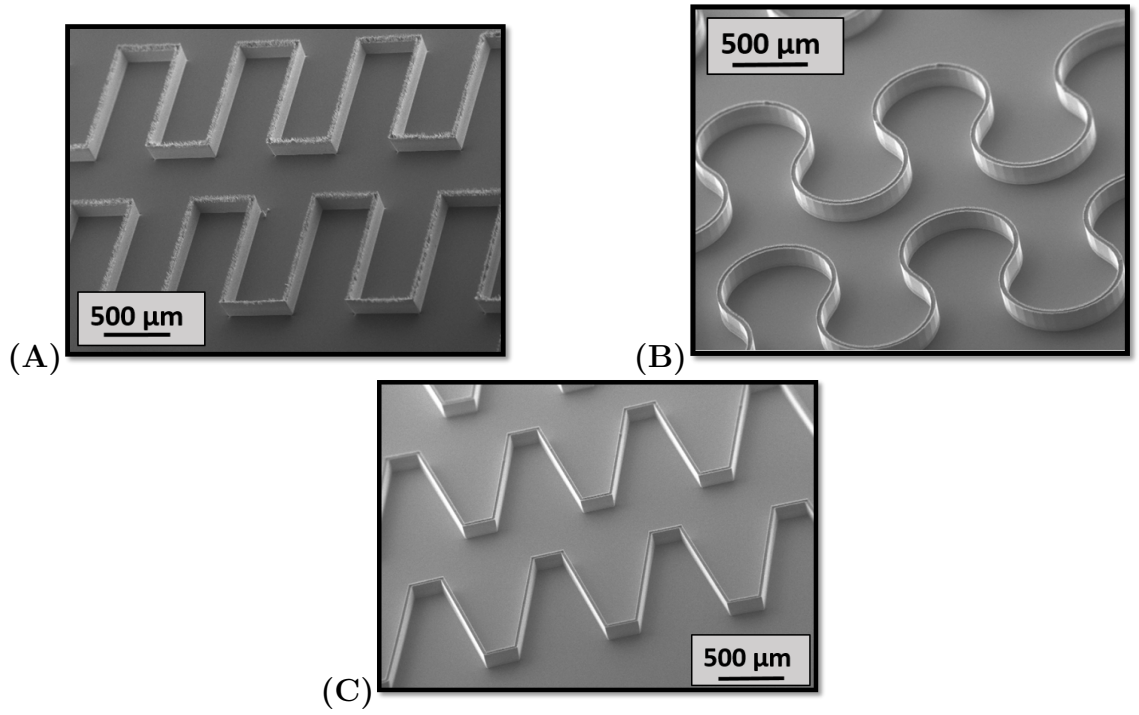
Figure 4.3: **Scanning electron microscopy (SEM) images of the other serpentine geometries tested though DRIE** A.) Rectangle B.) Horseshoe C.) Trapezoid

6. Next, the entire structure is stripped of all oxide hard masking material and residual photoresist using an anhydrous hydrofluoric acid (Primaxx HF Etcher) for 30 minutes. Additionally, I have demonstrated that these serpentines can survive one-sided metal deposition (2 μm NiTi AJA ATC 2200 Co-sputter Deposition) after release, shown in the processing image in step 6. However, all experiments demonstrated will be the bare Si serpentine.

7. Finally, the sample is clean and ready for mounting into the 3D printed sample holder, described in section 5.2.4. The holder is intended to apply external strain to the serpentine during Raman characterization. For mounting, a M31 Epoxy is used to mount the serpentine onto microscope slides, which are secured into the holder. This is the last step before characterization, shown in Figure 4.4.
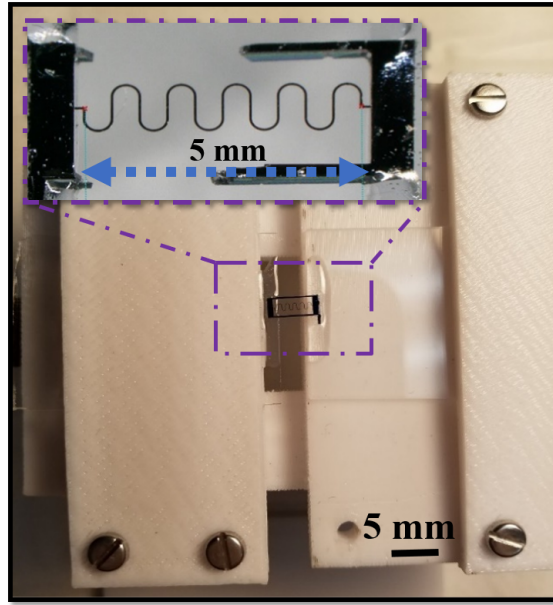
Figure 4.4: **Fabricated Curved Corner Si serpentine released and mounted into the 3D printed sample holder, ready for Raman Spectroscopy characterization.**

4.3 Fabrication Process of Serpentines from (0001) Gallium Nitride

The release process of Si serpentines was easily achieved by using an initial wafer stack that separates the desired Si device layer from the handle through dielectric material (SiO_2) which has a different etch selectivity than Si. This type of heterostructure etch selectivity is similar to the case of GaN on Si when in h selectivity of Si and GaN in Cl_2 plasma gas chemistry. The fabrication process developed in Section 4.2 can be modified, tuned, and adapted allow fabrication of III- V materials such as AlGaN, GaN, and InGaN, epitaxially grown on to a Si substrate. For the anisotropic etch of the III - V material, a Unaxis Versaline ICP III-V etcher can be used. I propose a process flow to allow for the fabrication and release of GaN serpentines. This work is preliminary, so far I have successfully demonstrated steps 1 - 5.
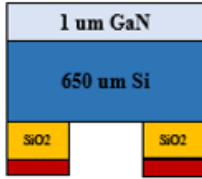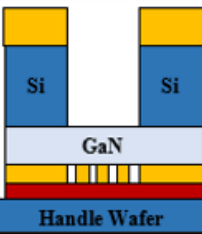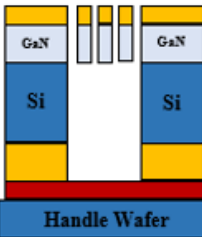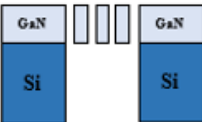
Device Cross Section:	Major Processing Step:	Required Materials/ Tools:
1 um GaN / 650 um Si	1. Starting Stack: 1 cm x 1 cm of 1 µm single crystal GaN on 650 µm Si. Clean (degrease) chip.	- Acetone (5 min) - Methanol (5 min) - IPA (5 min) - DI Water (5 min)
1 um GaN / 650 um Si / 6 um SiO2	2. PECVD 6 µm of SiO_2 onto the back of the silicon substrate.	- Plasma Therm 790 +
1 um GaN / 650 um Si / SiO2 SiO2	3. Photolithography to pattern the oxide. Buffered Oxide Etch 6:1 to pattern the oxide hard mask.	- AZ5214E Photoresist - Karl Suss Mask Aligner (MA6 / BA6) - AZ400 K Developer - Buffered Oxide Etch 6:1 (60 min)
1 um GaN / 650 um Si / SiO2 SiO2	4. PECVD 0.1 µm of SiO_2 onto GaN. Photolithography to pattern serpentine structure and BOE to etch hard mask.	- Plasma Therm 790+ - AZ5214E - Karl Suss Mask Aligner (MA6 / BA6) - AZ400 K - BOE Etch (30 seconds)
Si Si / GaN / Handle Wafer	5. Strip all photoresist. Bond stack GaN side down to handle wafer via photoresist. Deep Reactive Ion Etch (DRIE) through the 650 µm of Si.	- Acetone - Methanol - IPA - 4 in Si handle wafer - 10 µm AZ9245 Photoresist - DRIE: Versaline
GaN GaN / Si Si / Handle Wafer	6. De-bond chip from handle in acetone. Flip over and re-bond Si side to handle wafer. Plasma etch anisotropically to release GaN.	- Acetone - 10 µm AZ9245 - 4 in Silicon handle wafer - ICP DRIE III – V Plasma Etcher:
GaN GaN / Si Si	7. De-bond chip from handle using a hot plate. Vapor HF to remove all oxide.	- Hot plate - Primaxx Vapor HF

Figure 4.5: **Simplified process flow chart showing the major steps required to fabricate and release a GaN serpentine.**

4.4 Fabrication and Release Summary and Conclusions

In this chapter, I presented a detailed fabrication process to allow for the release of free standing 2D Si serpentine traces, not bonded to an elastomeric support. I demonstrated this by fabricating a 5 period Curved Corner serpentine structure with a amplitude height of 1 mm, wave length of 1 mm, radius of 250 μm, width of 50 μm, and thickness of 7 μm, patterned in the <110> and <100> crystallographic directions on a (100) Si wafer. The procedure I report can be repeated by the average user in a standard clean room. The methods reported in this thesis are advantageous to develop free standing single crystal silicon from an SOI wafer which gives us control over the serpentine's geometrical dimensions such as thickness (up to 200 μm), and width (up to 250 μm). Additionally, I proposed a fabrication process that would allow for the release of free-standing GaN serpentine traces. The GaN fabrication method I proposed will eventually be integrated with the current stretchable high electron mobility transistor (HEMT) fabrication process (3) to allow characterization of free standing stretchable AlGaN / GaN HEMT devices. It is desirable to characterize stretchable devices without the presence of a substrate to gain better insight on the crystalline materials performance.

Chapter 5: *In-Situ* Stress Measurements on Stretchable Crystalline Si using micro-Raman Spectroscopy

Raman spectroscopy is a powerful, non-destructive characterization technique that can optically provide structural information such as crystalline quality and the amount of stress/ strain in a crystal (74; 75). In this work, for the first time, I demonstrate micro-Raman Spectroscopy as an *in-situ* stress characterization technique on stretchable crystalline semiconductors, while applying external strain. First, a fabricated free standing (100) Si Curved Corner serpentine mechanical test structures patterned in the <110> crystallographic direction is mounted into a custom built 3D printed sample holder, which allows one to apply global external strain to the serpentine during micro-Raman Spectroscopy characterization. Next, to demonstrate that stretchable Si can survive a minimum applied external strain of 30%, optical microscopy was showed a strain-to-rupture (maximum tensile strain) of 84%. The tensile strain performance is compared to the FEM results reported in Chapter 3. Afterwards, a (100) Si Curved Corner serpentine patterned in the <100> direction was characterized while applying global external strains of 0-72% strain. Micro-Raman spectra were then taken as a function of position across the trace, analyzed and converted to stress measurements on three locations of the <100> Si Curved Corner serpentine (Amplitude, Bend, and Straight, shown in Figure 5.1) to analyze the non-uniform stress distributions. Lastly, I demonstrated micro-Raman spectroscopy can be used to optically monitor the elastic behavior of crystalline serpentines by performing low-cycle stress experiments, globally straining the <100> trace from 0 - 30% for 15 cycles.
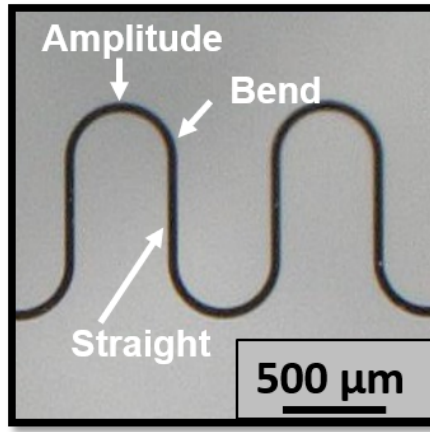
Figure 5.1: **Location of the Amplitude, Bend, and Straight part of a Si Curved Corner serpentine trace.**

5.1 Raman Spectroscopy as a Stress Measurement Technique

Inherent and induced residual stresses are known to affect the yield, functionality and reliability of fabricated microelectromechanical systems (MEMS), which can lead to premature device failure in the form of cracking, curling, buckling, or fatigue (76; 77). Stresses within a material can arise from internal and external factors which can occur during any step within a fabrication process. Internal stresses commonly originate from temperature dependent processes such as deposition of thin-film metals from sputtering or evaporation or deposition of oxides through plasma enhanced chemical vapor deposition (PECVD) (78). Another source of internal stress is epitaxial misalignment between a substrate and an epitaxially grown crystalline semiconductor through techniques such as molecular beam epitaxy (MBE) or metal-organic chemical vapor deposition (MOCVD) (78). External stresses arise from various micro-machining processes such as wet chemical etching, photolithography, inductively coupled plasma deep reactive ion etching (ICP DRIE), ion milling or even simply from device handling. Stress and strain present within a stretchable crystalline serpentine could lead to a degradation or a detrimental effect in the material's electrical and mechanical performance which could cause premature device

failure. Predication of the location, and characterization of the residual and applied mechanical stresses present within traditional and stretchable MEMS devices is essential for prediction of the material's performance and lifetime (79).

While several characterization techniques exist that allow for inherent crystal stress analysis, challenges arise when locally evaluating stress at the micro-scale, or while applying controlled external deformation. Examples of direct internal stress measurements include wafer curvature (57), bending tests, tensile tests and incorporation of strain sensors, however, these techniques often require lengthy user tool training, extensive data analysis, and model correlation for correct interpretation (78). Cross sectional transmission electron microscopy (XTEM) can be used to generate local stress measurements with high precision (nm), however, it requires destructive sample preparation (78), and can only be taken on a stationary sample. X-ray diffraction (XRD) can be used to generate the strain tensor components, which can be resolved into the stress components and intrinsic lattice constants of a crystal; however, laboratory scale XRD has such a low spatial resolution that only the mean value stress is typically obtained over a large area (57). This problem could be circumvented if the XRD is equipped with a micro-diffractometer, or if it is powered by a high energy source such as a synchrotron, however these powerful XRD sources are not easily accessed by the average user. As a result, the aforementioned techniques are insufficient to measure the internal and external stress effects within free-standing crystalline serpentine structures.

As an alternative, micro-Raman Spectroscopy (μRS) has proven to be a powerful characterization method for evaluating residual and applied mechanical stresses within crystalline materials. The effect of residual mechanical stress and externally applied loads on the Raman scattering spectrum has been well studied for single crystal silicon (75; 80). One of the first reports of stress on the Raman modes of Si was by Ganesan et al in 1970 (81), and their results showed there is a linear relationship between applied stress and wave number shift. De Wolf et al. also showed a linear relation between uniaxial and biaxial stress and the peak position for the mode in single crystal Si (74). When the wafer is under intrinsic or extrinsic

stress, the lattice strain causes linear shifts in the wavenumber of the active phonon modes. Since the discovery of this relationship, researchers have adapted Raman spectroscopy to measure stress in Si MEMS devices such as on released micro-bridges (77; 82) and map stress in Si micro-capsules (83).

5.2   General Theory of Raman Spectroscopy

Crystalline materials are comprised of periodically arrayed atoms vibrating at a characteristic frequency. Raman Spectroscopy has the ability to detect variations in the crystals lattice vibrational energy, based on the energetic shifts which arise from in-elastic scattering interactions with the active phonon modes. Typically, when a monochromic radiation source is incident on the surface of a crystal, the light wave (photon) will interact with the lattice vibration (phonon) through a first-order elastic Rayleigh scattering process. However, one out of 10^{12} of these interactions will result in an in-elastic energy exchange through a second order Stokes-Raman scattering process (74). In this case, the coupling between the phonon/ photon c hanges the crystals electrical susceptibility and polarizability, subsequently causing a shift in the lattice vibrational energy through Raman Scattering. Stokes-Raman and Anti-Stokes Raman scattering require that energy and momentum between the phonon/ photon interaction must be conserved: $w = w_i$ - w_s and $q = k_i$ - k_s, where w_i and k_i are the respective frequency and wave vector of the incident photon, and w_s and k_s are the respective frequency and wave vector of the scattered photon (74). The change in vibrational energy states in Rayleigh Scattering and Raman Scattering is explained through a Jablonski energy diagram, depicted in Figure 5.2.

Figure 5.2: **Jablonksi energy diagram of quantum energy transitons between Raman and Rayleigh scattering.** This diagram shows the difference between Rayleigh and Raman scattering when an incident photon excites a phonon from a vibrational state to a virtual state. Adapted from ref (84)

5.2.0.1 micro-Raman Experimental Information

The experimental apparatus required to perform Raman measurements is a monochromic light source, a spectrometer, and a charge coupled detector (CCD). When a Raman instrument is paired with a confocal microscope, the monochromic light source can be focused onto a spot size of $< 1 \ \mu$m, allowing for micro-Raman spectroscopy (μRS). μRS is desired for our experiments because the precision of the measurement allows us to study the local surface stress distribution on the small features of the serpentine. Further, the high mechanical stability of the micro-Raman system allows the recording of phonon properties over large area maps using a piezoelectric xy stage (74).The experimental apparatus used in the following experiments is shown in Figure 5.3.
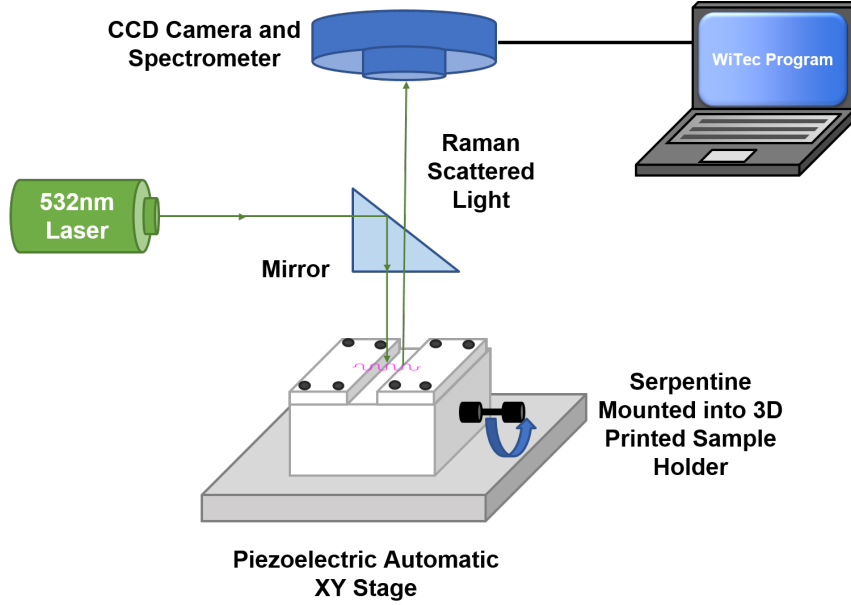
Figure 5.3: **Micro-Raman experimental apparatus** The apparatus consists of a monochromic laser radiation source (Nd:YAC 1064nm frequency doubled to 532nm), reflection mirror, piezoelectric XY stage holding the sample holder and serpentine, detector, CCD camera and spectrograph

The Raman experiments performed in this thesis were with a WITec Alpha300RA confocal Raman Microscope, with 300 nm spatial resolution. Prior to collecting Raman spectra, the laser is stabilized at the desired power for a minimum of 2 hours and then calibrated to the WITec standard procedure. An Nd:YAC 1064 μm frequency doubled excitation laser source (532 nm, 0.5 mW) was focused on Si serpentine samples through a 100X long working distance (LWD) microscope objective lens. Single Raman spectra are collected in the $Z(XX)\bar{Z}$ backscattered geometry of Si (001), with 0.5 second time integrations and 60 accumulations through a 1800 g/mm grating spectrometer, equipped with a charge coupled detector (CCD). The resolution of the measurements are 0.1 Rcm^{-1}. Our instrument is paired with an automatic XY piezoelectric stage, allowing for high resolution Raman mapping capabilities with step sizes of 200 nm, which was utilized in calibration measurements.

5.2.1 Raman To Measure Stress in Silicon

Silicon has three active optical phonon modes, two transverse optical (TO), and one longitudinal optical (LO) modes (74; 75). Based on crystal symmetry in the diamond cubic structure of Si, all of the optical phonon modes are triple degenerate, corresponding to a characteristic wave number of $w_0 = 520 - 521$ Rcm^{-1}. Note here Rcm^{-1} is used which means *relative cm^1* because the wavenumber of the scattered light is relative to the incident light. When Raman units are reported as cm^{-1} this refers to angular frequency. For the backscattering geometry of a (100) Si surface, the LO mode is the primary mode that contributes to the Raman signal. Reported values of the peak position of the LO phonon in unstrained (100) Si is reported to vary from as low as 520 Rcm^1 (74) to as high as 521 Rcm^1 (75). The peak position is sensitive to the the Raman instrument, wavelength of the excitation source, thickness of the sample, doping type, and any defects that could be present, inducing strain within the material. Because of this variability, when performing stress measurements with μRS, it is important to calibrate all measurements to a known unstrained silicon reference sample. The absolute position of the reference value is not necessarily important for these measurements since it can vary from instrument to instrument. What is important is the *change* in this value during Raman measurements, which reveals information about the local surface stress distribution.

Raman spectroscopy can be used to determine the built-in stress within a Si crystal with very high precision. When a Si crystal is under uniaxial or biaxial strain, the triple degeneracy of the optical phonons are lifted, resulting in a peak broadening and linear shift in Raman wavenumber. As a result, many researchers have found a direct linear correlation between a Raman wavenumber shift, and the magnitude of stress/ strain change in the material (74; 75; 82; 85). (100) Si exhibits a single Raman peak at $w_s = w_i - w_0 = 520\text{-}521$ Rcm^{-1}. Here w_s is the frequency of the scattered light, and w_i is the frequency of incident light, and w_0 corresponds to the triple degenerate optical phonon of the center of the Brillouin Zone, which occurs at a frequency of 520-521 Rcm^{-1} (80).

The relationship between frequency shift of the three optical phonons of Si be found through solving the secular equations (74; 81; 86) It has been shown that Raman frequency shifts linearly with stress/ strain; under tensile stress, the peak shifts to lower wavenumbers, while compressive stress shifts the peak to higher wavenumbers. This is related through the following equations for uniaxial stress in silicon (74):

$$
\begin{aligned}
\Delta\omega_1 &= \frac{\lambda_1}{2\omega_0} = \frac{1}{2\omega_0}(pS_{11} + 2qS_{12})\sigma \\
\Delta\omega_2 &= \frac{\lambda_2}{2\omega_0} = \frac{1}{2\omega_0}[pS_{12} + q(S_{11} + S_{12})]\sigma \\
\Delta\omega_3 &= \frac{\lambda_3}{2\omega_0} = \frac{1}{2\omega_0}[pS_{12} + q(S_{11} + S_{12})]\sigma
\end{aligned}
\tag{5.1}
$$

Where λ is the eigen value calculated from the secular equation, p, q, and r are the phonon deformation potential material constants, and S_{ij} are the elastic compliance tensor components. For a (001) backscattered surface, only the third optical mode is observed ($\Delta\omega_3$).

Since the elastic compliance tensor components are an anisotropic material property, the relationship between strain and Raman frequency shift can be evaluated along the <110> and <100> directions on a (100) Si wafer. For the <100> direction, $S_{11} = 7.68 \times 10^{-12}\ Pa^{-1}$, $S_{12} = $ -2.14 x $10^{-12}\ Pa^{-1}$, $S_{44} = 12.6 \times 10^{-12}$ Pa^{-1}, and p = -1.43ω_0^2, q = -1.89ω_0^2, r = -0.59ω_0^2, we find:

$$
\Delta\omega_3^{<100>}(cm^{-1}) = -1.936 * \sigma^{<100>}10^{-9}Pa \tag{5.2}
$$
$$
\sigma^{<100>}(MPa) = -516\Delta\omega(cm^{-1})
$$

Anastassakis et. al (87) reports there is a mean derivation of 25% in literature values for the phonon deformation potential coefficients of Si, and determined the average coefficients values to be $p/\omega_0^2 = $ -1.85 $\pm$ 0.06, $q/\omega_0^2 = $ -2.31 $\pm$ 0.06, r/ω_0^2 = -0.71 $\pm$ 0.02, the *Grüneisen* parameter $\gamma_G = 1.08 \pm 0.06$, and that hydrostatic

stress along the [100] direction for silicon is (1.88 ± 0.05 cm^{-1} / GPa) which is close to the calculated value in Equation 5.2. For the <110> direction on the (100) Si plane, $S_{11} = 5.45$ x 10^{-2} Pa^{-1}, $S_{12} = -0.835$ x 10^{-12} Pa^{-1}, $S_{44} = 12.6$ x 10^{-12} Pa^{-1}, and $p = -1.43\omega_0^2$, $q = -1.89\omega_0^2$, $r = -0.59\omega_0^2$, we find:

$$\Delta\omega_3^{<110>}(cm^{-1}) = -1.962 * \sigma^{<110>}10^{-9} * [Pa] \tag{5.3}$$

$$\sigma^{<110>}(MPa) = -509\Delta\omega(cm^{-1})$$

Biaxial stress is treated similar using the x and y stress tensor components (σ_{xx} and σ_{yy}), with a slightly lower stress dependence than in the uniaxial cases:

$$\Delta\omega_3^{biaxial} = \frac{\lambda_3}{2\omega_0} = \frac{1}{2\omega_0}[pS_{12} + q(S_{11} + S_{12})](\sigma_{xx} + \sigma_{yy})$$

$$\sigma^{biaxial}(MPa) = -435\Delta\omega(cm^{-1}) \tag{5.4}$$

DeWolf ([74]) reports that Si in the [100] direction under 500 MPa of tensile or compressive stress will demonstrate a peak shift of 1 Rcm^{-1}, as shown in the above calculations. Our instrument can detect wave number shifts with a precision of about 0.1 Rcm^{-1}, which corresponds to a stress of 50 MPa, and an intrinsic strain level of 2 x 10^{-4}. The coefficients I calculated describe the effect of anisotropy on the stress and Raman frequency dependence, however, the values are within the experimental resolution of the WITec instrument; therefore, we cannot use Raman to measure the anisotropic stress dependence. The relationship between frequency shift and stress is graphically demonstrated in Figure 5.4. For a very detailed, mathematical explanation of Raman Spectroscopy, and its applications to measure stress on silicon integrated circuits, please see De Wolf ([74]), Anastakkakis et al. ([85]; [87]), and Srikar et al. ([78]).

5.2.1.1 Raman Calibration used for Si Stress Measurements

As previously mentioned, it is very important to calibrate the system to a known "unstrained" reference sample, because micro-Raman spectroscopy mea-

sures relative *changes* in the wavenumber and thus the strain. After calibrating the WITEc Raman system using the manufacturer's standard procedure, an unstrained (100) Si sample provided by WITec is measured to serve as the reference sample in the following studies. The typical Raman spectra of Si is shown in Figure 5.4A (left), with the laser line at 0 Rcm^{-1}, the primary LO Si peak used for stress measurements at $w_0 = 521.7$ Rcm^{-1}, and a secondary Si peak 950 Rcm^{-1}. Figure 5.4B (right) the Raman shift in wavenumber of the primary shows three measured spectrum's of (100) Si with varying amounts of stress. The black curve serves as the unstrained bulk (100) Si reference, the red curve is shifted due to tensile stress, and the blue curve is shifted due to compressive stress.
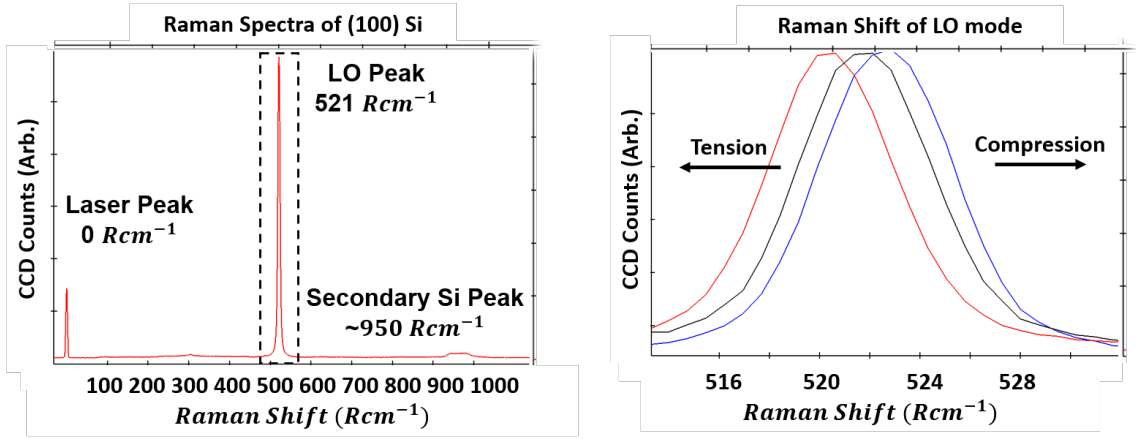
Figure 5.4: **Raman Spectra and stress relation in unstrained bulk (100) Si.** Figure A.) demonstrates the measured standard Raman Spectra of Si (provided by WITec), used as the calibration reference standard for the following experiments. Figure B.) demonstrates the relationship between wavenumber shift and tensile/ compressive stress. The red curved shifted to lower wavenumbers is Si in tensile stress while the blue curved shifted to a higher wavenumber is compression stress.

The standard (100) bulk Si sample provided by WITec results in an $w_0 = 521.7$ Rcm^{-1}, slightly higher than the range reported in literature ($w_0 = 520$ - 521 Rcm^{-1}). To provide a more accurate initial reference value for the Si serpentines that I fabricated in Chapter 4, I also generated a reference value on the silicon-on-insulator (SOI) wafer serpentines were processed on. Since the initial SOI wafer chip is unprocessed, I could use the piezoelectric XY stage to generate a 10 μm x 10 μm

map of the wavenumber of the LO phonon in Si. As shown in Figure 5.5, the initial unstrained position varies between 521.8 - 522.1 Rcm^{-1}. The average wavenumber value corresponds to 521.95 Rcm^{-1}.
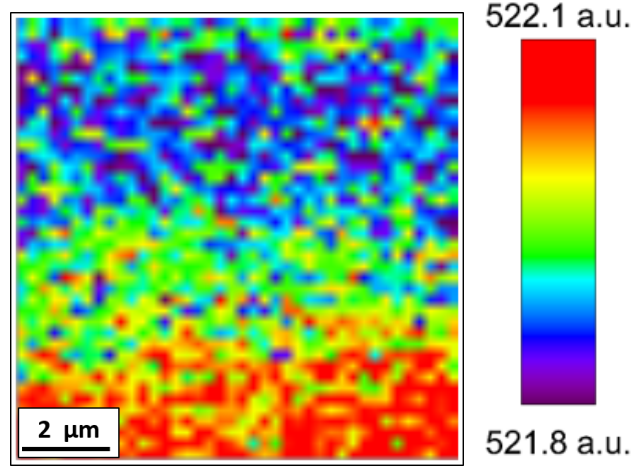
Figure 5.5: **Micro-Raman wavenumber position map of reference SOI wafer.** The wavenumber map shows the average position in a 10 μm x 10 μm region results in a variation between 521.8 - 522.1 Rcm^{-1}. The average wavenumber value in this sample corresponds to 521.95 Rcm^{-1}.

If we use the wavenumber value from the bulk (100) Si WITec sample as w_0 = 521.7 Rcm^{-1} and the wavenumber value from the unprocessed SOI wafer as w_s = 521.95 Rcm^{-1}, we find $\Delta\omega_3$ = 521.95 - 521.7 = 0.25 Rcm^{-1}. We can then calculate the amount of intrinsic stress in the SOI wafer using Equation 5.2, where we find $\sigma^{<110>}$ (MPa) = -509 * 0.25 = -127.25 MPa of stress. This means initially the SOI wafer is under -127.25 MPa of compressive stress. SOI wafers are known to have a built-in compressive stress, compared to bulk Si due to mismatch in the coefficient of thermal expansion between Si (2.6 X 10^{-6}/K) and SiO_2 (0.5 X 10^{-6}/K), and the relationship between stress and strain in SOI films is well studied using Raman spectroscopy in ref (88). It is also reported compressive strain in Si results in a decrease of the Hall mobility while tensile strain increases the Hall mobility, which shows there is a strong dependence between the electrical and mechanical properties of Si devices.

5.3 Experimental Modification to Allow Application of External Strain during μRS Measurements

To be suited for stretchable and wearable electronic applications, the stretchable Si serpentine traces must elastically survive global elastic deformation by a minimum of 30% strain to meet the performance of human skin (8). The advantage of using the serpentine geometries is the structure mitigates stress under strain, so while the serpentine is under 10s of percent global strain, locally the strain is far below the $<< 1\%$ intrinsic tensile strain limit of Si. To allow applied deformation to the serpentine, I designed and built a custom 3D printed sample holder that allowed application of externally applied strain in increments of 4-12%. Next, to demonstrate that serpentines I fabricated meet the wearable electronics minimum requirement, I mounted a <110> Si Curved Corner serpentine into the sample holder. I then performed tensile tests using optical microscopy demonstrating the serpentine survived global strains of up to -24% compression and 84% tension.

5.3.1 3D Printed Sample Holder Design

The overall goal of this work is to perform in-situ local stress measurement with Raman spectroscopy on released Si serpentines while applying external strain. The WiTec Raman System is equipped with a piezoelectric XY mapping stage, however, it is not equipped to apply deformation to a sample during measurements. To overcome this limitation, I used the program Solidworks to design a custom mechanical testing fixture (shown in Figure 5.6) which I then 3D printed using a 3D printer (Stratasys FDM Titan 3D printer with polycarbonate material). This sample holder was designed to mimic the conditions modeled in the finite element analysis which suspends and strains the serpentine while securely screwed in to the Raman microscope. Either end of the serpentine is first glued to two separate microscope slides, which are mounted onto both sides of the holder. One end of the serpentine is held fixed in the holder, while the other end is able displace by X

69

amount, parallel to the trace. The main components of the holder are the solid base plate, movable part, and tops to secure the microscope slides. The final assembled holder mounted into the Raman microscope is shown in Figure 5.7.
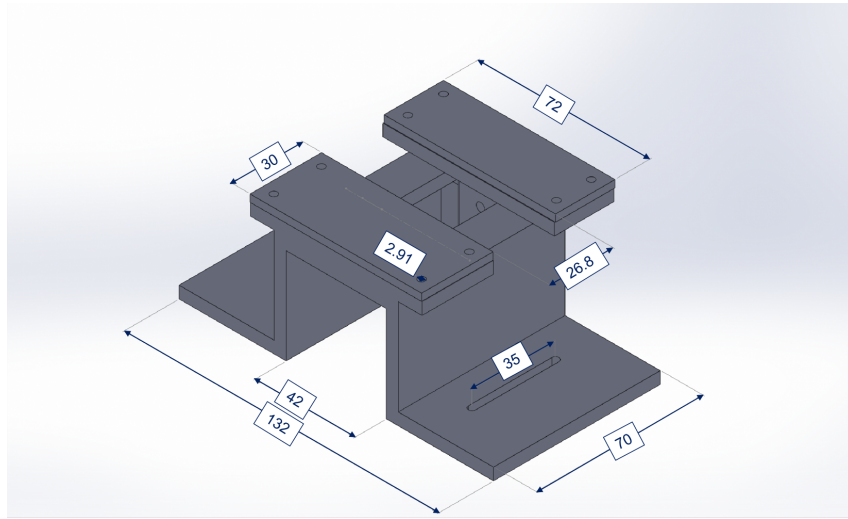
Figure 5.6: **Solidworks engineering drawing of the designed assembled sample holder.** All dimensions are in mm.

After the sample was fixed into the 3D printed sample holder described in section 5.3.1, it is mounted onto the XY stage and is ready for μRS characterization. Turning the black micrometer allows the sample to strain while in the Raman microscope in 4 - 12% strain increments. The reason for the large range in values is due to the imperfections within the 3D printed part which only allowed movement in 40 - 120 μm increments. The range could be reduced if a machine shop polished metal holder was instead designed.
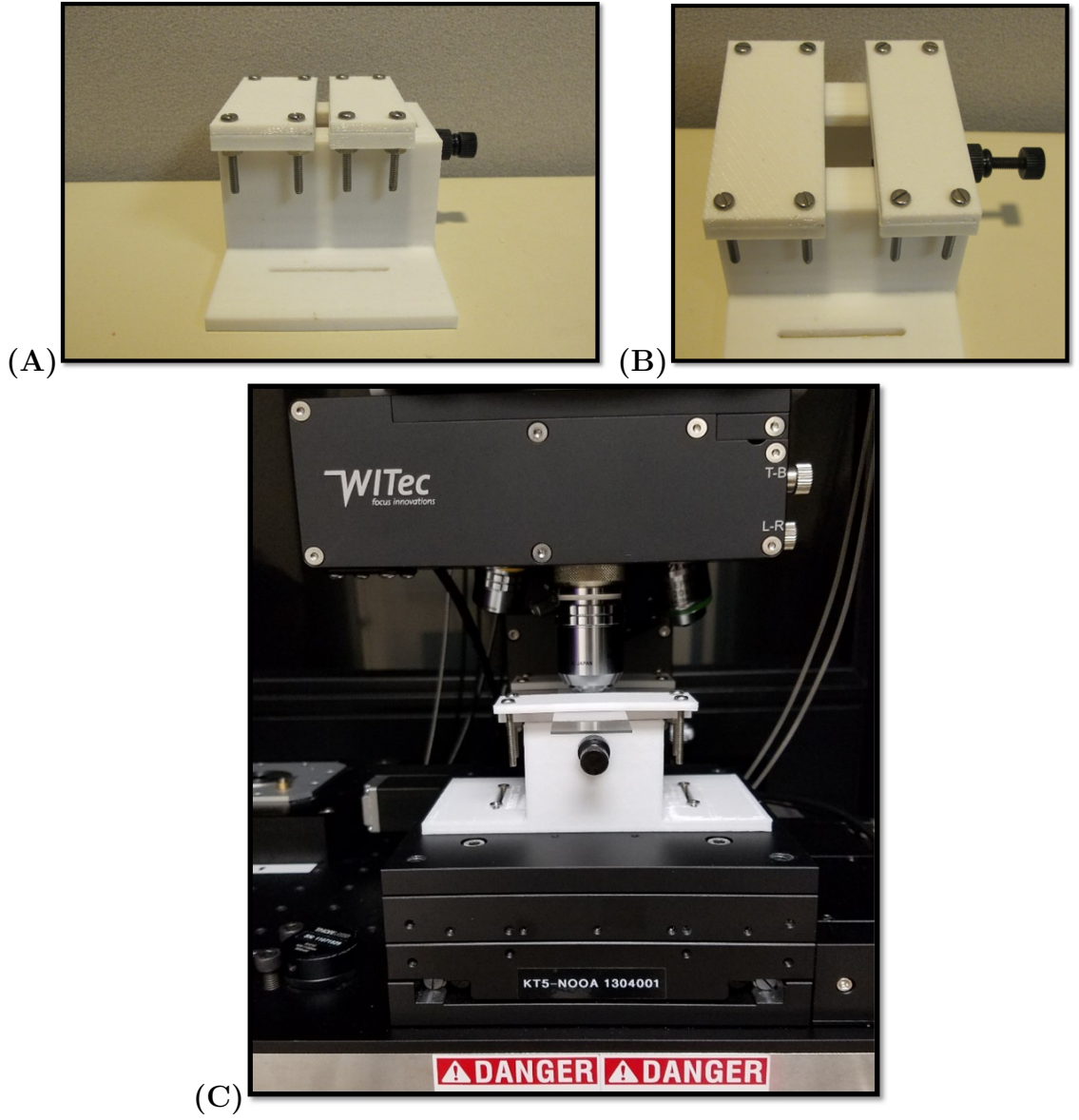
Figure 5.7: **Custom built sample holder for the Raman Microscope.** A.) The assembled holder closed B.) The holder open C.) Sample holder mounted in the Raman microscope

5.3.2 Optical Straining Images of Stretchable <110> Si

Optical microscopy was used to monitor the end-to-end displacement (global strain) of a <110> Si Curved Corner serpentine, as well as the local displacement within the individual period of the serpentine. A Keyence VHX 6000 Microscope with a 200X objective lens, was used to optically measure the individual period and the global end-to-end displacement of the entire serpentine trace, as a function of

strain. The global strain %s refer to the end-to-end displacement, while the local strain %s refer to the individual period strain, reported using the Keyance microscope. The values were later verified by using the computer program ImageJ. As shown in Figure 5.8 the serpentine survived global compressive strains between 0% of -24%. Shown in Figure 5.9, the serpentine reached a maximum global tensile strain of 84% before fracture. This end-to-end displacement was in excellent agreement with the 2D COMSOL model, which predicted a global tensile strain of 84% for this geometry in the <110> direction.
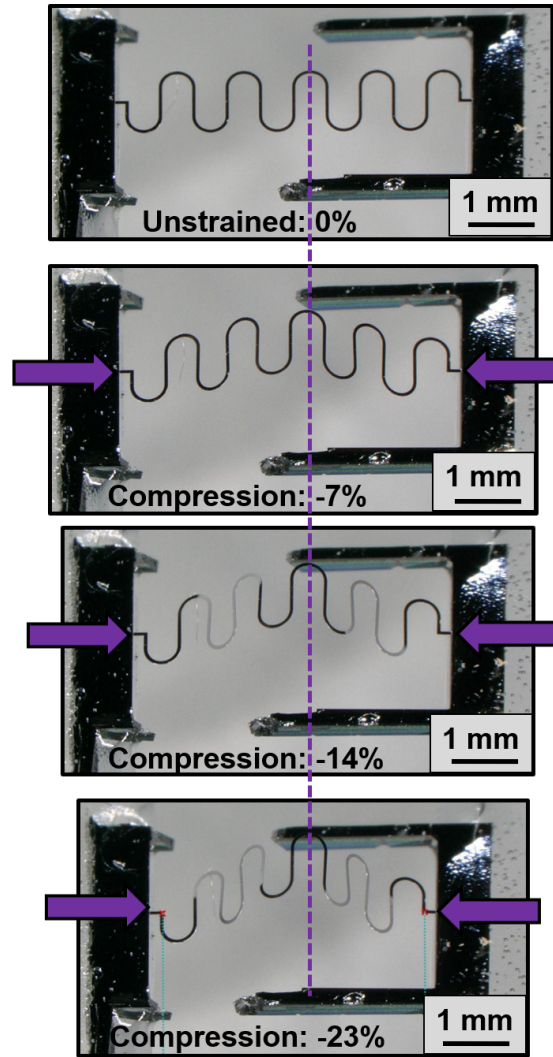
Figure 5.8: **Optical images of compressive strain testing of a <110> Curved Corner Si serpentine surviving a global strain of -24% compression.** Note -24% was not the maximum compressive strain value of strain on this sample.
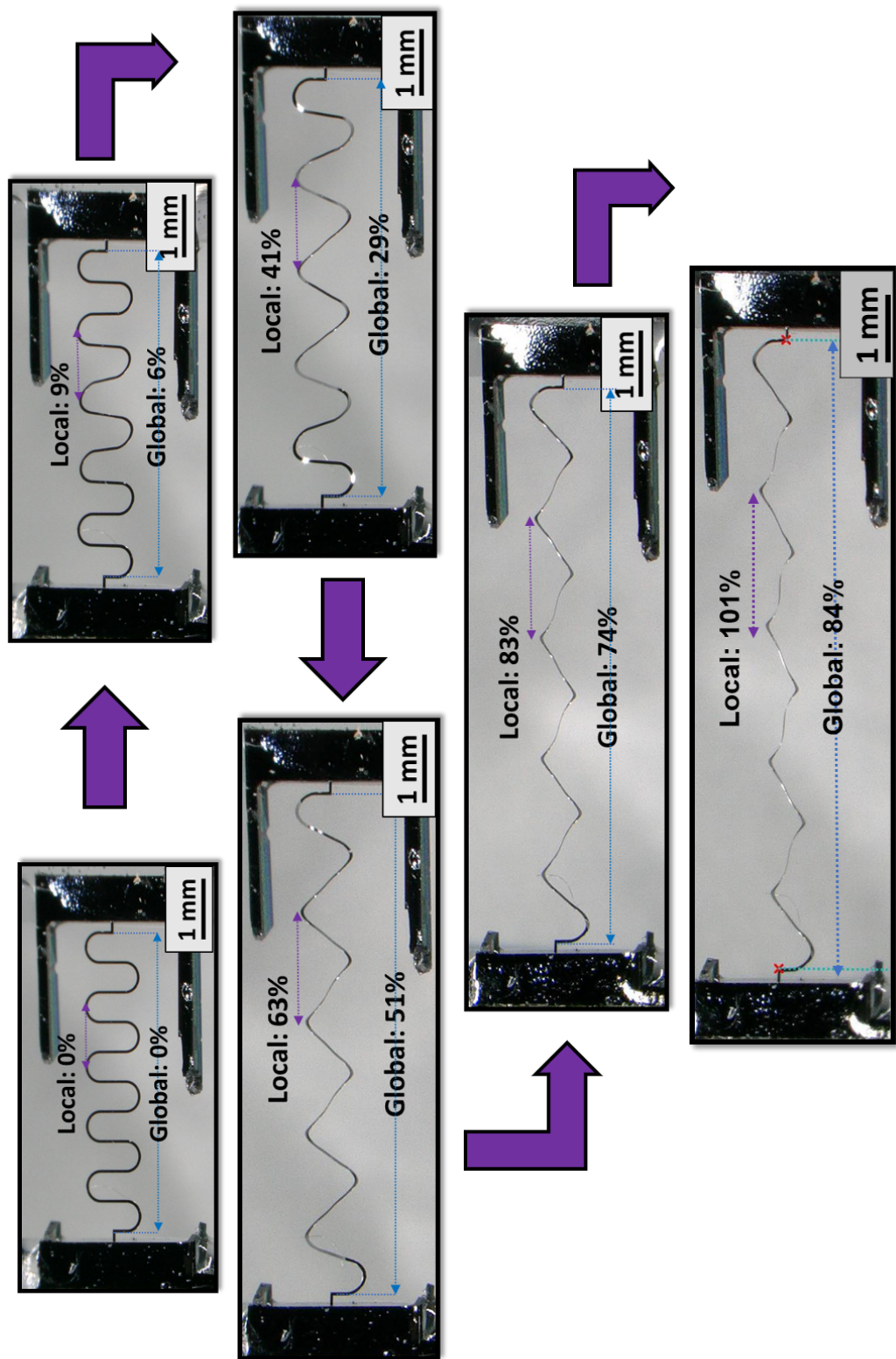
Figure 5.9: **Optical images tensile straining a <110> Curved Corner Si serpentine to a global maximum of 84%, and a local maximum of 101%.**

5.4 Optical Tensile Testing and FEM Result Comparison

The 3D finite element model (FEM) described in Figure 3.14 predicted the maximum stress in a <110> Si Curved Corner serpentine occurs at the Amplitude and at a maximum applied global tensile strain of 70%. The 2D FEM model also predicted the maximum stress to concentrate at the Amplitude, however, it predicted a larger maximum tensile strain at 84%. The experimental tensile testing results on the <110> Si Curved Corner serpentine are in good agreement with the modeling trends, showing a maximum applied global tensile strain of 84%, with breakage at the Amplitude. Figure 5.10 shows the Experiment and Model of the serpentine held at 84% and a cross section demonstrating similar out-of-plane bending motions.
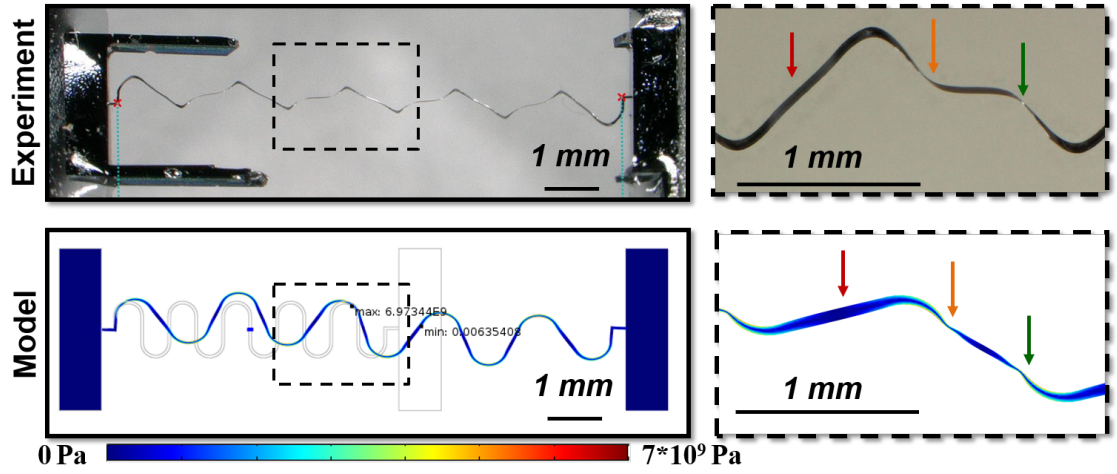
Figure 5.10: **Experiment and model strain comparison of the <110> Si Curved Corner serpentine stretching to 84%.** The model and experiment show similar straining distributions.

The 2D FEM model predicted in Chapter 3 and the experiment give similar strain-to-rupture values of 84% for <110> Si Curved Corner serpentine. However, the 3D FEM model more accurately predicted the out-of-plane buckling which results in a non-uniform stress distribution throughout the trace. The both models also correctly predicted the maximum stress to be concentrated on the Amplitude,

while the minimum stress is concentrated on the Straight part of the trace for a <110> serpentine. Micro-Raman spectroscopy will be used in the next section to gain insight on the local surface stress distribution of the serpentine while applying external strain on a Si Curved Corner serpentine now patterned in the <100> direction. For reference, the 3D COMSOL model predicts the maximum stress on a <100> trace to concentrate on the Bend, with a maximum applied tensile strain of 84%.

5.5 Stress Measurements on Released <100> Si Curved Corner Serpentines: Results and Analysis

In this section I describe the experimental methodology used to generate stress measurements along the three locations of a <100> Curved Corner Si serpentine. I then explain the experimental results and trends observed after converting Raman wavenumber position to stress values to analyze the non-uniform stress distribution on Amplitude, Bend, and Straight locations on the serpentine, as I apply external strains from 0 - 72%.

5.5.1 Stress Measurement Collection Techniques Using Raman

Individual Raman spectra's were collected on three major locations of the fabricated and released <100> Si Curved Corner Si serpentine: Amplitude, Bend, and Straight. As shown in Figure 5.9 the serpentine bends out-of-plane to relieve stress under strain, which was not originally predicted by the 2D COMSOL model, however it was predicted by the 3D model. While the WITec system has Raman mapping capabilities, the out-of-plane bending of the serpentine lead to poor microscope focus, thus a map could not be generated. For this reason, individual Raman spectra's were instead collected at each strain increment as a function of position across the trace, allowing me to monitor the non-uniform stress distribution changes within various locations of the serpentine as external strains were imposed.

To study the non-uniform stress distribution across the 50-55 μm wide trace,

5 single Raman spectra points were taken at every applied strain increment. The reason for the variation of trace width is most likely due to imperfect photolithography and plasma etching steps during the processing. The top and bottom of the period, is the region I refer to as Amplitude, position (A) in Figure 5.11. The origin (0 μm, 0 μm) was located precisely at the top centered edge of amplitude on the 3rd (middle) period in the 5 period serpentine trace, and served as the reference position for the measurements. The origin was redefined back to (0 μm, 0 μm) for each global strain increment. The Bend is labeled position (B) in Figure 5.11, at a location approximately (50,-120) μm away from the Amplitude. The Straight position is labeled (C) in Figure 5.11, and has a location of approximately (500 μm, -500 μm).

In Figure 5.11, 0 μm was defined at the origin (0 μm, 0μm) on the third period's Amplitude, where compression is expected to be found in the trace. As we move down (y-axis) in 10 15 μm step sizes, we can monitor the local stress change from compression to tension. The difference in the Z-height focus between 0 μm and 50 μm was never more than 20 μm on the amplitude. Similar to the methods used for the Amplitude, single spectra's across the trace on the Bend and Straight locations of the beam were also generated with 10-15 μm spacing.
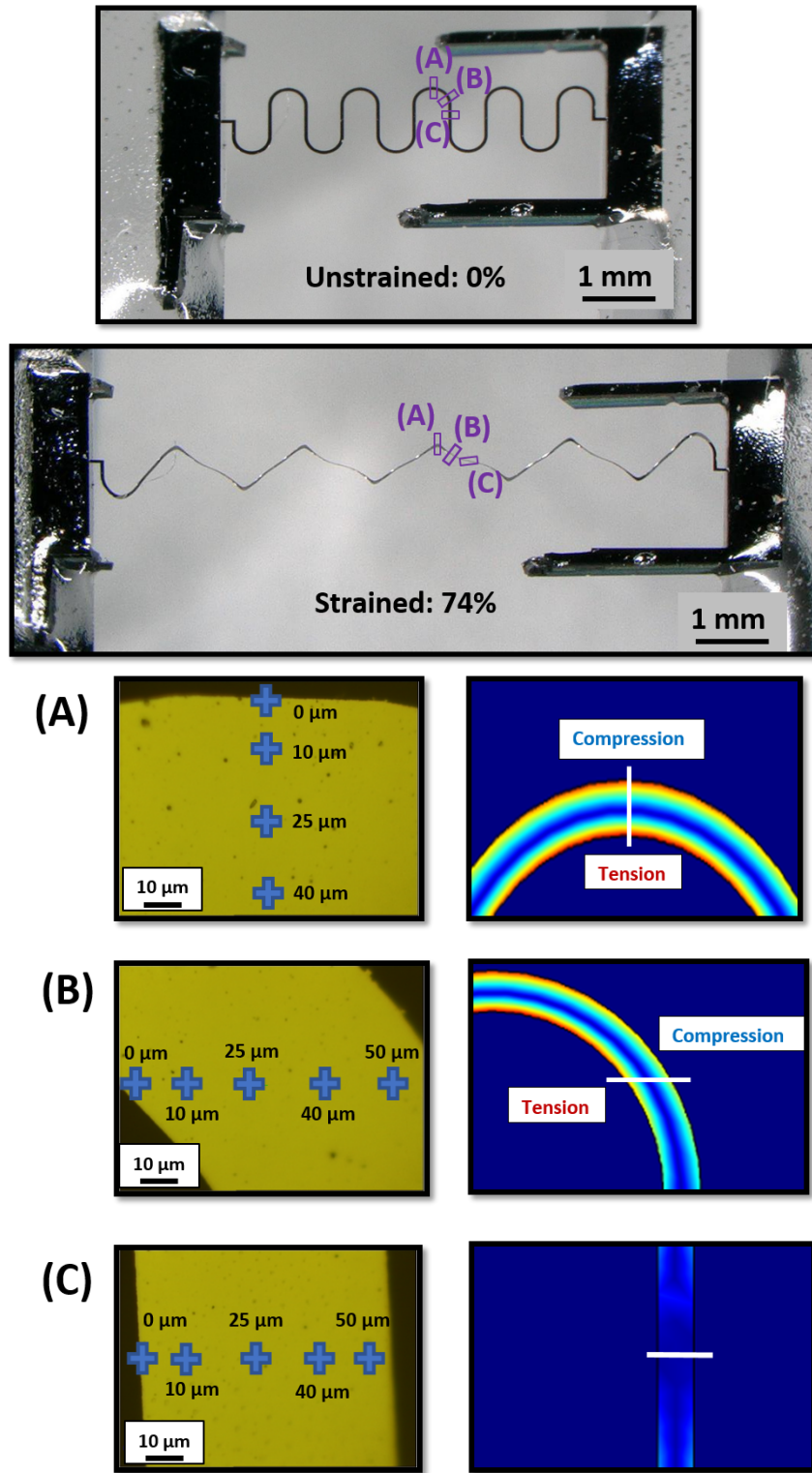
Figure 5.11: **Images demonstrating the locations on the serpentine measured with Raman.** Stress measurements were collected on the A.) Amplitude B.) Bend and C.) Straight parts as a function of position across the trace. The COMSOL images of these locations are also included for reference.

5.5.2 Raman Stress Characterization on Stretchable Si Curved Corner Serpentines

Single Raman spectra were taken as a function of position across the trace on the Amplitude, Bend, and Straight part of a <100> Curved Corner Si serpentine. A minimum of 4 points were generated at each position as I applied global external strains between of 0% and 72%. Optical microscopy demonstrated in the previous section a strain-to-rupture (tensile strain) of 84% for a <110> Curved Corner Si serpentine; therefore, a maximum strain of 72% was selected to prevent inducing plastic deformation. The selection of a lower strain value will allow low-cycle stress fatigue evaluation of the serpentines elastic behavior in Section 5.6. The non-uniform stress distribution, and out-of-plane buckling across the Amplitude, Bend, and Straight part of the trace after a 30% applied global strain are shown in Figure 5.12.
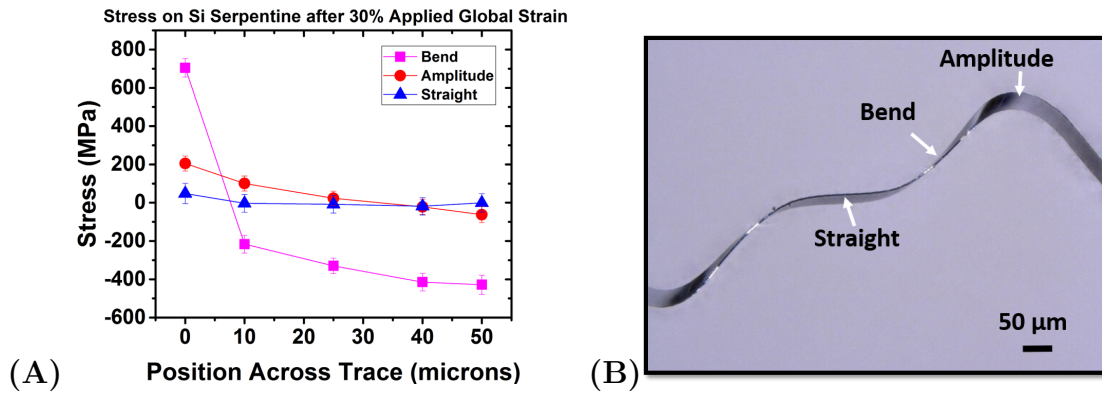
Figure 5.12: **A.) Raman measured stress distribution for all positions after applying a 30% global strain parallel to the trace. B.) Cross section of curved corner serpentine buckling out-of-plane at the Bend and Amplitude under applied strain.**

As shown in Figure 5.12, the maximum stress was concentrated at the Bend, followed by the Amplitude, and then the Straight. Figures 5.13 A,C, and E shows how the non-stress distribution changes while applying external strain from 0 - 72% at each position (A) Amplitude, (C) Bend, and (E) Straight. Figures B, D, and F show the color coordinated Raman position and intensity plot of the Amplitude, Bend, and Straight location at its respective applied strain value.
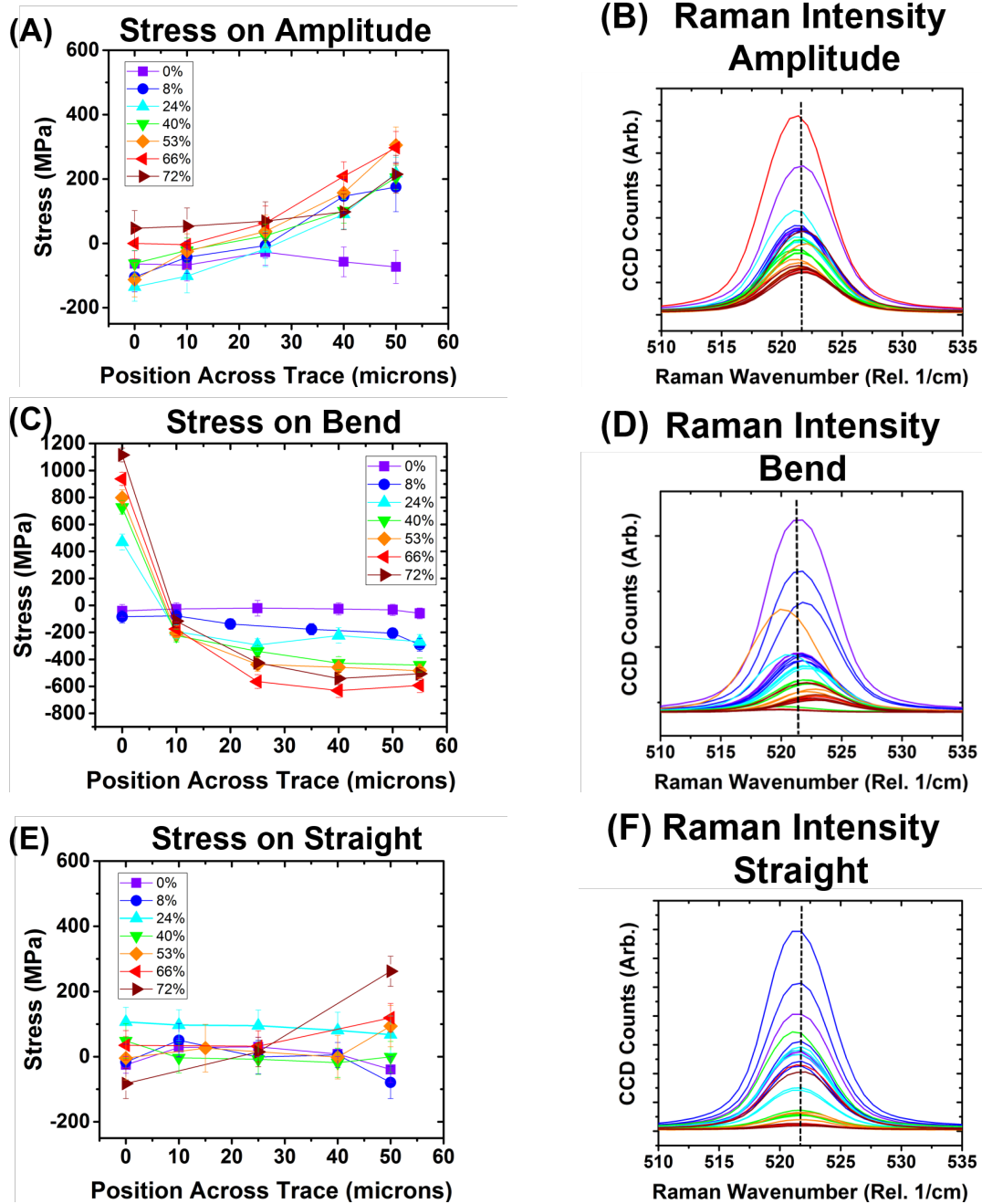
Figure 5.13: **Raman measured stress distribution across the Amplitude, Bend, and Straight part of the serpentine trace as a function of applied strain.** The measured stress distribution and variation in Raman peak position and intensity shown for both locations. Figures A-B show the distribution and Raman intensity plot for the Amplitude, C-D show the Bend, and E-F show the Straight part of the serpentine.

These results indicate that the maximum tensile and compressive stress is

located in the Bend at each applied stain increments, while the minimum stress is located on the Straight part of the serpentine. The maximum stress at the Bend predicted by the 3D FEM for a <100> Curved Corner Si serpentine, due to the out-of-plane buckling induced on the Bend under applied deformation. The Straight part of the serpentine undergoes little buckling deformation, results in minimal stress changes with applied strain. Additionally, all Raman intensity plots demonstrate a decrease in intensity with applied external strain. This is most likely due to the out-of-plane bending and twisting causing a loss in focus on the microscope, and thus a loss in CCD counts on the spectrometer.

5.6 Low-Cycle Fatigue Evaluation on Stretchable <100> Si using Raman Spectroscopy
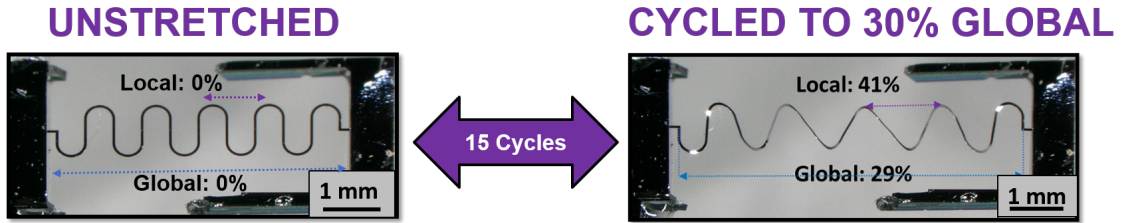
Figure 5.14: **Low-cycle fatigue testing of a <100> Curved Corner serpentine from 0% to 30% applied global strain for 15 cycles.** Raman spectra was collected on each location after applying 0, 5, 10, and 15 cycles. Note that the period is not straining uniformly, meaning a 30% global strain (end-to-end displacement) corresponds to a local strain of 40% in the 3rd period.

In order to study the reversible (elastic) mechanical performance of the serpentines, low cycle fatigue tests were performed to examine the strains required to promote of crack propagation. After the final stress measurement was taken at 72%, the serpentine was reset back to its 0% strain position. The trace was then cycled 15 times between 0 - 30% (end-to-end), which corresponded to a local strain within the individual period of 40%, shown in Figure 5.14. After the 5th, 10th, and 15th cycle, the Raman experimental protocol from above was repeated to collect 5 individual spectra on the Amplitude, Bend, and Straight, shown in Figure 5.15.
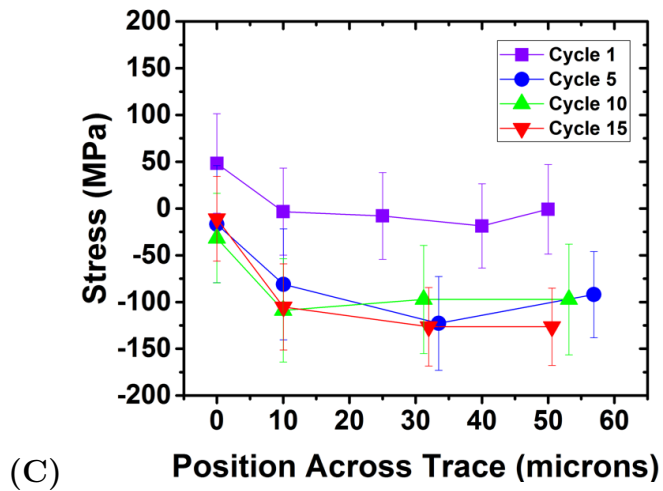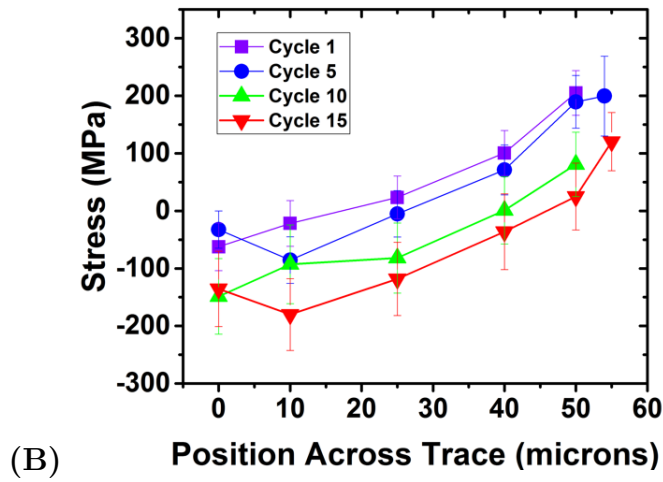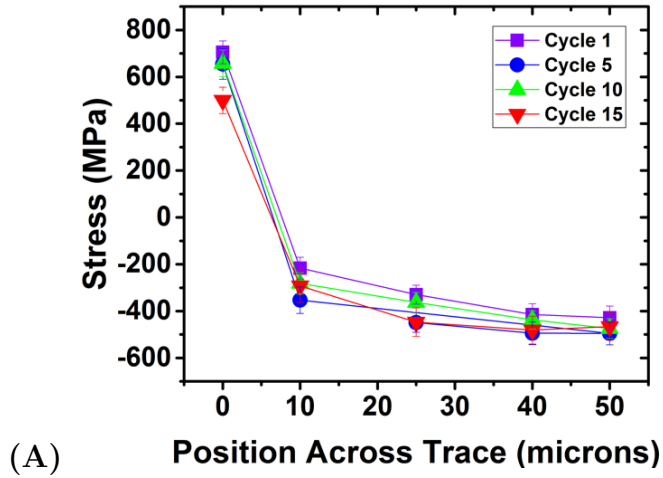
Figure 5.15: **Low-cycle stress and fatigue evaluation on the Amplitude, Bend, and Straight of the <100> Si Curved Corner serpentine after applying a global strain of 30% for 0-15 cycles.** Figure A.) Shows the maximum stress on the Bend, B.) Shows the stress distribution across the Amplitude, and C.) Shows the minimum stress on the Straight part.

These measurements fall within the uncertainty of the instrument (+/- 50 MPa) which indicates there is very little to no plastic deformation in this devices after undergoing a low number of cycles. Since the measurements recorded here follow a systematic baseline shift and the error bars of the measurements fall within the uncertainty of each other, there is no appreciable change in the magnitude of stress that would indicate fatigue in this serpentine trace after 15 cycles. During continuous cycling, it is expected that residual stress gradually accumulates which can lead to micro-cracking, which is problematic for wearable devices intended to have long-term applications. For this reason, I would recommend high cycle fatigue testing (< 1000 cycles) experiments, which I expect to complete on these serpentine traces in the future.

5.7 Raman Spectroscopy to Measure Stress in Stretchable Si Summary and Conclusions

The methods presented in this chapter show micro-Raman spectroscopy is a powerful tool for measuring mechanical performance (stress and strain) in stretchable crystalline semiconductors. Through optical microscopy, I demonstrate a non-uniform straining profile that resulted in a maximum end-to-end displacement of 84% on a <110> Curved Corner Si serpentine, which is in very good agreement with the prior solved FEM models. I then shown I can measure the non-uniform stress distribution across the Amplitude, Bend, and Straight part of a <100> Curved Corner Si serpentine, while applying external global strains of 0 - 72%. The maximum stress was shown to concentrate in the Bend of this trace due to out-of-plane buckling, while the minimum stress concentrated in the Straight part of the trace, also predicted by the prior FEM model. Additionally, I demonstrate low-cycle fatigue stress/ strain monitoring, using micro-Raman spectroscopy, by cycling an applied 0 - 30% end-to-end displacement 15 times, and then taking a set of Raman measurements at each position every 5 cycles. The results demonstrate a baseline shift in the stress measurements, within the experimental resolution of the instrument,

indicating this cycling resulted in elastic behavior. Overall, the results presented in this chapter demonstrate micro-Raman spectroscopy is viable tool in-situ stress characterization technique for stretchable crystalline materials while on the wafer, free standing, and while applying external strain.

Chapter 6: *Ex Situ* Stress Measurements of Stretchable AlGaN/ GaN HEMT Devices

Aluminum gallium nitride / gallium nitride high electron mobility transistors (AlGaN/ GaN HEMTs) are high performance devices which could enable high power and ultrafast switching wearable devices, if made stretchable. With most crystalline materials, the challenge with GaN and AlGaN is the high strength and low tensile strain makes the material inherently brittle to any applied deformation. While device fabrication into serpentine structures can relieve stress under applied strain, there are additional strain considerations inherent to the crystal such as strain present at the interface between the AlGaN/ GaN heterostructure, and the interphase of GaN/ substrate due to lattice constant mismatch. Additionally, deposition of other materials such as metal contacts and passivation layers induces local strain fields within the surface of the device. The presences of non-uniform stress throughout the hetero-structure stack presents additional challenges during the fabrication, release, and encapsulation of stretchable AlGaN/ GaN HEMT devices. In this chapter, I describe methodology and applications of Raman Spectroscopy as a stress monitoring technique of multiple processing steps in the fabrication of stretchable AlGaN/ GaN HEMTs through two separate fabrication approaches: bottom-up and top-down. This includes evaluation of the inherent stress present due to epitaxial mismatch from the as-grown heterostructure, stress within the device fabricated into the serpentine geometry on the wafer, and finally stress within the AlGaN/ GaN HEMT once released from the wafer.
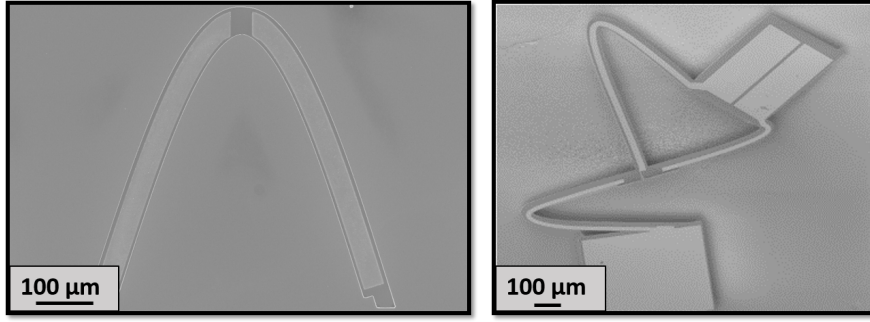
Figure 6.1: **Scanning electron microscopy (SEM) images of a stretchable AlGaN/ GaN HEMT devices grown through the bottom-up and top-down approaches.** (A.) Stretchable HEMT fabricated using the bottom-up approach by Ms. Isra Mahaboob, SEM taken by Ms. Kasey Hogan. (B.) Stretchable HEMT fabricated using the top-down approach by Dr. Randy Tompkins, SEM taken by Dr. Milena Graziano.

In this study, I use Raman Spectroscopy as a stress monitoring technique to evaluate the built-in and induced crystal stress during the fabrication and production of stretchable AlGaN/GaN HEMTs through both the bottom-up and top-down approach. The bottom-up approach refers to using selective area growth (SAG) methods through metal organic chemical vapor deposition (MOCVD) to grow single crystal AlGaN / GaN directly into serpentine structures onto a sapphire substrate. The top-down approach refers to using standard photolithography and micromachining techniques to etch AlGaN / GaN in to the serpentine geometries and then release the structure from its Si wafer. The scanning electron microscopy (SEM) images of the top-down and bottom-up stretchable AlGaN/ GaN HEMT devices that will be characterized are shown in Figure 6.1. The goal of this study is to evaluate how the various fabrication approaches and steps effect the amount of induced stress in the AlGaN / GaN crystal.

First micro-Raman spectroscopy is used to evaluate the stress on the as grown materials to serve as the references, 3.5 μm unintentionally doped GaN on bulk sapphire substrate (bottom-up study reference) and 1.5 μm AlGaN/ GaN stress on bulk silicon substrate (top-down study reference). I then measure a traditional planar HEMT (AlGaN/ GaN on bulk sapphire substrate) as a reference sample to generate a baseline measurement for standard stress in a HEMT device. Next, I map the sur-

face stress on bottom-up stretchable AlGaN/ GaN HEMT devices (on a sapphire substrate) grown on the wafer using two two different masking materials: silicon dioxide (SiO_2) and tungsten (W). Afterwards, I map the surface stress on a top-down stretchable AlGaN/ GaN HEMT (on a silicon substrate) while on the wafer. I then finally map the surface stresses of the top-down stretchable HEMT released (removed) from the Si wafer, and encapsulated within an soft silicone elastomer. Overall, this is the first ex-situ mapping of the surface stresses within stretchable AlGaN/ GaN HEMT devices, using micro-Raman spectroscopy.

6.1   AlGaN/ GaN HEMT Overview

6.1.1   Stretchable AlGaN/ GaN HEMT Motivation

A high electron mobility transistor (HEMT) is a type of hetero-structure field effect transistor, which can operate at frequencies as high as 230 GHz with a power of 250 W (89). The wide band gap semiconductor GaN is commonly used in HEMT devices because it forms solid solutions with its III-Nitride counterparts (AlGaN, In-GaN, AlInGaN), which demonstrates interesting electrical properties, such as high electron mobility, and a high break down field, when joined together into a hetero junction. Extensive research has been conducted to understand the electrical and mechanical material properties for traditional HEMT devices, demonstrating a direct correlation between charge (free electron carriers) and the amount of stress within the material, due to spontaneous and piezoelectric polarization (89; 90). The Army Research Lab has partnered with the College of Nanoscale Science at SUNY Polytechnic Institute to develop the first stretchable AlGaN/ GaN HEMT device for wearable power management. Currently the relationship between HEMT device performance, failure mechanisms, and initial material quality is limitedly understood (89). My research contribution to this collaboration is the first *ex-situ* mapping of the surface stresses within stretchable AlGaN/GaN HEMT devices with micro-Raman spectroscopy on devices fabricated through the bottom-up and top-down approaches. These results will eventually reveal how processing effects stretchable

crystalline GaN device electrical and mechanical performance.

6.1.2 AlGaN / GaN HEMT Hetero-Structure

A heterojunction is formed when an AlGaN layer is epitaxially grown onto GaN, forcing the Fermi energies of two the material to reach an equilibrium which induces a net positive polarization within the AlGaN at the AlGaN / GaN interface and a negative polarization within the GaN at this interface (10; 51; 91). There is a negative polarization that forms at the top of the AlGaN layer and the bottom of the GaN layer. Due to this net polarization, there is an intrinsic electric field present within the GaN and AlGaN materials themselves (E^{GaN} and E^{AlGaN}), and additionally the net polarization due to the AlGaN/ GaN hetero-structure results in the formation of a built in electric field at the interphase between the materials $E_{Interface}^{AlGaN/GaN}$). At this interface, free electrons generated from the surface donor states in AlGaN and electrons from the GaN will accumulate at an energy above the fermi energy, resulting in an extremely conductive region known as the two-dimensional electron gas (2DEG) (10; 51; 92).

The electrons from the surface donor states are thought to come from oxygen impurities and nitrogen vacancies (10; 51; 91; 92). Additionally, since AlGaN and GaN are piezoelectric materials, under an applied electric field or external tensile strain, they will spontaneously generate free carriers ($P_{spontaneous}^{GaN}$ and ($P_{spontaneous}^{AlN}$) which will also accumulate and contribute to the conduction in the 2DEG. The 2DEG formation is attributed to the piezoelectric response of GaN and AlGaN, composition, polarization and strain which generate the various electric field lines (72).The 2DEG is responsible for the fast switching performance, which is why they are highly researched for high power and high frequency devices. Figure 6.2 demonstrates a cross section of a planar AlGaN/ GaN HEMT demonstrating the polarization and electric field lines which lead to the formation of a 2DEG. Equation 6.1 shows the net polarization in the 2DEG that is from the combination of the piezoelectric polarization and spontaneous polarization of AlN and GaN. The piezoelectric contribution of AlN (AlGaN) is thought to be much greater than that

of GaN.
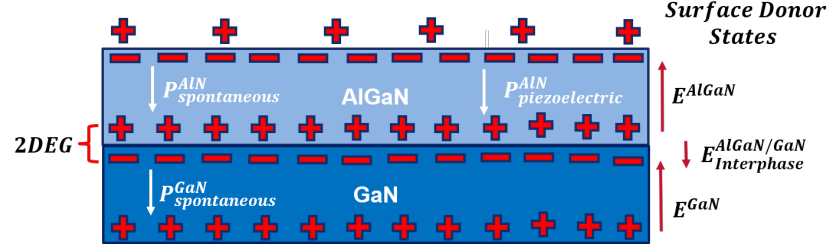
Figure 6.2: **Cross section of a AlGAN/ GaN HEMT device showing the electric field lines that form the 2DEG** Electric field lines of both AlGaN (E^{AlGaN}) and GaN (E^{GaN})point in the opposite direction of spontaneous and piezoelectric polarization. The 2DEG arises from the charge balance at the AlGaN/ GaN interface, ($E_{Interface}^{AlGaN/GaN}$).

$$P_{2DEG} = P_{spontaneous}^{GaN}(1 - x) - (P_{spontaneous}^{AlN}x + P_{piezoelectric}^{AlN}) \qquad (6.1)$$

6.1.3   Built-In Stress within HEMT Structure

Due to the cost of production of GaN, hetero-epitaxial growth is used through molecular beam epitaxy (MBE) or metal organic chemical vapor deposition (MOCVD) onto a substrate of a different material such as silicon (Si), silicon carbide (6H-SiC), or sapphire (Alpha-Al$_2$O$_3$). Epitaxial growth of high quality GaN onto a Si or Al$_2$O$_3$ hetero-substrate is very challenging due to misalignment of the lattice constants which leads to a mismatch in the coefficient of thermal expansion (CTE) (66). This severe misalignment between the deposited GaN film and its substrate leads to a built-in strain and intrinsic stress within the as-grown material, due to the promotion of dislocations. GaN grown on Si is in tensile stress (56%) while GaN grown on sapphire is in compressive stress (16%). The large difference in the CTE and lattice mismatch induces a high defect density within AlGaN / GaN which can be on the order of 10^{10} cm^{-2} (89).

AlGaN has a smaller lattice constant than GaN; growth of AlGaN material on GaN results in lattice mismatch between the two materials causing the AlGaN layer to be grown under tensile strain at the AlGaN/ GaN interphase. For electronics

applications, the AlGaN layer grown on top of GaN is typically limited to a thickness of 30 nm, and critical composition of 30% to prevent crystal cracking. GaN is grown in tension on a Si substrate, and often times an AlN buffer layer is used on the top or bottom of the GaN to compensate for the induced strain (57; 89). μRS has been used to study strain effects on $Al_{0.5}Ga_{0.5}N/GaN$ on crack and dislocation density (93). *In Situ* wafer curvature measurements, later verified by X-Ray Diffraction (XRD) reveal GaN grown on sapphire induces a compressive stress of -0.66 GPa μm at room temperature, and with increasing concentration of Si dopant, GaN can experience an induced tensile stress of up to 0.15 GPa (57). The lattice constant mismatch and coefficient of thermal expansion mismatch between GaN, AlN, and common substrate materials is summarized in Figure 6.3.

Material	Lattice Constant (nm)	Lattice Mismatch %	CTE $(10^{-6}/K)$	CTE Mismatch %	Defect Density (cm^{-2})
GaN	a = 0.3189 c = 0.5185	0%	5.59	0%	10^3- 10^4
AlN	a = 0.3112	0-2.4%	4.5	0-21%	10^3- 10^6
Si	a = 0.3431	17%	2.44	54%	10^9
Alpha - Sapphire	a = 0.4758 c = 1.2991	- 33%	7.5 8.5	35%	> 10^{10}
6H - SiC	a = 0.3081 c = 1.511	3.5	4.2 4.68	25%	$5 * 10^8$

Figure 6.3: **Table showing GaN, AlN, Si, SiC, and Sapphire lattice constant and coefficient of thermal expansion (CTE) mismatch, and dislocation density values.**

The problem of strong residual stress throughout the HEMT stack can be circumvented by releasing the hetero structure from the substrate, which allows the AlGaN/ GaN hetero structure to strain relax to its lowest energy configuration. Some methods to release GaN include laser ablation, mechanical polishing and releasing, and chemical etch releasing; however, these techniques roughen the surface which inhibits the amount of carriers which could contribute to the 2DEG. These

processes are known to increase the defects and dislocation density of the GaN material, which is ideal for stretchable and flexible electronic applications (62). To determine an optimal process to fabricate and release which induces minimal stress into the GaN crystal during stretchable HEMT fabrication, we are exploring two separate approaches with our collaborators: top-down and bottom-up. Both processes are designed to be compatible with plasma dry etching to remove the substrate which is less harsh on the crystal during release from the substrate.

Understanding the origin of stress in AlGaN/ GaN HEMT devices is important because this type of heterostructure is known to have a direct correlation between the number of free carriers in the 2DEG, and the amount of strain in the crystal. Kuball demonstrated that micro-Raman Spectroscopy (μRS) could be used to independently measure both of these material properties: free carrier concentration through the polar A1(LO) peak, and strain through the non-polar E2 (high) peak (90). Many researchers have since then used μRS to monitor the relationship between both of these properties in GaN devices. For example μRS has been used to study the free carrier concentration as a function of the as grown stress in the fabrication of core-shell nanowire InN-GaN on devices (94) and in heavily-doped GaN:Si micro-rods (95). μRS, correlated with FEM results, has also been used to study the stress in GaN micro-beams before and after release (71).

6.2 Raman to Measure Stress in GaN

Raman Spectroscopy has extensively been used to non-invasively locally monitor crystalline quality, such as stress, free carrier concentration, composition, thickness, growth and operating temperature within semiconductor materials (90) through changes in the Raman peak position and bandwidth. The III - V semiconductor compounds GaN, AlGaN, and AlN all crystallize into hexagonal (wurtzite) crystal structures, with four atoms in the primitive unit cell. For these materials, group theory predicts eight sets of phonon modes: $2E_2$, $2A_1$, $2E_1$, and $2B_1$ within the first Brillion Zone (q=0), however, the $2B_1$ mode is not active. The crystal orienta-

tion and polarization configuration of the material determines which phonon modes are observed. All samples evaluated in this thesis are assumed to be in the (0001) c-plane of GaN, which corresponds to a back scattered geometry of $Z(XX)\bar{Z}$. For a full description of the GaN group velocity derivation which explains where the various phonon modes arise from, please see reference (96).

An individual Raman spectrum of single crystal GaN in the $Z(XX)\bar{Z}$ backscattered geometry has three characteristic Raman peaks: E_2(low) 144 cm^{-1}, E_2(high) 568 cm^{-1}, and A_1(LO) 733 cm^{-1} (90; 96). Variations peak frequency position of the E_2(high) is indicative of changes within the stress in the GaN crystal stack, while variations in the peak's full-width half max (FWHM) reveal crystalline quality (90). Additionally, in polar crystals, Raman has been demonstrated as a technique to measure the free carrier concentration and determine the doping-type (n or p type) based on interactions between plasmons and phonons, which is useful information to evaluate HEMT performance; however, this is beyond the scope of discussion in this thesis (90; 95; 96; 97; 98; 99). Figure 6.4 shows the Raman Spectra of A.) (solid) 3.5 μm unintentionally doped GaN, grown on bulk sapphire substrate and B.)(dashed) 1.5 μm intentionally doped AlGaN/GaN, grown on bulk silicon substrate, used as the reference samples in the following studies presented in this thesis.
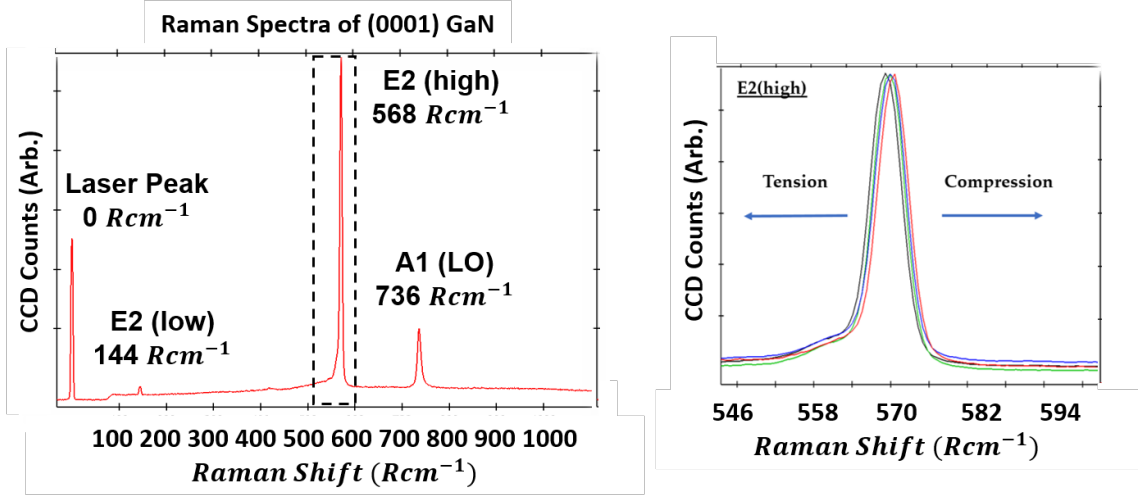
Figure 6.4: **Raman Spectra of μm GaN in the (0001) back scattered geometry on a bulk sapphire substrate.** The image on the right demonstrates the linear relationship between the shift in the E2(high) Raman wavenumber and tensile/compressive stress.

6.2.1 Stress Measurement Methodology

Strain can lead to the formation of defects, which can increase the crack and dislocation density of the material, and is observed through a linear shift in the vibrational frequency position of E_2 (high) mode in the Raman spectra of GaN. Using the phonon deformation potential (DP), Raman peak shift can be resolved into the magnitude of stress and strain present within the crystalline materials, with compressive and tensile stress shifting the frequency to higher and lower values, respectively (90; 100). This can provide extremely useful insight on strain effects induced during growth and during each processing step of a stretchable AlGaN/ GaN HEMT device. Using Equation 6.2, we can determine the stress-induced frequency shift of the non-polar E_2 (high) peak in GaN (101).

$$\Delta\omega = \omega_s - \omega_0 = K\sigma_{xx}cm^{-1} \tag{6.2}$$

Here K is the pressure coefficient for GaN (K = 4.3), ω_s is the frequency of the scattered light and ω_0 is the frequency of the unstrained E_2 (high) position. Kuball suggests biaxial stress shifts linearly with 2.9 GPa $Rcm-1$. A thick (400 μm) bulk

92

single crystal of unstrained GaN was reported to have a characteristic frequency of 567.5 $Rcm-1$ (90; 101).

6.2.1.1 AlGaN / GaN on Si and Sapphire Reference Samples

2D Raman maps of GaN samples can be generated since they are planar while on the wafer. A 70 μm x 70 μm area with a 1 μm step size was scanned at each location, generating a grid composed of 4,900 individual Raman spectra, which creates a Raman map. Figure 6.5 show the Raman position map generated on the 1.5 μm AlGaN / GaN on 650 μm Si reference sample.
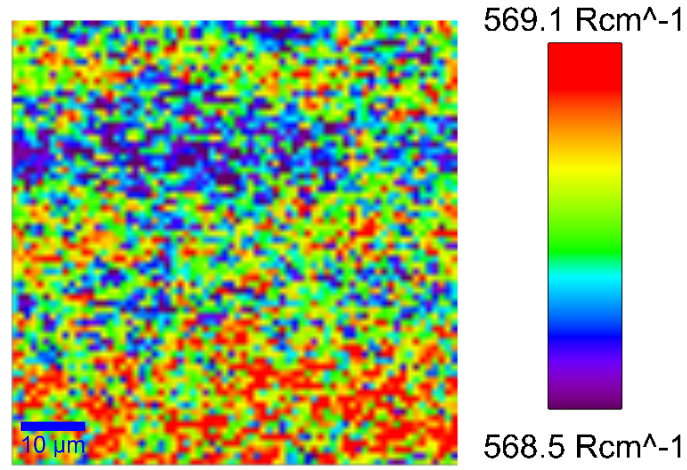
Figure 6.5: **A 70 μm x 70 μm Raman position map of the as-grown AlGaN/ GaN on Si wafer** This sample is used as the reference position for stress values reported in the top-down maps. The average position $w_0 = 568.75$ Rcm^{-1}

An unstrained bulk single GaN crystal was reported to have an E_2 (high) phonon mode corresponding to $w_0 = 567$ Rcm^{-1}. If we take the average Raman value for AlGaN / GaN grown on Si reported in Figure 6.5, as $w_s = 568.75$ Rcm^{-1}, then the built-in stress in this crystal can be calculated using $\delta\omega = w_s$ - $w_0 = 4.3\sigma$. Therefore the built-in stress of the GaN on Si reference sampl is $\sigma = $ (568.75 - 567.5)/4.3 = +0.29 GPa . Note the sign of stress is positive which indicates this sample is under tensile stress of GPa. The following measurements will report stress changes with respect to the built in stress of the crystal (i.e $w_0 = 568.75$ Rcm^{-1}

is the 0 stress/ strain position). Following the same procedure above on the GaN on sapphire reference sample used in the bottom-up study (spectra shown in Figure 6.4) we find an average position of which results in a built-in stress of -0.35 GPa of compressive stress. All stress values reported are changes from the reference as-grown materials.

6.3 Stress Measurements on Bottom-Up AlGaN/GaN HEMTs: Results and Analysis
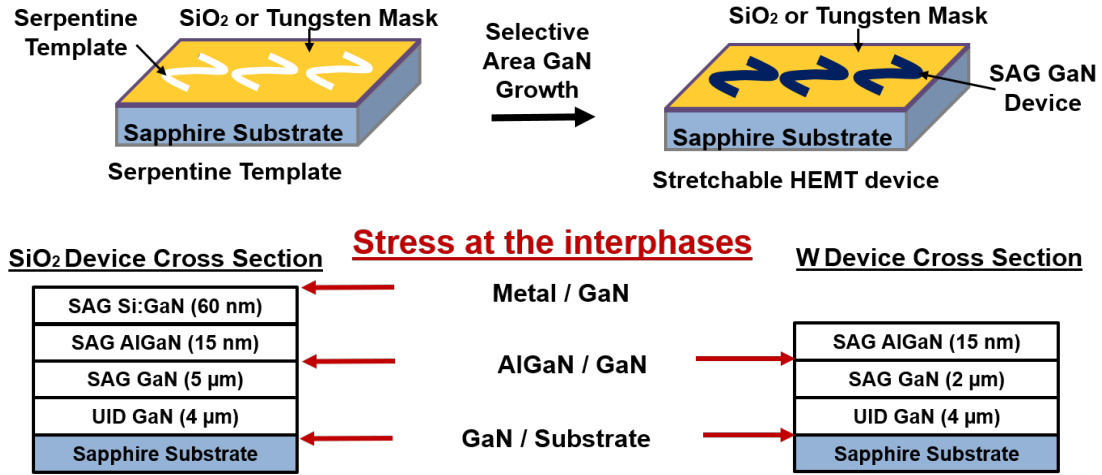
Figure 6.6: **Diagram demonstrating the bottom-up fabrication approach to build a stretchable AlGaN / GaN HEMT using selective area growth (SAG).** SAG was performed using metal organic chemical vapor deposition (MOCVD). Cross sections of the HEMT devices fabricated using the silicon dioxide mask and tungsten mask are also included, with arrows pointing to the the interfaces were stress is expected to be found.

6.3.1 Bottom-Up Approach Background

In this study, I use μRS to map the surfaces stresses within stretchable AlGaN/GaN HEMTs grown using the bottom-up, selective area growth (SAG) method, with metal organic chemical vapor deposition (MOCVD). Two masking materials were evaluated (silicon dioxide and tungsten) on the stress within the grown stretchable AlGaN/ GaN HEMT device, while still on its planar sapphire substrate. Since

these devices were still on the substrate, the WITec Raman Spectroscopy instrument we have in house is equipped with a piezoelectric XY stage, is suited to generate large area stress maps on these samples. For this study, I used a WITec Alpha300RA confocal Raman Microscope, with 300 nm spatial resolution. An Nd:YAC 1064 nm frequency doubled excitation laser source (532 nm) with 1 mW power was focused on a sample through a 100 X microscope objective lens. A 70 μm x 70 μm large area map with a step size of 1 μm was collected using a 1800 g/mm grating spectrometer equipped with a charge coupled detector (CCD), with resolution of 0.1 Rcm^{-1} . Measurements were carried out in the backscattered geometry of $Z(XX)\bar{Z}$, with 0.5 second time integrations and 60 accumulations, to reduce the signal-to-noise ratio. The position and intensity of the laser peak in the Raman spectra's were used as the calibration reference position between samples.

The bottom-up devices characterized in this study were grown, fabricated, and graciously provided by Ms. Isra Mahaboob (Ph.D. student) in Prof. Shadi Shahedipour-Sandvik's group in the College of Nanoscale Science and Engineering at SUNY Polytechnic Institute, Albany, NY. Information regarding the specifics in the growth procedures from this group are reported elsewhere (101; 102; 103; 104).

6.3.2   Selective Area Growth with SiO_2 Mask

The first device evaluated in this study was a SAG Stretchable AlGaN/ GaN HEMT grown using a SiO_2 mask. The device was already deposited with a Ti/Al/Ni/Au (20/120/60/50 nm) metal contact along the Bend and Straight part of the sinusoid serpentine device, leaving the Amplitude of the device exposed with crack free Al-GaN/ GaN crystal. Figure 6.7 demonstrates an optical image, laser intensity plot of the E_2 peak used to evaluate stress, and the surface stress map on the Amplitude and Bend of this device.
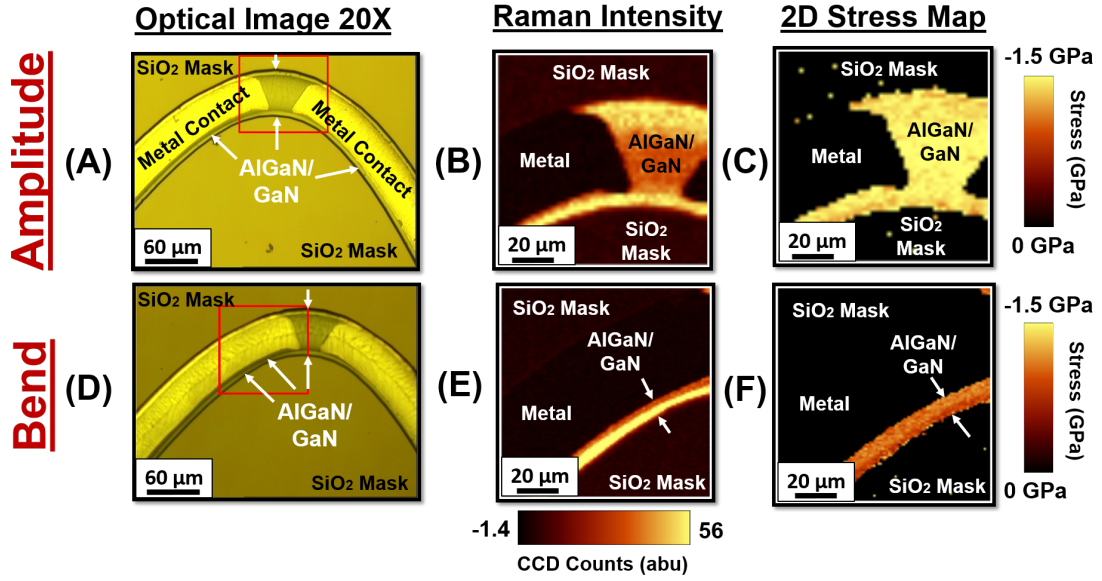
Figure 6.7: **2D Raman stress maps of bottom-up SAG AlGaN/ GaN HEMTs with the SiO_2 Mask.** The left column (A) and (D) show the optical images of the mapped regions along Amplitude and Bend, indicated by a red square. The middle column (B) and (E) show the laser intensity plot of the GaN E_2 peak, used to extrapolate stress. Finally the right column (C) and (F) shows the 2D stress maps calculated for the Amplitude and Bend of this stretchable AlGaN/ GaN HEMT.

As shown in Figure 6.7, there is an average stronger compressive stress in the Amplitude than in the Bend (-1.5 GPa and -1.3 GPa respectively). The likely reason for the reduction in stress within the Bend of the serpentine is due to the deposited metal contact. The lattice constant of the metal contact is smaller than that of the AlGaN/ GaN, which induces tension the surface of the crystal. As a result, the magnitude of stress within the edge of the HEMT along the Bend is 300 MPa lower than the magnitude of stress within the Amplitude.

6.3.3 Selective Area Growth with Tungsten (W) Mask

Repeating the same procedure from above, I evaluated the surface stress on a SAG Stretchable AlGaN/ GaN HEMT grown using a tungsten (W) metal mask. This serpentine had the same dimensions are the device characterized with the silicon dioxide mask; however this device had no deposited metal contacts. The region measured was a crack free region of exposed AlGaN / GaN crystal in the

stretchable serpentine geometry. The optical image, Raman intensity, and 2D stress map of this device is shown in Figure 6.8.
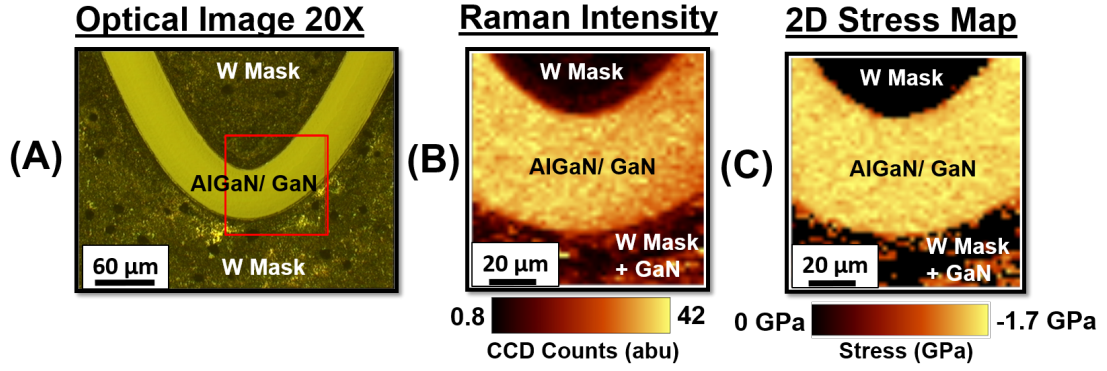
Figure 6.8: **2D Raman stress map of bottom-up SAG AlGaN/ GaN HEMT fabricated with the tungsten metal mask.** (A) shows the optical image of the mapped region, indicated by the red square. (B) shows the laser intensity plot of the GaN E_2 peak, used to extrapolate stress. (C) shows the calculated 2D stress map.

The stress map on this device reveals a uniform stress distribution along the SAG AlGaN/ GaN crystal. The magnitude of stress is slighly higher in the sample grown with the tungsten mask than with the silicon dioxide mask (-1.7 GPa vs -1.5 GPa respectively). This could be due to a lack of top metal contact. Additionally, upon evaluation of the FWHM in the spectra of tungsten and silicon dioxide masked samples, the FWHM was narrower in the tungsten mask sample which indicated a lower dislocation density and a purer crystal. In the future we will look into comparing stress in serpentines with similar cross sections grown using the two different masking materials.

6.4 Stress Measurements on Top-Down AlGaN/GaN HEMTs: Results and Analysis
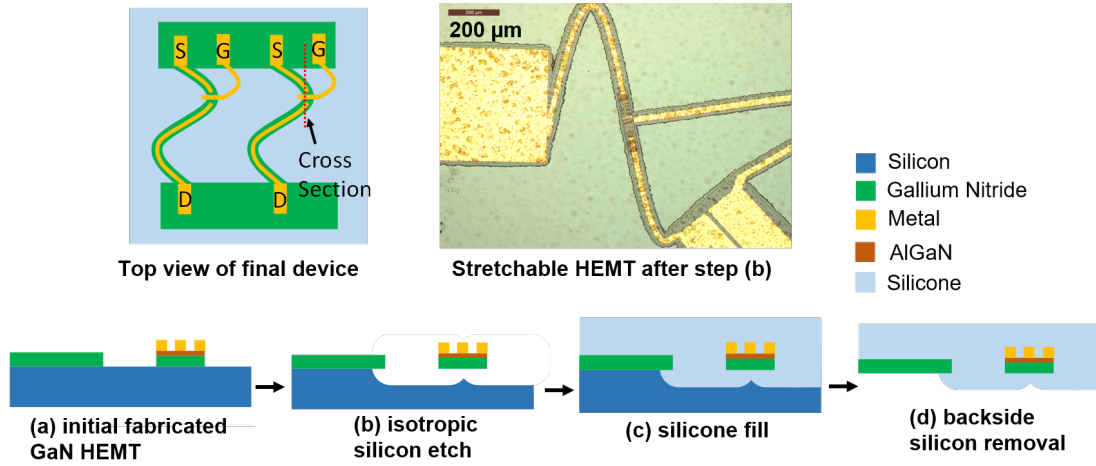
Figure 6.9: **Top-down fabrication approach for stretchable AlGaN/GaN HEMTs.** Simplified fabrication approach of the top-down devices tested, developed by Dr. Randy Tompkins and Dr. Nathan Lazarus. Step (a) uses standard photolithography and micro-machining processes to develop a HEMT device into a stretchable geometry. Step (b) performs an isotropic plasma etch to undercut the HEMT from the Si wafer. Step (c) pours liquid silicone onto the front side of the device to encapsulate and protect the structure. Step (d) is a backside removal of the Si substrate using plasma etching (3).

6.4.1 Top-Down Approach Background

The second fabrication method explored is referred to as the top-down approach. The top-down method initially starts with a wafer of crystalline material, and then one performs traditional photolithography and micro-machining processes to etch a device into a desired geometry. The top-down stretchable AlGaN/GaN HEMT devices explored in this study were fabricated by my collaborators and mentors Dr. Randy Tompkins and Dr. Nathan Lazarus at the Army Research Lab. The general fabrication procedure they developed is shown in Figure 6.9. First the HEMT structure is fabricated into a stretchable geometry on a 1 cm x 1 cm piece part from an AlGaN/GaN/Si (30 nm / 1.47 μm / 650 μm) wafer using a traditional fabrication approach (89). Next, XeF_2 is used to isotropically undercut the struc-

ture, followed by device encapsulation in an elastomer (Sylgard 184). Sylgard 184 is the same silicone rubber modeled in chapter 3. Finally, the Si substrate is removed from the backside of the device using Xenon Diflouride (XeF_2) gas chemistry to fully release the device into the elastomer substrate (2; 3).

6.4.2 Stress in AlGaN/ GaN HEMT on the wafer

Here I use micro-Raman spectroscopy as a stress monitoring technique during the fabrication of a stretchable AlGaN/ GaN HEMT using the top-down approach. The stress was previously evaluated on the wafer from the original as-grown crystal. Next, I generate a stress map of the stretchable AlGaN/ GaN HEMT while on the wafer, as shown in Figure 6.10. The zero stress reference state was selected as the average value of $w_0 = 568.75\ Rcm^{-1}$ from the as-grown material. This device went under many fabrication steps including photolitograpy, metal deposition, and anisotropic-plasma etching to define the HEMT device into a serpentine geometry. The map results shown in Figure 6.10 (D) show that these fabrication procedures induce up to 0.5 GPa of tensile stress within the AlGaN/ GaN crystal layer along the amplitude of this serpentine.
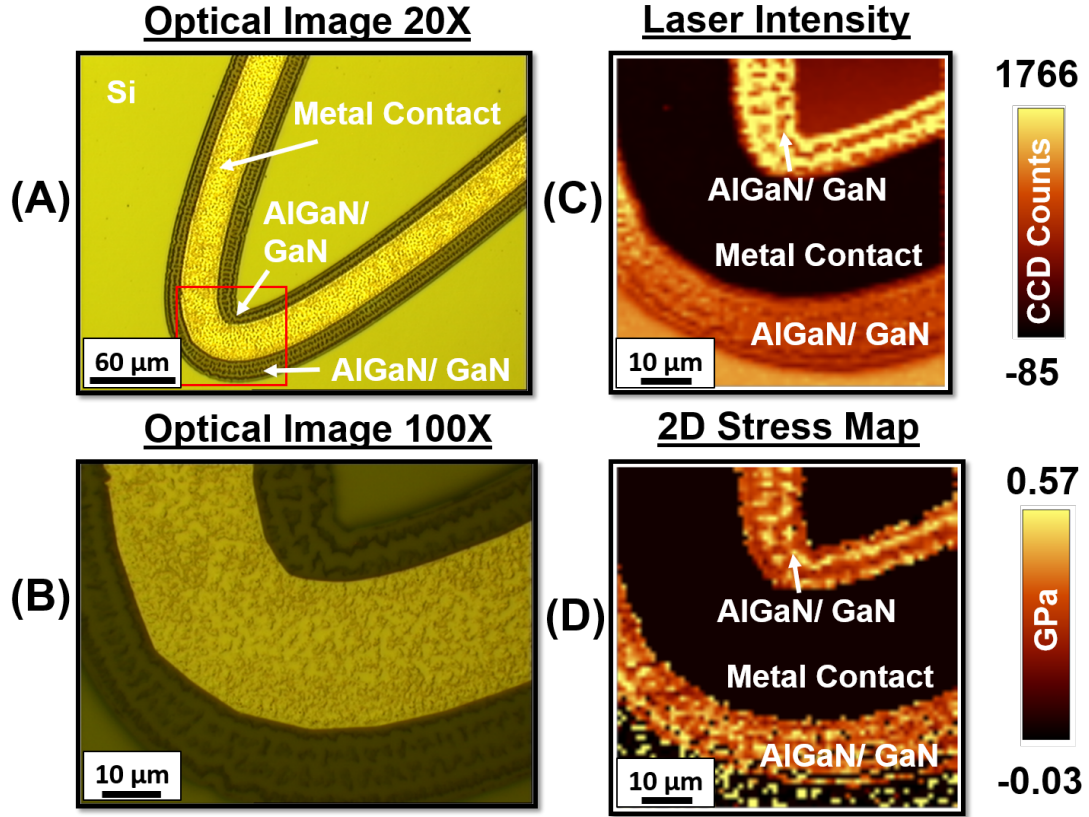
Figure 6.10: **2D Raman stress map of a top-down stretchable AlGaN/ GaN HEMT on the Si wafer.** The optical image of the device measured for the map is shown with a 20X objective in (A) and with a 100X objective in (B). The laser intensity of the E2 (high) phonon peak is shown in (C), and finally the stress map of the device in (D).

6.4.3 Stress in AlGaN/GaN HEMT when Released and Embedded into a Stretchable Substrate

Next, I evaluate the the surface stress within a released and encapsulated Stretchable HEMT, step (d) in Figure 6.9. This device was encapsulated on the top side of the device, leaving the back of the device exposed for Raman measurements. Since GaN is transparent, we can see the metal contact on the other side of the device, also encapsulated in the silicone. Figure 6.11 show the optical image, Raman map intensity, and stress map of the released device.
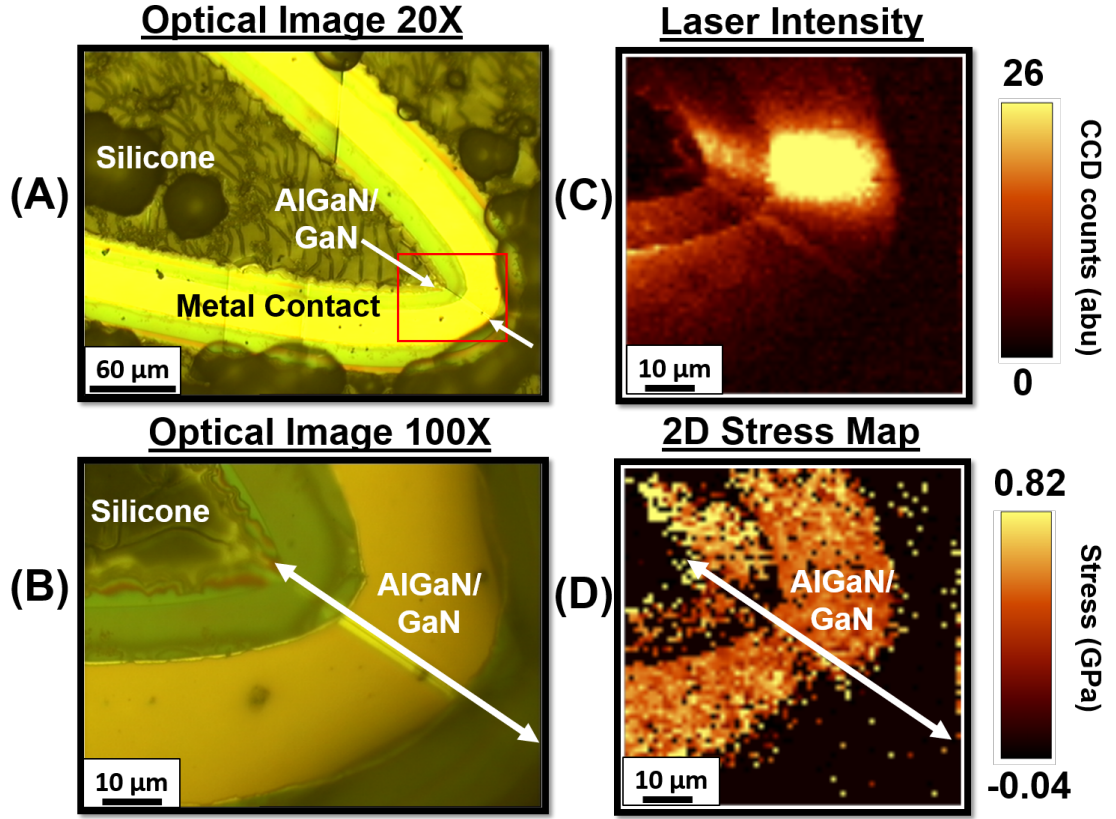
Figure 6.11: **2D Raman stress map of a top-down stretchable AlGaN/ GaN HEMT released from the Si wafer and encapsulated in silicone.** The optical image of the device measured for the map (back side of GaN) is shown with a 20X objective in (A) and with a 100X objective in (B). The laser intensity of the E_2 (high) phonon peak is shown in (C), and finally the stress map of the device in (D).

These results indicate that removal of the silicon substrate and encapsulation within an elastomer increases the tensile stress of the device by 300 MPa. This induced stress would be advantageous for a stretchable AlGaN/ GaN HEMT device because this would induce additional free carriers within the 2DEG of the device.

6.5 Stress Measurements in AlGaN/GaN HEMTs Conclusions

Micro-Raman spectroscopy was shown to be a viable optical stress monitoring tool during the fabrication and processing of GaN crystals. In this chapter I used micro-Raman spectroscopy to evaluate the surface stresses in stretchable AlGaN/

GaN HEMT samples fabricated through two separate approaches: bottom-up (silicon dioxide and tungsten mask) on sapphire substrates and top-down (on a Si substrate and encapsulated in silicone after substrate removal). Through measurement of the E_2(high) phonon peak, it was revealed epitaxial growth of AlGaN/GaN on a sapphire substrate induces intrinsic compressive stress while AlGaN/GaN growth on a silicon substrate induces tensile stress due to differences in lattice constants and coefficient of thermal mismatch. Next, I evaluated the stress in two stretchable serpentine HEMT devices grown through the selective area method (bottom-up) with two different masking materials (silicon dioxide and tungsten) onto sapphire substrates. Both samples were shown to have an induced compressive stress, however, the sample grown with the tungsten mask was under a higher order of magnitude of compressive stress. A possible explanation for this is the tungsten masked sample had no metal contact on the top surface which could induce a counter tensile stress, as in the case with silicon dioxide sample.

Next, I evaluated induced tensile stress during the fabrication of stretchable AlGaN / GaN HEMTs on silicon substrates through the top-down fabrication approach. Measurements were taken on the as grown material, stretchable HEMT device fabricated on the wafer, and substrate removed (device encapsulated in silicone). The HEMT device fabricated on the Si wafer was under up to +0.60 GPa of tensile stress. It was shown that as the silicon substrate is removed after it is encapsulated within silicone rubber, the tensile surface stress of the HEMT device increased by +0.3 GPa of stress. Since GaN and AlGaN are piezoelectric materials, an increase in tensile stress would indicate an increase in the number of free carriers in the device. Micro-Raman spectroscopy can independently measure both of these phenomena, and future studies by our group will explore the piezoelectric coupling effects between induced tensile stress and generated electric charge in stretchable AlGaN / GaN HEMT devices. These findings further support GaN-on-Si technology will becoming exciting for wearable electronics in the future.

Chapter 7:   Outlook for Stretchable Crystalline Materials

7.1   Conclusions and Summary of Contributions

Throughout my Masters thesis, I showed modeling, fabrication, and characterization results on the mechanical performance of the stretchable crystalline semiconductors silicon and gallium nitride. The research presented has yielded the following contributions and main conclusions:

(i.) Stretchable anisotropic modeling of crystalline semiconductors. I used finite element analysis, through COMSOL Multiphysics 5.2 to evaluate the effect of mechanical anisotropy on stretchable behavior of (0001) GaN and (100) Si. It was determined that serpentine geometries can offer a reduction in the von Mises peak stress by 20 to 90%, with geometries displaying strong curvature, such as Curved Corner or Horseshoe, demonstrated improved stretchable behavior over geometries with sharp corners. I showed (0001) GaN displays isotropic stretchable behavior which means there is no crystallographic orientation dependence on mechanical behavior for GaN devices fabricated in this plane; however, (100) Si displays strong stretchable anisotropic behavior, with the <100> orientation performing the best. I showed this anisotropic dependence as a function of serpentine stiffness through varying the width-to-radius ratio (0 to 0.6) can results in a 12% variation in the tensile strain results of Rectangular serpentine structures and a 36% variation for Curved Corner serpentine structures. At small w/r ratios both the Curved Corner and Rectangular structure could reach large strain-to-ruptures of > 100% which is attributed to an out-of-plane buckling mode to relieve stress under strain, which far exceeds the expected intrinsic tensile strain of Si (< 1%). At high w/r ratios it was found these structures were confined to in-plane deformations to relieve stress

under strain and thus achieved lower strain-to-ruptures, however; they could still the minimum 30% tensile strain requirement for wearable electronics. These results then indicate that more square-like serpentine geometries display less variation in their mechanical properties due to crystalline anisotropy than geometries with curvature. Overall, mechanical anisotropy presents many challenges when fabricating stretchable devices in (100) Si, therefore, I recommend fabrication on a (111) Si wafer for processes requiring uniform devices, which would result in Si devices with isotropic stretchable behavior.

(ii.) Stretchable fabrication and release process of crystalline materials. I demonstrate a micro-fabrication process which allows for the release of free standing 2D in-plane Si serpentines, with freedom to tune many geometrical parameters such as serpentine amplitude, wavelength, width, and thickness. This process is compatible with other fabrication procedures such as metal and dielectric deposition, which are essential components in most device fabrication processes. With careful optimization my process can be adapted to develop released free standing stretchable Si device such as sensors, actuators, and solar cells, without requiring the presence of an elastomer support. I have also proposed a modified process flow which will allow for the release of stretchable single crystal GaN (and most III-V materials), which will eventually be employed to fabricate free-standing stretchable AlGaN/ GaN HEMT devices.

(iii.) In-situ stress characterization and fatigue evaluation of stretchable Si with micro-Raman spectroscopy. Measuring local stress/strain within silicon micro-electronics is well known using micro-Raman spectroscopy. For the first time, I demonstrated an application of micro-Raman spectroscopy to measure stress within a stretchable Si Curved Corner serpentine, while applying external strain of 0 72%. With this technique, I could resolve the local non-uniform stress distribution, with a resolution of 50 MPa, along three different locations of the Si serpentine (Amplitude, Bend, and Straight). For the case of a <100> Si Curved Corner serpentine the *in-situ* stress measurements revealed the largest peak stress distribution were found to concentrate in the Bend (-0.6 GPa to 1.2 GPa) which is the region which

undergoes the most out-of-plane buckling deformation after applying a 72% uniaxial external strain. The minimum stress was found to concentrate along the Straight part of the trace (-0.1 GPa to +0.25 GPa), and the amplitude ranged from (-0.15 GPa to + 0.25 GPa) after applying a 72% uniaxial external strain. I also performed preliminary low-cycle fatigue tests showing after 0 - 15 cycles, from 0 40% the stress varied in the Amplitude by (0.015 GPa to -0.175 GPa), in the by (0.7 GPa to 0.5 GPa (-28%), and Straight by (0.05 GPa to -0.04 GPa, -180%). These results would need further exploration with other experiments such as X-Ray Diffraction or high-cycle fatigue testing to draw conclusive results regarding the elastic/plastic behavior of stretchable crystalline Si. Additionally, I demonstrated a strain-to-fracture on a <110> Si Curved Corner serpentine at 84% which is in excellent agreement with the FEA modeling results. While I demonstrated micro-Raman Spectroscopy stress measurements with only Si, the methods I described could be adapted to measure stress and evaluate fatigue with many crystalline materials which have well-defined phonon deformation potentials, which relate stress to Raman frequency shifts.

(iv.) Stress monitoring during fabrication of stretchable AlGaN / GaN HEMT devices using micro-Raman spectroscopy. Gallium nitride is another material with a well-known relationship between stress and Raman frequency shift of the E2(high) phonon peak. During the fabrication of Stretchable AlGaN/ GaN high electron mobility transistors (HEMT), I applied micro-Raman Spectroscopy as a stress monitoring technique to spatially map and resolving the surface stresses of GaN devices fabricated through two different approaches: bottom-up and top-down. First, the stress was resolved in the reference samples (as-grown materials) where 3 μm GaN on bulk sapphire had an intrinsic stress of (-1.0 GPa) while 1.5 μm AlGaN/GaN on bulk Si had an intrinsic tensile stress of (+0.29 GPa), with respect to the literature value of unstrained bulk GaN. The first method, bottom-up approach, creates a stretchable AlGaN/ GaN HEMT devices on a sapphire substrate through selective area hetero-epitaxial growth. Using two-different masking materials, it was found selective area growth induced further compressive stress in the crystal, averaging (-1.3 to -1.5 GPa) with a SiO_2 mask and (-1.7 GPa) with a W

mask. The area measured with an W mask had no metal contact while the area measured with the SiO_2 mask contained a deposited front metal contact. I speculate the stress is lower in the SiO_2 mask due to the metal contact inducing tensile stress within the surface of AlGaN/ GaN crystal, resulting in an average lower magnitude in stress. Lastly, I evaluated effect of removing the silicon substrate and embedding a stretchable AlGaN/ GaN HEMT device into a stretchable substrate, through the top-down approach. It was shown that traditional processing of the HEMT structure onto the wafer induced (+0.5 GPa) of tensile stress within the HEMT device while on the wafer. Further processing to undercut the structure, encapsulate the device in silicone, and remove the Si substrate was shown to induce an additional stress of 300 MPa average the total stress to (+0.8 GPa). Overall, these results show micro-Raman spectroscopy is an extremely useful tool for fabrication processes monitoring, and characterization of stretchable GaN devices. In the future we will explore similar measurements while straining the GaN devices, using similar methods reported in the Si case.

7.2 Future Work

Future research opportunities on stretchable crystalline materials is quite fruitful and expected to explode in the years to come. Raman spectroscopy is well known as a fast, non-destructive characterization technique to measure residual and applied stress, and monitor the local strain within crystalline semiconductors and other materials. The work presented in this thesis demonstrated a micro-Raman Spectroscopy as a direct stress measurement technique while applying external strain to stretchable single crystalline Si serpentines and as stress monitoring technique during various stages of the production of and stretchable single crystal GaN devices. While only two stretchable single crystal materials were explored in my studies, the techniques developed in this thesis can be adapted to use micro-Raman Spectroscopy measure stress within other stretchable crystalline materials where the phonon-deformation potential is well-known for example possible candidates include diamond and zinc-blend type semiconductors include Ge, GaAs, GaSb, InAs, and ZnS [105]. Raman can also be used to determine induced crystal stress within polycrystalline thin films (i.e synthetic diamond films) due to growth on multiple substrate materials (i.e alumina, tungsten carbide, SiAlON, and SiO_2 glass) [106] and can even resolve the stress dependence on the exact microcrystal shapes within polycrystalline films [107]. Additionally, Raman has been shown to measure stress in dielectric films deposited onto crystalline semiconductor materials such as Si_3N_4 [74], SiO_2 [86], and anatase TiO_2 [108], which are thin-film materials integrated as absorption layers in crystalline solar cells (Si and GaAs), and AlGaN/ GaN HEMT devices. With all of the exciting material classes readily available for stress characterization using micro-Raman Spectroscopy, the doors are wide open to use implement this as a standard crystalline stretchable electronic technique.

The next steps to continue the studies I presented in this thesis would be to integrate the fabrication and characterization techniques I developed to build stretchable crystalline power and energy devices. One such device I briefly explored with my undergrad capstone senior design team during the 2016 - 2017 school year

is stretchable Si photovoltaic devices. Since Si is the most brittle component in a solar cell, this is the limiting material to produce a stretchable solar cell. We developed two fabrication approaches that allowed us to develop a Si solar cell, etched into a stretchable serpentine geometry, with both a lateral and a vertical PN junction, as shown in Figure 7.1. While the preliminary devices we demonstrated were stretchable solar cells patterned into single serpentine traces on the wafer, this process could be combined with my previously described fabrication process to release stretchable solar cells from the wafer. I would suggest characterization on a solar cell fabricated into a traditional geometry, released from the wafer, and while stretched under tension to determine the change in the device's mechanical and electrical performance under applied external strain. In addition to performance monitoring with micro-Raman Spectroscopy, complimentary measurements would include high resolution X-Ray diffraction to determine the change in the lattice constant spacing, and nanoscale functional imaging with photoluminescence spectroscopy to resolve the changes in the band-gap behavior of the device as a function of applied external strain(109).
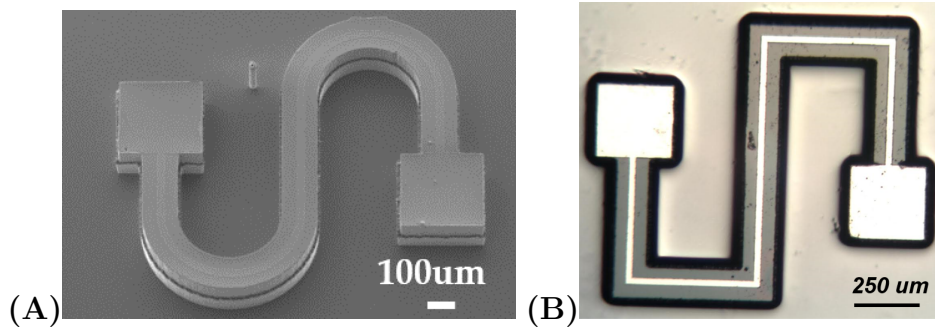

Figure 7.1: **Fabricated stretchable silicon photovoltaic devices.** (A) shows a scanning electron microscopy image of a curved corner PV on the Si wafer (B) shows an optical image of a rectangle PV with a top metal contact.

7.3 Products of this Research

7.3.1 Honors and Awards

[1] Recipient of the 2018 National Science Foundation (NSF) Graduate Research Fellowship Program (GRFP) Fellowship (April 2018)

[2] Undergraduate Finalist: National Inventors Hall of Fame Collegiate Inventors Competition (November 2017)

[3] First Place in the U.S Army Research Labs (ARL) Sensors and Electron Devices Directorate Summer Student Oral Presentation: Branch, Division, and Directorate Undergraduate Winner (July 2017)

[4] Second Place Poster Award Mid-Atlantic Micro-Nano Alliance (MAMNA) Spring 2017 Symposium (April 2017)

7.3.2 Oral Presentations

[1] Micro-Raman Spectroscopy for Stress Mapping of Crystalline Stretchable Semiconductors **S.M. Curtis**, R. Tompkins, B. Nichols, I. Kierzewski, and N. Lazarus Invited Seminar Talk University of Kiel. Kiel, Germany. December 18, 2017

[2] Effect of Mechanical Anisotropy in Silicon and Gallium Nitridde for Stretchable Electronics **S.M. Curtis**, R. Tompkins, and N. Lazarus Army Research Labs Sensors and Electron Devices Directorate Summer Student Competition. Adelphi, MD. July 16-27, 2017

7.3.3 Posters

[1] Design, Fabrication, and Characterization of Stretchable Silicon Photovoltaic Devices **S.M. Curtis**, H. Wang, A. Randolph, G. Anfinrud, G. Vostal, and K. Chang. Capstone Senior Design Day 2017. University of Maryland, College Park, MD. May 2017.

[2] Effect of Mechanical Anisotropy in Gallium Nitride and Silicon for Stretchable Electronics **S.M Curtis**, H. Wang, R. Tompkins, N. Lazarus. Poster: Mid Atlantic

Micro-Nano Alliance (MAMNA) Spring 2017 Symposium. Johns Hopkins Applied Physics Laboratory, Laurel, MD. April 2017.

7.3.4 Publications

[1] Growth and Characteristics of Nanostructured IrOx Films M.B Graziano, B. Hanrahan, B. Sanchez, T. Parker, **S. Curtis**, M. Rivas, and P. Sunal In preparation April 2018

Bibliography

[1] John A Rogers, Takao Someya, and Yonggang Huang. Materials and mechanics for stretchable electronics. *Science*, 327.5973:1603 – 1607, 2010.

[2] R P Tompkins, I Mahaboob, F Shahedipour-Sandvik, and N Lazarus. Mechanical Analysis of Stretchable AlGaN/GaN High Electron Mobility Transistors. *ECS Transactions*, 72.5:89–95, 2016.

[3] R. P. Tompkins, I. Mahaboob, F. Shahedipour-Sandvik, and N. Lazarus. Electrical properties of AlGaN/GaN HEMTs in stretchable geometries. *Solid-State Electronics*, 136:36–42, 2017.

[4] Defense advanced research projects agency warrior web *https://www.darpa.mil/program/warrior-web*, 2018.

[5] Energy and power division u.s. army research laboratory *https://www.arl.army.mil/www/default.cfm?page=2563*, Feb 2015.

[6] Azonano: Applications of silicon in mems devices *https://www.azonano.com/article.aspx?ArticleID=3835* 2014.

[7] Jerry L. Hudgins, Grigory S. Simin, Enrico Santi, and M. Asif Khan. An assessment of wide bandgap semiconductors for power devices. *IEEE Transactions on Power Electronics*, 18(3):907–914, 2003.

[8] Kristen Bethke. The Second Skin Approach: Skin Strain Field Analysis and Mechanical Counter Pressure Prototyping for Advanced Spacesuit Design. *M.Sc. thesis*, pages 26–30, 2005.

[9] Nando Kaminski and Oliver Hilt. SiC and GaN devices wide bandgap is not all the same. *IET Circuits, Devices & Systems*, 8(3):227–236, 2014.

[10] Xiao Guang He, De Gang Zhao, and De Sheng Jiang. Formation of two-dimensional electron gas at AlGaN/GaN heterostructure and the derivation of its sheet density expression. *Chinese Physics B*, 2015.

[11] D.S. Gray, J. Tien, and C.S. Chen. High-Conductivity Elastomeric Electronics. *Advanced Materials*, 16(5):393–397, mar 2004.

[12] J. A. Rogers and Y. Huang. A curvy, stretchy future for electronics. *Proceedings of the National Academy of Sciences*, 2009.

[13] Dae-Hyeong Kim and J. A. Rogers. Stretchable and Foldable Silicon Integrated Circuits. *Science Mag*, 320(April):507–511, 2008.

[14] Dae Hyeong Kim and John A. Rogers. Stretchable electronics: Materials strategies and devices. *Advanced Materials*, 20(24):4887–4892, 2008.

[15] Dae Hyeong Kim, Jianliang Xiao, Jizhou Song, Yonggang Huang, and John A. Rogers. Stretchable, curvilinear electronics based on inorganic materials. *Advanced Materials*, 22(19):2108–2124, 2010.

[16] Thomas Widlund, Shixuan Yang, Yung-Yu Hsu, and Nanshu Lu. Stretchability and compliance of freestanding serpentine-shaped ribbons. *International Journal of Solids and Structures*, 51(23-24):4026–4037, nov 2014.

[17] Wei Liu, Min-Sang Song, Biao Kong, and Yi Cui. Flexible and Stretchable Energy Storage: Recent Advances and Future Perspectives. *Advanced Materials*, 2017.

[18] Rak-Hwan Kim Kim, Dae-Hyeong , Nanshu Lu, Rui Ma, Yun-Soung Kim, Ki Jun Yu Shuodao Wang, Jian Wu, Sang Min Won,Hu Tao, Ahmad Islam, Hyun-Joong Chung Tae-il Kim, Raeed Chowdhury, Ming Ying, Lizhi Xu Ming Li, Fiorenzo G. Omenetto Hohyun Keum,Martin McCormick, Ping Liu, Yong-Wei Zhang, and John A. Rogers Yonggang Huang, Todd Coleman. Epidermal Electronics. *Science*, 333(6044):838–843, 2011.

[19] Dae-Hyeong Kim, Nanshu Lu, Yonggang Huang, and John A. Rogers. Materials for stretchable electronics in bioinspired and biointegrated devices. *MRS Bulletin*, 37(03):226–235, mar 2012.

[20] Dae-Hyeong Kim, Nanshu Lu, Roozbeh Ghaffari, and John A Rogers. Inorganic semiconductor nanomaterials for flexible and stretchable bio-integrated electronics. *NPG Asia Materials*, 4(4):e15–e15, apr 2012.

[21] Dae-Hyeong Kim, Roozbeh Ghaffari, Nanshu Lu, and John A. Rogers. Flexible and Stretchable Electronics for Biointegrated Devices. *Annual Review of Biomedical Engineering*, 14(1):113–128, aug 2012.

[22] J A Rogers, Z Bao, K Baldwin, A Dodabalapur, B Crone, V R Raju, V Kuck, H Katz, K Amundson, J Ewing, and P Drzaic. Paper-like electronic displays: large-area rubber-stamped plastic sheets of electronics and microencapsulated electrophoretic inks. *Proceedings of the National Academy of Sciences of the United States of America*, 98(9):4835–40, apr 2001.

[23] M. Stoppa and C. Alessandro. Wearable electronics and smart textiles: a critical review. *Sensors*, 14.7, 2014.

[24] Darren J. Lipomi and Zhenan Bao. Stretchable, elastic materials and devices for solar energy conversion. *Energy & Environmental Science*, 2011.

[25] Darren J. Lipomi, Benjamin C K Tee, Michael Vosgueritchian, and Zhenan Bao. Stretchable organic solar cells. *Advanced Materials*, 23(15):1771–1775, 2011.

[26] Tsuyoshi Sekitani, Hiroyoshi Nakajima, Hiroki Maeda, Takanori Fukushima, Takuzo Aida, Kenji Hata, and Takao Someya. Stretchable active-matrix organic light-emitting diode display using printable elastic conductors. *Nature Materials*, 2009.

[27] Kuniharu Takei, Toshitake Takahashi, Johnny C. Ho, Hyunhyub Ko, Andrew G. Gillies, Paul W. Leu, Ronald S. Fearing, and Ali Javey. Nanowire active-matrix circuitry for low-voltage macroscale artificial skin. *Nature Materials*, 9(10):821–826, 2010.

[28] Ashu K. Bansal, Shuoben Hou, Olena Kulyk, Eric M. Bowman, and Ifor D.W. Samuel. Wearable Organic Optoelectronic Sensors for Medicine. *Advanced Materials*, 2015.

[29] Yihui Zhang, Yonggang Huang, and John A. Rogers. Mechanics of stretchable batteries and supercapacitors. *Current Opinion in Solid State and Materials Science*, 2015.

[30] D.-Y. Khang. A Stretchable Form of Single-Crystal Silicon for High-Performance Electronics on Rubber Substrates. *Science*, 311(5758):208–212, jan 2006.

[31] S.P. Lacour, J. Jones, S. Wagner, Teng Li, and Zhigang Suo. Stretchable Interconnects for Elastic Electronic Surfaces. *Proceedings of the IEEE*, 93(8):1459–1467, aug 2005.

[32] Jun Tang, Hao Guo, Miaomiao Zhao, Jiangtao Yang, Dimitris Tsoukalas, Binzhen Zhang, Jun Liu, Chenyang Xue, and Wendong Zhang. Highly Stretchable Electrodes on Wrinkled Polydimethylsiloxane Substrates. *Scientific Reports*, 5:1–9, 2015.

[33] Mario Gonzalez, Fabrice Axisa, Mathieu Vanden Bulcke, Dominique Brosteaux, Bart Vandevelde, and Jan Vanfleteren. Design of metal interconnects for stretchable electronic circuits. *Microelectronics Reliability*, 48(6):825–832, 2008.

[34] I. D. Johnston, D. K. McCluskey, C. K.L. Tan, and M. C. Tracey. Mechanical characterization of bulk Sylgard 184 for microfluidics and microengineering. *Journal of Micromechanics and Microengineering*, 2014.

[35] N Bowden, S Brittain, AG Evans, JW Hutchinson, and GM Whitesides. Spontaneous formation of ordered structures in thin films of metal supported on an elastomeric polymer. *Nature*, 393:146–149, 1998.

[36] T Sekitani, Y Noguchi, K Hata, T Fukushima, T Aida, and T Someya. A Rubberlike Stretchable Active Matrix Using Elastic Conductors. *Science*, 321:1468–1472, 2008.

[37] Nanshu Lu, Zhigang Suo, and Joost J. Vlassak. The effect of film thickness on the failure strain of polymer-supported metal films. *Acta Materialia*, 2010.

[38] Yihui Zhang, Sheng Xu, Haoran Fu, Juhwan Lee, Jessica Su, Keh-Chih Hwang, John A. Rogers, and Yonggang Huang. Buckling in serpentine microstructures and applications in elastomer-supported ultra-stretchable electronics with high areal coverage. *Soft Matter*, 9(33):8062, 2013.

[39] Taisong Pan, Matt Pharr, Yinji Ma, Rui Ning, Zheng Yan, Renxiao Xu, Xue Feng, Yonggang Huang, and John A. Rogers. Experimental and Theoretical Studies of Serpentine Interconnects on Ultrathin Elastomers for Stretchable Electronics. *Advanced Functional Materials*, 2017.

[40] Nanshu Lu, Xi Wang, Zhigang Suo, and Joost Vlassak. Metal films on polymer substrates stretched beyond 50%. *Applied Physics Letters*, 91(22):221909, nov 2007.

[41] Jongseung Yoon, Alfred J. Baca, Sang Il Park, Paulius Elvikis, Joseph B. Geddes, Lanfang Li, Rak Hwan Kim, Jianliang Xiao, Shuodao Wang, Tae Ho Kim, Michael J. Motala, Bok Yeop Ahn, Eric B. Duoss, Jennifer A. Lewis, Ralph G. Nuzzo, Placid M. Ferreira, Yonggang Huang, Angus Rockett, and John A. Rogers. Ultrathin silicon solar microcells for semitransparent, mechanically flexible and microconcentrator module designs. *Nature Materials*, 2008.

[42] Sheng Xu, Yihui Zhang, Jiung Cho, Juhwan Lee, Xian Huang, Lin Jia, Jonathan A. Fan, Yewang Su, Jessica Su, Huigang Zhang, Huanyu Cheng, Bingwei Lu, Cunjiang Yu, Chi Chuang, Tae-il Kim, Taeseup Song, Kazuyo Shigeta, Sen Kang, Canan Dagdeviren, Ivan Petrov, Paul V. Braun, Yonggang Huang, Ungyu Paik, and John A. Rogers. Stretchable batteries with self-similar serpentine interconnects and integrated wireless recharging systems. *Nature Communications*, 4:1543, feb 2013.

[43] Cunjiang Yu, Charan Masarapu, Jiepeng Rong, Bing Q.Mg Wei, and Hanqing Jiang. Stretchable supercapacitors based on buckled single-walled carbon nanotube macrofilms. *Advanced Materials*, 21(47):4793–4797, 2009.

[44] Yi Min Xie, Xiaoying Yang, Jianhu Shen, Xiaolei Yan, Arash Ghaedizadeh, Jianhua Rong, Xiaodong Huang, and Shiwei Zhou. Designing orthotropic materials for negative or zero compressibility. *International Journal of Solids and Structures*, 51(23):4038–4051, 2014.

[45] Jongho Lee, Jian Wu, Mingxing Shi, Jongseung Yoon, Sang Il Park, Ming Li, Zhuangjian Liu, Yonggang Huang, and John A. Rogers. Stretchable GaAs

photovoltaics with designs that enable high areal coverage. *Advanced Materials*, 23(8):986–991, 2011.

[46] Nathan Lazarus, Christopher D. Meyer, and Sarah S. Bedair. Fractal inductors. *IEEE Transactions on Magnetics*, 50(4), 2014.

[47] Nathan Lazarus, Chris D. Meyer, Sarah S. Bedair, Geoffrey A. Slipher, and Iain M. Kierzewski. Magnetic elastomers for stretchable inductors. *ACS Applied Materials and Interfaces*, 7(19):10080–10084, 2015.

[48] Nathan Lazarus, Chris D Meyer, and Sarah S Bedair. Stretchable Inductor Design. *IEEE Transactions on Electron Devices*, 62(7):1–1, 2015.

[49] N. Lazarus and S. S. Bedair. Improved power transfer to wearable systems through stretchable magnetic composites. *Applied Physics A: Materials Science and Processing*, 122(5):1–7, 2016.

[50] Nanshu Lu and Shixuan Yang. Mechanics for stretchable sensors. *Current Opinion in Solid State and Materials Science*, 2015.

[51] Domenica Visalli, Jury Gustaaf Borghs, Promoter André Stesmans, Promoter André Vantomme, and Chair Robert Pierre Mertens Cor Claeys Gaudenzio Meneghesso Marleen Van Hove Joff Derluyn. OPTIMIZATION OF GaN-on-Si HEMTs FOR HIGH VOLTAGE APPLICATIONS. 2011.

[52] T Hanada. Basic Properties of ZnO, GaN, and Related Materials. *Oxide and Nitride Semiconductors*, pages 1–19, 2009.

[53] Matthew A Hopcroft, William D Nix, and Thomas W Kenny. What is the Young's Modulus of Silicon? *JOURNAL OF MICROELECTROMECHANICAL SYSTEMS*, 19(2), 2010.

[54] J.J. Wortman and R.A Evans. Young's Modulus, Shear Modulus, and Poisson's Ratio in Silicon and Germanium. *Journal of Applied Physics*, 36, Number(153-156), 1964.

[55] Kevin M. Knowles and Philip R. Howie. The Directional Dependence of Elastic Stiffness and Compliance Shear Coefficients and Shear Moduli in Cubic Materials. *Journal of Elasticity*, 2015.

[56] A. Polian, M. Grimsditch, and I. Grzegory. Elastic constants of gallium nitride. *Journal of Applied Physics*, 1996.

[57] A. Krost, A. Dadgar, G. Strassburger, and R. Clos. GaN-based epitaxy on silicon: Stress measurements. *Physica Status Solidi (A) Applied Research*, 2003.

[58] Bavani Balakrisnan, Aleksandar Nacev, Jeffrey M. Burke, Abhijit Dasgupta, and Elisabeth Smela. Design of compliant meanders for applications in MEMS, actuators, and flexible electronics. *Smart Materials and Structures*, 21(7), 2012.

[59] Yihui Zhang, Haoran Fu, Yewang Su, Sheng Xu, Huanyu Cheng, Jonathan A. Fan, Keh-Chih Hwang, John A. Rogers, and Yonggang Huang. Mechanics of ultra-stretchable self-similar serpentine interconnects. *Acta Materialia*, 61(20):7816–7827, 2013.

[60] Kevin Huang and Peter Peumans. PROCEEDINGS OF SPIE Stretchable silicon sensor networks for structural health monitoring "Stretchable silicon sensor networks for structural health monitoring," Proc. SPIE 6174, Smart Structures and Materials 2006: Sensors and Smart Structures Technologie. 2006.

[61] Jaemin Kim, Mincheol Lee, Hyung Joon Shim, Roozbeh Ghaffari, Hye Rim Cho, Donghee Son, Yei Hwan Jung, Min Soh, Changsoon Choi, Sungmook Jung, Kon Chu, Daejong Jeon, Soon Tae Lee, Ji Hoon Kim, Seung Hong Choi, Taeghwan Hyeon, and Dae Hyeong Kim. Stretchable silicon nanoribbon electronics for skin prosthesis. *Nature Communications*, 2014.

[62] Tzu Hsuan Chang, Kanglin Xiong, Sung Hyun Park, Hongyi Mi, Huilong Zhang, Solomon Mikael, Yei Hwan Jung, Jung Han, and Zhenqiang Ma. High power fast flexible electronics: Transparent RF AlGaN/GaN HEMTs on plastic substrates. In *2015 IEEE MTT-S International Microwave Symposium, IMS 2015*, 2015.

[63] N. Defrance, F. Lecourt, Y. Douvry, M. Lesecq, V. Hoel, A. Des Lecavelier Etangs-Levallois, Yvon Cordier, A. Ebongue, and J. C. De Jaeger. Fabrication, characterization, and physical analysis of AlGaN/GaN HEMTS on flexible substrates. *IEEE Transactions on Electron Devices*, 60(3):1054–1059, 2013.

[64] Z. Ma, Y.H Jung, J.H. Seo, J. Lee, S.J. Cho, T.H Chang, H. Zhang, S. Gong, and W. Zhou. Radio-frequency flexible and stretchable electronics. *Semiconductor Technology Internation Conference (CSTIC) 2016 China IEEE*, 2016.

[65] Keon Jae Lee, Matthew A. Meitl, Jong-Hyun Ahn, John A. Rogers, Ralph G. Nuzzo, Vipan Kumar, and Ilesanmi Adesida. Bendable GaN high electron mobility transistors on plastic substrates. *Journal of Applied Physics*, 2006.

[66] Keon Jae Lee, Jaeseob Lee, Heedon Hwang, Zachary J. Reitmeier, Robert F. Davis, John A. Rogers, and Ralph G. Nuzzo. A printable form of single-crystalline gallium nitride for flexible optoelectronic systems. *Small*, 2005.

[67] Bok Y Ahn, Eric B Duoss, Michael J Motala, Xiaoying Guo, Sang-il Park, Jongseung Yoon, Ralph G Nuzzo, John A Rogers, Jennifer A Lewis, and

Bok Y Ann. Omnidirectional Printing and of Flexible , Stretchable , Silver Microelectrodes Spanning. *Science Mag*, 323(5921):1590–1593, 2009.

[68] Yugang Sun, Won Mook Choi, Hanqing Jiang, Yonggang Y. Huang, and John A. Rogers. Controlled buckling of semiconductor nanoribbons for stretchable electronics. *Nature Nanotechnology*, 1(3):201–207, 2006.

[69] Banqiu Wu, Ajay Kumar, and Sharma Pamarthy. High aspect ratio silicon etch: A review. *Journal of Applied Physics*, 108(5), 2010.

[70] Jianan Lv, Zhenchuan Yang, Guizhen Yan, Wenkui Lin, Yong Cai, Baoshun Zhang, and Kevin J Chen. Fabrication of Large-Area Suspended MEMS Structures Using GaN-on-Si Platform. *IEEE ELECTRON DEVICE LETTERS*, 30(10), 2009.

[71] Z. Yang, R. N. Wang, S. Jia, D. Wang, B. S. Zhang, K. M. Lau, and K. J. Chen. Mechanical characterization of suspended GaN microstructures fabricated by GaN-on-patterned-silicon technique. *Applied Physics Letters*, 88(4):1–3, 2006.

[72] S. Davies, T. S. Huang, M. H. Gass, A. J. Papworth, T. B. Joyce, and P. R. Chalker. Fabrication of GaN cantilevers on silicon substrates for microelectromechanical devices. *Applied Physics Letters*, 84(14):2566–2568, 2004.

[73] Riccardo D'Agostino and Daniel L. Flamm. Plasma etching of Si and SiO$_2$ in SF$_6$ O$_2$ mixtures. *Journal of Applied Physics*, 52(1):162–167, 1981.

[74] I DeWolf. Micro-Raman spectroscopy to study local mechanical stress in silicon integrated circuits. *Semiconductor Science and Technology*, 11(2):139–154, 1996.

[75] A Atkinson and S C Jain. Spatially Resolved Stress Analysis Using Raman Spectroscopy. *Journal of Raman Spectroscopy*, 30(10):885–891, 1999.

[76] E Ochoa L A Starman J Lott, M Amer W Cowan. Residual Stress Characterisation in MEMS Microbridges using Micro Raman Spectroscopy. *Modelling of Microsystems*, pages 2–5, 2002.

[77] L. Starman and R. Coutu. Stress Monitoring of Post-processed MEMS Silicon Microbridge Structures Using Raman Spectroscopy. *Experimental Mechanics*, 52(9):1341–1353, 2012.

[78] V. T. Srikar, Anna K. Swan, M. Selim Ünlü, Bennett B. Goldberg, and S. Mark Spearing. Micro-Raman measurements of bending stresses in micromachined silicon flexures. *Journal of Microelectromechanical Systems*, 12(6):779–787, 2003.

[79] Lavern a Starman. Characterization of Residual Stress in Microelectromechanical Systems (MEMS) Devices using Raman Spectroscopy. *Air Force Institute of Technology*, 2002.

[80] Th. Englert, G. Abstreiter, and J. Pontcharra. Determination of existing stress in silicon films on sapphire substrate using Raman spectroscopy. *Solid-State Electronics*, 23(1):31–33, 1980.

[81] S Ganesan, A.A Maradudn, and J. Oitmaa. A Lattice Theory of Morphic Effects in the Crystas of the Diamond Structure. *Annals of Physics*, 594(68):556–594, 1970.

[82] V T Srikar and S Mark Spearing. A Critical Review of Microscale Mechanical Testing Methods Used in the Design of Microelectromechanical Systems. *Experimental Mechanics*, 43(3):238–247, 2003.

[83] D Naumenko, V Snitka, M Duch, N Torras, and J Esteve. Microelectronic Engineering Stress mapping on the porous silicon microcapsules by Raman microscopy. *Microelectronic Engineering*, 98:488–491, 2012.

[84] Theory of raman scattering *http://bwtek.com/raman-theory-of-raman-scattering/, journal*, 2017.

[85] E. Anastassakis, A. Pinczuk, Burstein E., F.H Pollak, and M. Cardona. Effect of static uniaxial stress on the raman spectrum of silicon. *Solid State Communications*, 8.2:133–138, 1970.

[86] K Brunner and Abstreiter. STRAIN AT Si-SIO INTERFACES STUDIED BY MICRO-RAMAN SPECTROSCOPY. *Applied Surface Science*, 39:116–126, 1989.

[87] E. Anastassakis, A. Cantarero, and M. Cardona. Piezo-Raman measurements and anharmonic parameters in silicon and diamond. *Physical Review B*, 41(11), 1990.

[88] Tsutomu Iida, Takamasa Itoh, Daisuke Noguchi, Yoshifumi Takanashi, Yukio Takano, and Yozo Kanda. Residual lattice strain in thin silicon-on-insulator bonded wafers: Effects on electrical properties and raman shifts. *Journal of Applied Physics*, 89(4):2109–2114, 2001.

[89] F. Shahedipour-Sandvik, J. Leathersich, R. P. Tompkins, P. Suvarna, M. Tungare, T. A. Walsh, K. W. Kirchner, S. Zhou, and K. A. Jones. Enhanced performance of an AlGaN/GaN high electron mobility transistor on Si by means of improved adatom diffusion length during MOCVD epitaxy. *Semiconductor Science and Technology*, 28(7), 2013.

[90] M. Kuball. Raman spectroscopy of GaN, AlGaN and AlN for process and growth monitoring/control. *Surface and Interface Analysis*, 2001.

[91] Ho Won Jang, Chang Min Jeon, Ki Hong Kim, Jong Kyu Kim, Sung-Bum Bae, Jung-Hee Lee, Jae Wu Choi, and Jong-Lam Lee. Mechanism of two-dimensional electron gas formation in Al x Ga 1Àx NÕGaN heterostructures. 2002.

[92] O. Ambacher, B. Foutz, J. Smart, J. R. Shealy, N. G. Weimann, K. Chu, M. Murphy, A. J. Sierakowski, W. J. Schaff, L. F. Eastman, R. Dimitrov, A. Mitchell, and M. Stutzmann. Two dimensional electron gases induced by spontaneous and piezoelectric polarization in undoped and doped AlGaN/GaN heterostructures. *Journal of Applied Physics*, 2000.

[93] S. Tripathy, S. J. Chua, P. Chen, and Z. L. Miao. Micro-Raman investigation of strain in GaN and AlxGa1-xN/GaN heterostructures grown on Si(111). *Journal of Applied Physics*, 92(7):3503–3510, 2002.

[94] P. Sangeetha, K. Jeganathan, and V. Ramakrishnan. Micro-Raman investigations of InN-GaN core-shell nanowires on Si (111) substrate. *AIP Advances*, 3(6), 2013.

[95] M.S Mohajerani, S. Khachadorian, T. Schimpke, C. Nensteil, J. Hartmann, J. Ledig, A. Avramescu, M. Strassburg, A. Hoffman, and A. Waag. Evaluation of local free carrier concentrations in individual heavily-doped GaN: Si micro-rods by micro-Raman spectroscopy. *Journal of Applied Physics Letters*, 108(091112-1), 2016.

[96] Hiroshi Harima. Properties of GaN and related compounds studied by means of Raman scattering. *J. Phys.: Condens. Matter*, 14:967–993, 2002.

[97] H. Harima, H. Sakashita, and S. Nakashima. Raman Microprobe Measurement of Under-Damped LO-Phonon-Plasmon Coupled Mode in n-Type GaN. *Materials Science Forums*, 264-268:1363–1366, 1998.

[98] T. Kozawa, T. Kachi, H. Kano, Y. Taga, M. Hashimoto, N. Koide, and K. Manabe. Raman scattering from LO phonon-plasmon coupled modes in gallium nitride. *Journal of Applied Physics*, 75(2):1098–1101, 1994.

[99] C. Wetzel, W. Walukiewicz, E. Haller, J. Ager, I. Grzegory, S. Porowski, and T. Suski. Carrier localization of as-grown n-type gallium nitride under large hydrostatic pressure. *Physical Review B - Condensed Matter and Materials Physics*, 53(3):1322–1326, 1996.

[100] A Sarua, M Kuball, and J E Van Nostrand. Phonon deformation potentials of the phonon mode of Internal quantum efficiency and nonradiative recombination coefficient of GaInN/GaN multiple quantum wells with different dislocation densities Phonon deformation potentials of the E 2 " high... phonon mod. *Citation: Appl. Phys. Lett.SiC Journal of Applied Physics Journal of Applied Physics Applied Physics Letters Journal of Applied Physics Applied Physics Letters*, 85(94):2217–1426, 2004.

[101] Vibhu Jindal, James R. Grandusky, Neeraj Tripathi, Fatemeh Shahedipour-Sandvik, Steven LeBoeuf, Joleyn Balch, and Todd Tolliver. Selective area heteroepitaxy of nano-AlGaN ultraviolet excitation sources for biofluorescence application. *Journal of Materials Research*, 22(4):838–844, 2007.

[102] I. Mahaboob, K. Hogan, S. Novak, F. Shahedipour-Sandvik, R. Tompkins, and N. Lazarus. Influence of mask material on the electrical properties of selective area epitaxy gan microstructures. *Journal of Vacuum Science and Technology B, Nanotechnology and Microelectronnics: Materials, Processing, Measurement, and Phenomena*, 36, 2018.

[103] Vibhu Jindal, James Grandusky, Muhammad Jamil, Neeraj Tripathi, Bradley Thiel, Fatemeh Shahedipour-Sandvik, Joleyn Balch, and Steven LeBoeuf. Effect of interfacial strain on the formation of AlGaN nanostructures by selective area heteroepitaxy. *Physica E: Low-Dimensional Systems and Nanostructures*, 40(3):478–483, 2008.

[104] V. Jindal, N. Tripathi, M. Tungare, O. Paschos, P. Haldar, and F. Shahedipour-Sandvik. Selective area heteroepitaxy of low dimensional a-plane and c-plane InGaN nanostructures using pulsed MOCVD. *Physica Status Solidi (C) Current Topics in Solid State Physics*, 5(6):1709–1711, 2008.

[105] F Cerdeira, C. J. Buchenauer, F. H. Pollak, and M. Cardona. Stress-induced raman shifts of diamond and zincblende semiconductors, 1972.

[106] D S Knight and W B White. Characterization of Diamond Films By Raman-Spectroscopy. *Journal of Materials Research*, 4(November 1988):385–393, 1989.

[107] I. H. Campbell and P. M. Fauchet. The effects of microcrystal size and shape on the one phonon Raman spectra of crystalline semiconductors. *Solid State Communications*, 58(10):739–741, 1986.

[108] Ibrahim A. Alhomoudi and G. Newaz. Residual stresses and Raman shift relation in anatase TiO2thin film. *Thin Solid Films*, 517(15):4372–4378, 2009.

[109] Elizabeth M. Tennyson, Joseph L. Garrett, Jesse A. Frantz, Jason D. Myers, Robel Y. Bekele, Jasbinder S. Sanghera, Jeremy N. Munday, and Marina S. Leite. Nanoimaging of Open-Circuit Voltage in Photovoltaic Devices. *Advanced Energy Materials*, 5(23):1501142, dec 2015.